FEASIBILITY AND APPLICATION OF A Cu_xO-BASED MEMRISTOR FOR SENSING OXYGEN AND OTHER GASES

By

Chinwe Pamela Nyenke

A DISSERTATION

Submitted to
Michigan State University
in partial fulfillment of the requirements
for the degree of

Electrical Engineering - Doctor of Philosophy

2017

ABSTRACT

FEASIBILITY AND APPLICATION OF A Cu_xO-BASED MEMRISTOR FOR SENSING OXYGEN AND OTHER GASES

By

Chinwe Pamela Nyenke

This dissertation introduces the design, fabrication, and application of a copper-oxide-based memristor for the passive sensing of oxygen and other gases. The device design was as follows: Deposition of copper (Cu) bottom electrodes, (oxygen) vacancy-rich copper oxide (Cu_xO) switching layers, and tungsten (W) top electrodes in a crossbar array structure. The Cu_xO layer was deposited via reactive sputtering of a Cu target with an argon-oxygen (Ar/O_2) mixture. A portion of this layer was extended from each array cell to be exposed for sensing. Memristive devices of different switching layer thicknesses were initially explored for irreversible sensing of oxygen in ambient air. Results of this first experiment demonstrated an increase in resistance states upon prolonged exposure to ambient air. For the second experiment, memristive devices were fabricated with sub-micron holes that were etched into the W top electrode to better reveal the switching layer surface. The devices were also subjected to ambient oxygen at 180 deg C to induce passive sensing in minutes. Resistance results were consistent with the first experiment but also revealed a dependence on the surface area of the exposed oxide. Finally, memristive devices were investigated in a third experiment for reversible sensing of an oxidizing gas and reducing gas at room

temperature. This time, changes were not only observed in resistance but also in hysteresis (current versus voltage) depending on the type of gas introduced. Overall, this work demonstrates a step towards the use of the memristor as a gas sensor, which we have named “memsensors”, by taking advantage of the device’s ability to memorize (or record) historical information.

Dedicated to my parents, sisters, husband, and son.

ACKNOWLEDGMENTS

Firstly, I would like to thank my advisor – Dr. Lixin Dong – for his guidance and support throughout these years. Without his intellectual probing and ideas, this work would not be what it is. He challenged me to go down the path of considering a new application for memristors that had never before been explored.

Additionally, I would like to thank Dr. Percy Pierre for his longtime mentorship, encouragement, and motivation. His belief in me helped to instill the perseverance I needed to complete this research and dissertation. I would also like to acknowledge his support of my work, including through the Alfred P. Sloan Foundation M.PhD Program and GAANN Fellowship Program.

I would also like to thank my dissertation committee – Dr. Ning Xi, Dr. Tim Hogan, Dr. Wen Li, and Dr. Junghoon Yeom – for their assistance and motivation in completing this project. They helped me to ponder and explore possibilities I had not initially realized.

I would like to acknowledge Dr. Baokang Bi and Dr. Per Askeland for information and equipment training related to fabrication of the devices for this project. Additionally, I would like to acknowledge Dr. Zheng Fan and Amberley Huang for critical assistance in data collection.

TABLE OF CONTENTS

LIST OF TABLES

LIST OF FIGURES

CHAPTER 1 INTRODUCTION

1.1 MEMRISTOR – WHAT IS IT?

More than forty-five years ago, there were only three fundamental two-terminal circuit elements known to relate charge or current ($dq = idt$) to flux or voltage ($d\varphi = vdt$). These elements were the resistor ($dv = Rdi$), capacitor ($dq=Cdv$), and inductor ($d\varphi=Ldi$). In 1971, professor Leon Chua mathematically recognized a fourth fundamental circuit element to relate charge q and flux φ via the equation $d\varphi=Mdq$ [1]. He named this element the memory resistor, or memristor.

It was not until 2008 that a feasible physical model of the memristor was presented by Strukov and others [2] in *Nature*. The researchers described a semiconductor device divided into two regions – one with a high concentration of

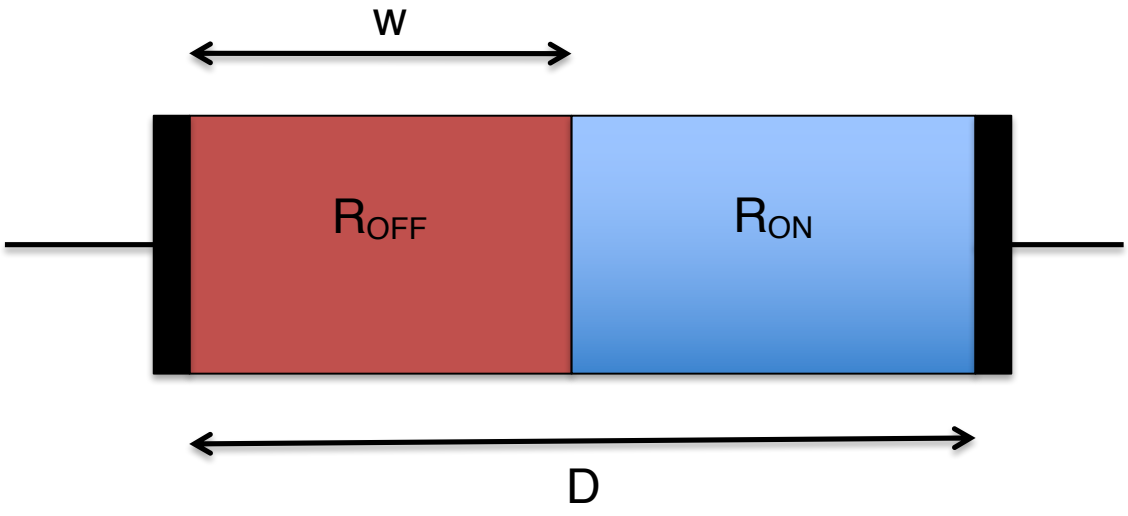

Figure 1. Semiconductor film with a high dopant region (R_{OFF}) and low dopant region (R_{ON}).

dopants and the other with a low concentration of dopants. By consequence, the region with high dopant concentration has high electrical conductivity translating to low resistance R_{ON}. Alternatively, the region with low dopant concentration has low electrical conductivity and thus, large resistance R_{OFF}. An illustration of this device is provided in Figure 1.

When an external bias is applied across the device, the charged dopants will then drift, thus moving the boundary between the two regions. Assuming Ohmic conduction and linear ionic drift in a uniform field [2], we then obtain the following:

$$v(t) = \left(R_{ON} \frac{w(t)}{D} + R_{OFF} \left(1 - \frac{w(t)}{D} \right) \right) i(t) \tag{1}$$

$$\frac{dw(t)}{dt} = \mu_v \frac{R_{ON}}{D} i(t) \tag{2}$$

where μ_v is the electrical mobility, *w(t)* is the width of the high dopant region over time *t*, *D* is the thickness of the semiconductor film, and *i(t)* is the current. If we integrate equation (2) to solve for *w(t)*, we get:

$$w(t) = \mu_v \frac{R_{ON}}{D} q(t) \tag{3}$$

Substituting equation (3) into equation (1) then gives us the voltage in terms of charge *q(t)* and *i(t)*:

$$v(t) = \left(\mu_v \frac{{R_{ON}}^2}{D^2} q(t) + R_{OFF} \left(1 - \frac{\mu_v R_{ON}}{D^2} q(t) \right) \right) i(t) \quad (4)$$

Thus, the term on the right side of equation (4) in front of the term *i(t)* is just the memristance of the device, which is resistance that is dependent on the drift of charged dopants. For the case where $R_{ON} << R_{OFF}$, the memristance simplifies to the following:

$$M(q) = R_{OFF} \left(1 - \frac{\mu_v R_{ON}}{D^2} q(t) \right) \quad (5)$$

1.2 BACKGROUND AND MOTIVATION

In metal-oxide based memristors, it is believed that resistive switching depends on the migration of oxygen vacancies [3-6] or oxygen ions [7,8] between electrodes. Based on the external bias applied, these devices can switch between low and high resistance states that are hundreds to thousands of ohms and tens to thousands of kilo-ohms, respectively. The understanding of this phenomenon combined with the increasing limits of complementary metal–oxide semiconductors [3,5,9] have led to a surge in memristor research for memory applications, particularly for non-volatile memory (NVM) devices, or resistive random-access memories (RRAMs) [9,10]. Considerable attention has also been given to the memristor for logic applications, including as synapses in neuromorphic systems [10–12]. Over the past several years, improvements in

memristive switching behavior have also been reported, including increased speeds [5,13] and endurances [10] for particular metal oxide combinations and stoichiometric ratios [5,14].

Excluding memristor research, metal oxides have been heavily studied for gas and chemical sensing [15–19] because of inherent defective sites, which allow for the adsorption of oxygen and other chemical species. For example, in 2014, V. Hien and others developed Cu_2O nanorods and nano-trees to irreversibly sense hydrogen sulfide (H_2S) [18]. The sensing mechanism of their samples involved a phase transformation of Cu_2O to copper sulfide (CuS). In 2013, M. Ahmad and other researchers fabricated tungsten oxide (WO_3) thin films for ethanol (C_2H_6O) sensing. They concluded that the reaction between the sensor's WO_3 surface and the ethanol molecules was attributed to the oxygen ion species adsorbed by the metal oxide while in air [19].

This ability of metal oxides to adsorb oxygen ions begs the question of how can we exploit metal-oxide based memristance for gas or chemical sensing.

(This section is reproduced from publication [20].)

1.3 STATEMENT OF THE PROBLEM

In this study, metal-oxide based memristors are fabricated and investigated for feasibility and application in passive sensing of oxygen and other gases. The

traditional memristor is influenced by voltage only and typically researched for electronic applications in memory and logic. This study, however, examines the influence of gas and voltage on the memristor, thus applying the device with the added function of gas sensing.

A nano-sized metal-oxide memristor is fabricated with a portion of the switching layer exposed. Sensing is determined as it relates to adsorption of oxygen and other gases to the exposed metal oxide.

1.4 PURPOSE OF THE STUDY

The purpose of this project is to expand memristor research, especially that of metal oxides, into the area of gas sensing. Another purpose of this project is to increase the understanding of environmental effects, such as tuning, on memristors. Finally, there is the potential application of such passive sensors as sensing alternatives for devices which typically have no batteries integrated due to their small sizes including micro/nanorobots, such as catalytically-driven microjets [21] or artificial bacteria flagella [22] designed for medical applications.

1.5 RESEARCH QUESTIONS

In particular, the following questions will be addressed:

- Can the memristance of a metal-oxide based memristor be exploited for sensing oxygen and other gases?
- If so, what is the nature of sensing in this memristor?
    - What is happening at the physical level?
    - How do the surface layer physics (and bulk layer physics) come into play?
- How will heat affect sensing?
- How will design of the device affect sensing?
- Finally, how do the memristive effects from exposure to oxygen compare to those from exposure to other gases.

1.6 DISSERTATION OUTLINE

The rest of this dissertation is outlined as follows:

Chapter 2 will give a review of relevant literature on memristor research, including the design of metal-oxide based devices, applications of the memristor in electronics, and advances in sensing. Chapter 3 will discuss the fabrication of the memristor as well as choices in approach and design. Chapter 4 will cover the first study – passive sensing of ambient oxygen at room temperature with a prototype device. Chapter 5 will cover an improved “memsensor” design and

passive sensing of oxygen with heat. Chapter 6 will discuss the reversible detection of an oxidizing gas and a reducing gas with the improved “memsensor”. Chapter 7 will sumamrize the dissertation with conclusions and future work concerning each study.

REFERENCES

REFERENCES

1. L. O. Chua, “Memristor - the missing circuit element,” *IEEE Transactions Circuit Theory*, vol. 18, pp. 507–519, 1971.

2. D. Strukov, G. Snider, D. Stewart, and R. Williams, "The missing memristor found," *Nature*, vol. 453, pp. 80-83, May 2008.

3. R. Waser and M. Aono, “Nanoionics-based resistive switching memories,” *Nature Materials*, vol. 6, pp. 833–840, Nov. 2007.

4. Y. Yang, S. Choi, and W. Lu, “Oxide heterostructure resistive memory,” *Nano Letters*, vol. 13, pp. 2908-2915, May 2013.

5. J. J. Yang, M. D. Pickett, X. Li, D. A. A. Ohlberg, D. R. Stewart, and R. S. Williams. “Memristive switching mechanism for metal/oxide/metal nanodevices,” *Nature Nanotechnology*, vol. 3, pp. 429-433, Jun. 2008.

6. J.P. Strachan, et al. “Direct identification of the conducting channels in a functioning memristive device,” *Advanced Materials*, vol. 22, pp. 3573–3577, 2010.

7. T.-M. Tsai, K.-C. Chang, T.-C. Chang, R. Zhang, T. Wang, C.-H. Pan, and K.-H. Chen, “Resistive switching mechanism of oxygen-rich indium tin oxide resistance random access memory,” *IEEE Electron Device Letters*, vol. 37, no. 4, pp. 408-411, Apr. 2016.

8. Y.-J. Huang, S.-C. Chao, D.-H. Lien, C.-Y. Wen, J.-H. He, and S.-C. Lee, “Dual-functional memory and threshold resistive switching based on the push-pull mechanism of oxygen ions,” *Scientific Reports |*, vol. 6, art. no. 23945, Apr. 2016.

9. D. Sacchetto, G. De Micheli, and Y. Leblebici, "Multiterminal memristive nanowire devices for logic and memory applications: a review," *Proceedings of the IEEE*, vol. 100, pp. 2008-2020, Jun. 2012.

10. D. Jeong, R. Thomas, R. Katiyar, J. Scott, H. Kohlstedt, A. Petraru, and C. Hwang, “Emerging memories: Resistive switching mechanisms and current status,” *Reports on Progress in Physics*, vol. 75, art. no. 076502, Jul. 2012.

11. S. Jo, T. Chang, I. Ebong, B. Bhadviya, P. Mazumder, and W. Lu, "Nanoscale memristor device as synapse in neuromorphic systems," *Nano Letters*, vol. 10, pp. 1297-1301, Apr. 2010.

12. T. Chang, Y. Yang, and W. Lu, "Building neuromorphic circuits with memristive devices," *IEEE Circuits and Systems Magazine*, vol. 13, pp. 56-73, 2013.

13. J. Tedesco, L. Stephey, M. Hernandez-Mora, C. Richter, and N. Gergel-Hackett, "Switching mechanisms in flexible solution-processed TiO_2 memristors," *Nanotechnology*, vol. 23, art. no. 305206, Aug. 2012.

14. P. R. F. Rocha, A. Kiazadeh, D. M. De Leeuw, S. C. J. Meskers, F. Verbakel, D. M. Taylor, and H. L. Gomes. “The role of internal structure in the anomalous switching dynamics,” *Journal of Applied Physics*, vol. 113, no. 13, art. no. 134504, Jul. 2013.

15. G. F. Fine, L. M. Cavanagh, A. Afonja, and R. Binions, “Metal oxide semiconductor gas sensors in environmental monitoring,” *Sensors*, vol. 10, pp. 5469-5502, Jun. 2010.

16. R. Ionescu, A. Hoel, C.G. Granqvist, E. Llobet, P. Heszler, “Low-level detection of ethanol and H2S with temperature-modulated WO_3 nanoparticle gas sensors,” *Sensors and Actuators B*, vol. 104, pp. 132-139, 2005.

17. Z. Wen, L. Tian-mo, and L. De-jun, “Formaldehyde gas sensing property and mechanism of TiO_2–Ag nanocomposite,” *Physica B: Condensed Matter*, vol. 405, pp. 4235-4239, Oct. 2010.

18. V. Hien, J.-L.You, K.-M. Jo, S.-Y. Kim, J.-H. Lee, et al., "H_2S-sensing properties of Cu_2O submicron-sized rods and trees synthesized by radio frequency magnetron sputtering," *Sensors and Actuators B*, vol. 202, pp. 330-338, Oct. 2014.

19. M. Ahmad, A. Sadek, J. Ou, M.H. Yaacob, et al., “Facile synthesis of nanostructured WO_3 thin films and their characterization for ethanol sensing," *Materials Chemistry and Physics*, vol. 141, pp. 912-919, Jun. 2013.

20. C. Nyenke and L. Dong, “Sensing ambient oxygen using a W/CuxO/Cu memristor,” *IEEE 10th International Conference on Nano/Micro Engineered and Molecular Systems*, pp. 254-258, Apr. 2015. © 2015 IEEE.

21. V. Magdanz, M. Guix, and O. G. Schmidt, “Tubular micromotors: from microjets to spermbots,” *Robotics and Biomimetics*, vol. 1, no. 11, pp. 1-10, Oct. 2014.

22. L. Zhang, J. J. Abbott, L. Dong, B. E. Kratochvil, D. Bell, and B. J. Nelson, “Artificial bacterial flagella: Fabrication and magnetic control,” *Applied Physics Letters*, vol. 94, art. no. 064107, Feb. 2009.

CHAPTER 2 LITERATURE REVIEW

2.1 METAL-OXIDE MEMRISTOR: SWITCHING LAYER DESIGN

While the simplest design of a metal-oxide based memristor consists of a transition metal oxide sandwiched between two metal electrodes, consideration for improved endurance and performance have propelled design of the device into the use of nonstoichiometric switching layers [1]-[3]. This is because the chemistry of such layers allows for increased oxygen vacancies [4]-[6] – or increased oxygen ions [7,8] – giving rise to more efficiently formed conductive filaments. To date, some of the more studied nonstoichiometric switching layers include copper-rich oxide (Cu_xO) [9]-[13], oxygen-deficient titanium oxide (TiO_{2-x}) [14]-[16], oxygen-deficient silicon oxide (SiO_x) [6,17-20], oxygen-rich tungsten oxide (WO_x) [21]-[24], and oxygen-rich zinc oxide (ZnO_x) [25]-[27].

Another area of memristor design improvement has been the sandwiching of the metal oxide between an inactive metal electrode and an active metal electrode. With this particular arrangement, the active electrode can contribute metal ions to the formation of conductive filaments in the switching layer. Such electrodes have been constructed from metals like silver (Ag) [28]-[30] and copper (Cu) [31]-[33] that will react with the metal-oxide layer and emit metal ions. On the other hand, the inactive electrode is a metal, such as platinum (Pt) [28,33], gold (Au) [30], and tungsten (W) [30-31] that does not chemically react with the switching layer. For example, work by Yan and his colleagues [28] in a 2010

publication incorporated active electrodes fabricated from silver (Ag). The researchers were able to attribute resistive switching to Ag+ ions contributed from the electrode. Additionally, recent work by Zhang and his colleagues and others in 2016 suggested formation of titanium (Ti) conductive filaments from the incorporation of a TiN electrode in their device [34]. An illustration of this process is shown in Figure 2.

In recent years, bilayer structuring of the metal-oxide switching layer has been used to further enhance memristor performance and endurance. Work by Lin, Huang et al. [35] has demonstrated that the addition of ZnO_{1-x} nanorod arrays on a zinc oxide (ZnO) thin film reduces the operation voltage for a Pt/ZnO_{1-x} /ZnO/Pt memristor by acting as a reservoir for supplemental oxygen vacancies.

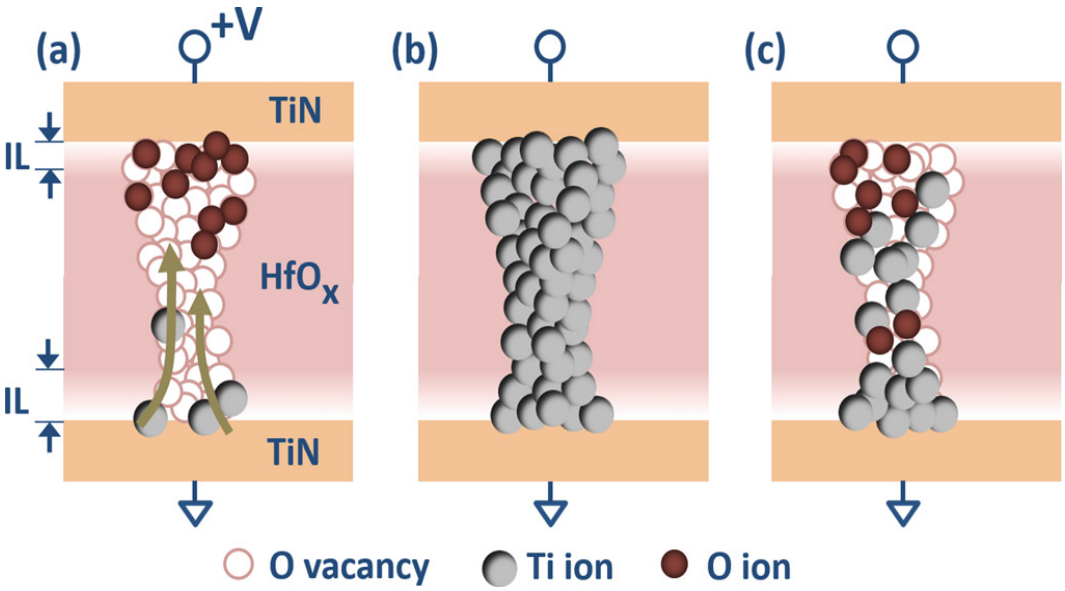

Figure 2. Formation of conductive filaments comprising of a) titanium ions only and b) oxygen vacancies and ions with titanium ions. Reprinted from H. Z. Zhang, D. S. Ang, K. S. Yew, and X. P. Wang, "Enhanced stability of complementary resistance switching in the TiN/HfO_x/TiN resistive random-access memory device via interface engineering," Applied Physics Letters, vol. 108, art. no. 083505, Feb 2016, with the permission of AIP Publishing.

This particular bilayer structure also exhibited hydrophobic behavior, which allowed for good switching endurance and the prevention of short circuits in a wet environment. Fabrication of the device involved deposition via sputtering (for the ZnO thin film) and a chemical solution process (for the ZnO_{1-x} nanorod array).

In a later work, Huang, Lin et al. further explored bilayer structures to improve the performance of traditional ZnO-based memory systems. This more

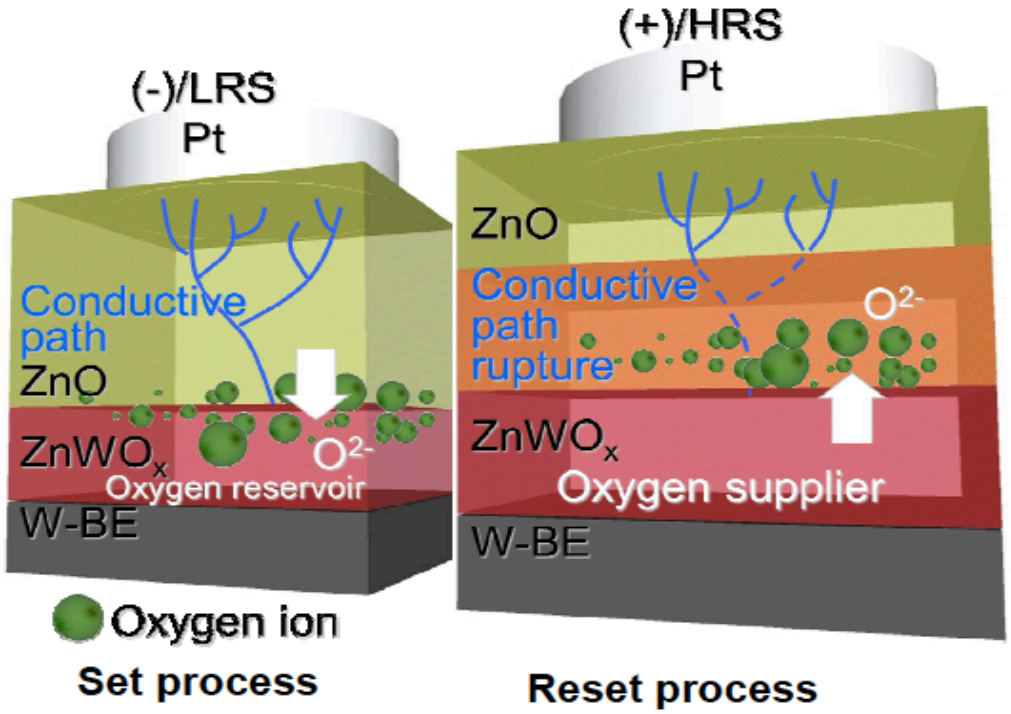

Figure 3. [LEFT] When a sufficient negative bias is applied, the ZnWOx layer acts as an oxygen ion reservoir to form the conductive filament. [RIGHT] When a sufficient positive is bias, the layer becomes an oxygen supplier leading to the rupture of the conductive filament. Reprinted with permission from S.-M. Lin, J.-S. Huang, W.-C. Chang, T.-C. Hou, H.-W. Huang, C.-H. Huang, S.- J. Lin and Y.-L. Chueh, "Single-step formation of ZnO/$ZnWO_x$ bilayer structure via interfacial engineering for high performance and low energy consumption resistive memory with controllable high resistance states," ACS Applied Materials & Interfaces, vol. 5, no. 16, pp. 7831-7837, Aug. 2013. Copyright 2013 American Chemical Society.

recent work [36] demonstrated that the inclusion of a thin $ZnWO_x$ layer between a zinc oxide (ZnO) film and bottom tungsten (W) electrode can improve switching endurance and enable less power consumption by reducing the compliance current. Other additional benefits of the ZnO/$ZnWO_x$ bilayer structure include enhancements in switching uniformity and increases in high resistance states. In this study, the ZnO/$ZnWO_x$ bilayer structure was spontaneously formed during a one-step sputtering process of ZnO onto the W contact. The switching process of the device is illustrated in Figure 3.

In addition to the aforementioned ZnO-based devices, other materials have been used to implement bilayer structures for memristors. For example, work by Lee et al. [37] has also demonstrated improvements in switching and power consumption but via a TaO-based structure. A TaO_{2-x} base layer was deposited via reactive sputtering followed by a TaO_2O_{5-x} layer that was formed using oxygen plasma to control thickness and provide medium resistivity. The overall design allowed for device stability and a reduction in the low-resistance-state current. Similarly, work by Pi and others [38] showed a reduction in total switching energy consumption via the addition of a thin yttrium (Y) layer onto a yttrium oxide (Y_2O_3) layer. Many other arrangements of bilayer structures have been demonstrated over the years [39, 40].

2.2 MEMRISTOR RESEARCH IN ELECTRONIC APPLICATIONS

Most memristor research has focused on applications in electronics, particularly in the areas of memory and logic [41, 42]. One intrigue is the memristor's potential to become an option for non-volatile memory [41] due to its ability to remember past information even after power has ceased. Additionally, since the resistance of these devices can switch between very small values (e.g., hundreds to thousands of ohms) and extremely large values (e.g., tens to thousands of kilo-ohms), such low and high states can represent 0s and 1s. Additionally, memristors are an appealing replacement for transistors due to density scaling [42] because while the transistor has two dimensions – gate width and length – the memristor has only one critical dimension – switching layer thickness [42, 43]. (Because the conductive filaments are few and localized rather than homogenous throughout the switching layer [44, 45], the area of the device is not a critical dimension.)

The more recent attention towards the memristor's application in logic has increased research in neuromorphic systems [46-50]. For example, Jo and others demonstrated the use of nanoscale silicon-based memristors, as shown in Figure 4, to model synapses supporting important neural functions, such as spike timing dependent plasticity [46]. In a more recent paper by Wang and his colleagues, the plasticity and learning behaviors of synapses are mimicked in HfO_x/ZnO_x-based memristors [47], as illustrated in Figure 5. The attraction to memristors in

neuromorphic research is largely due to “the local adaptive learning and large connectivity that can be obtained in such devices” [48].

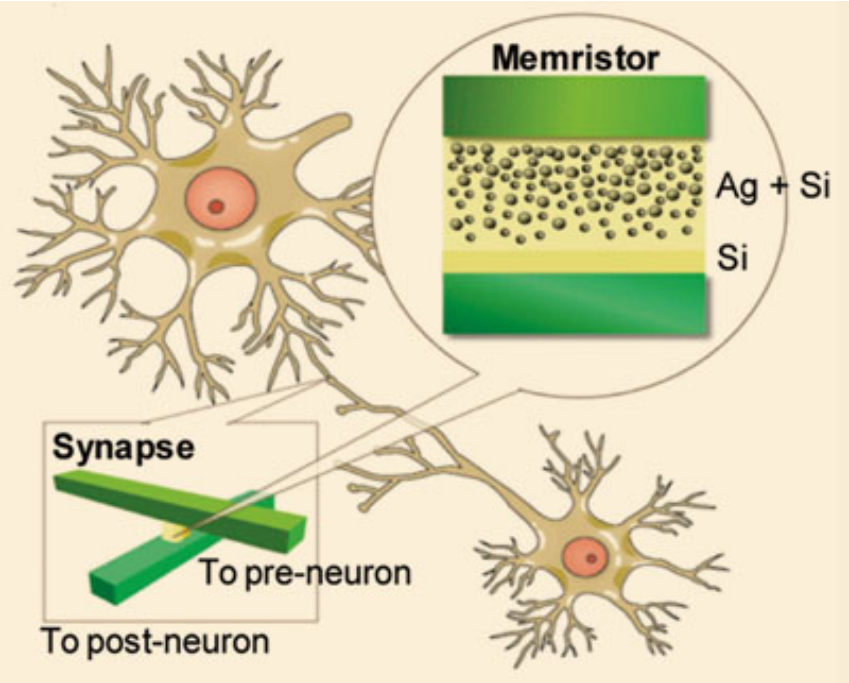

Figure 4. Reprinted with permission from S. Jo, T. Chang, I. Ebong, B. Bhadviya, P. Mazumder, and W. Lu, "Nanoscale Memristor Device as Synapse in Neuromorphic Systems," Nano Letters, vol. 10, pp. 1297-1301, Apr 2010. Copyright 2010 American Chemical Society.

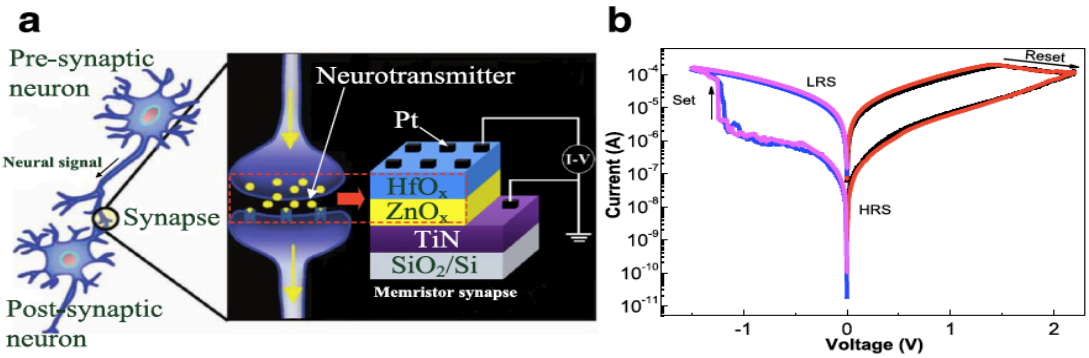

Figure 5. Reproduced from L. G. Wang, W. Zhang, Y. Chen, Y. Q. Cao, A. D. Li, and D. Wu, “Synaptic plasticity and learning behaviors mimicked in single inorganic synapses of Pt/HfOx/ZnOx/TiN memristive system,” Nanoscale Research Letters, vol 12, art. no. 65, Jan. 2017. Publisher: Springer.

2.3 PASSIVE GAS SENSING WITH METAL OXIDES

Most metal oxides are suitable for gas sensing because of inherent defective sites, which allow for the adsorption of oxygen from the ambient air. These defective sites are typically the result of vacancies [51] generated in the fabrication process. In the case of cuprous oxide (Cu_2O) and cupric oxide (CuO), for example, such sites are the result of Cu vacancies [52]. Chemical bonding between adsorbed oxygen and Cu results in the presence of holes ($O_2 \leftrightarrow O_{2^-} + h$), which leads to an accumulation layer near the grain surface. Certain gases can then react with the ionically-adsorbed oxygen (O_{2^-}/O^-) thus changing the resistance of the material.

In 2013, M. Ahmad and his colleagues fabricated and investigated simple tungsten oxide (WO_3) thin films for reproducible ethanol (C_2H_6O) sensing [53]. The films were most sensitive to a concentration of 100ppm of ethanol at 300 to 400 degrees Celsius and exhibited a reversible decrease in resistance. This change in resistance was believed to be attributed to oxygen ions which were adsorbed by the metal oxide surface from the ambient air. Upon exposure to ethanol, these adsorbed oxygen ions react with the ethanol molecules leading to the desorption of surface oxygen ions as demonstrated in the following reactions [53]:

$$CH_3CH_2OH_{(ads)} + 6O^-_{(ads)} \rightarrow 2CO_{2(g)} + 3H_2O_{(vap)} + 6e^- \quad (6)$$

$$CH_3CH_2OH_{(ads)} + 6O^{2-}_{(ads)} \rightarrow 2CO_{2(g)} + 3H_2O_{(vap)} + 12e^- \quad (7)$$

This chemical process, which is depicted in Figure 6, translates to a temporary increase in the WO_3 conductivity. When the ethanol source is cut off, the electrons and conductivity gradually decrease.

Similarly, in 2014, Hien and his colleagues investigated passive sensing of hydrogen sulfide (H_2S) via fabricated cuprous oxide (Cu_2O) structures [52]. The sensing mechanism of their samples involved an irreversible phase transformation from Cu_2O to CuS [52] through an interaction of H_2S with Cu_2O (at high temperatures) as follows:

$$2Cu_2O + O_2 \rightarrow 4CuO \quad (8)$$

$$CuO + H_2S \rightarrow CuS + H_2O \quad (9)$$

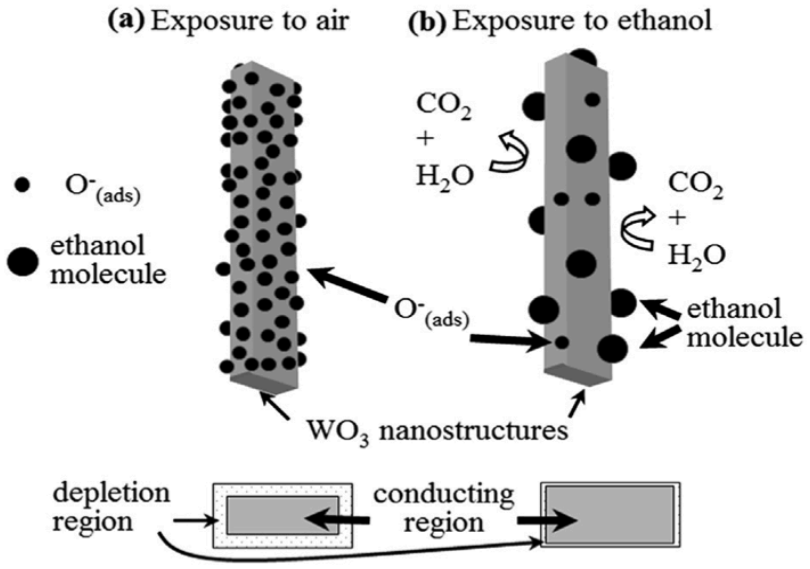

Figure 6. Reprinted from Materials Chemistry and Physics, vol. 141, M. Ahmad, A. Sadek, J. Ou, M.H. Yaacob, et al., "Facile synthesis of nanostructured WO3 thin films and their characterization for ethanol sensing," pp. 912-919, Copyright 2013, with permission from Elsevier.

Additionally, there was a removal of adsorbed oxygen ions (where $n = 1, 2$) on the oxide layer via the following reactions:

$$2H_2S_{(g)} + 3O^{n-}_{2(ads)} \rightarrow 2H_2O_{(g)} + 2SO_{2(g)} + 3ne^- \quad (10)$$

$$2SO_{2(g)} + O^{n-}_{2(ads)} \rightarrow 2SO_3 + ne^- \quad (11)$$

More importantly, Hien and his colleagues compared the sensitivities between Cu_2O thin films, Cu_2O nano-rods, and Cu_2O nano-trees, with the nano-trees outperforming the other structures. This research underlined the importance of structural considerations – particularly, surface area – when fabricating gas sensors.

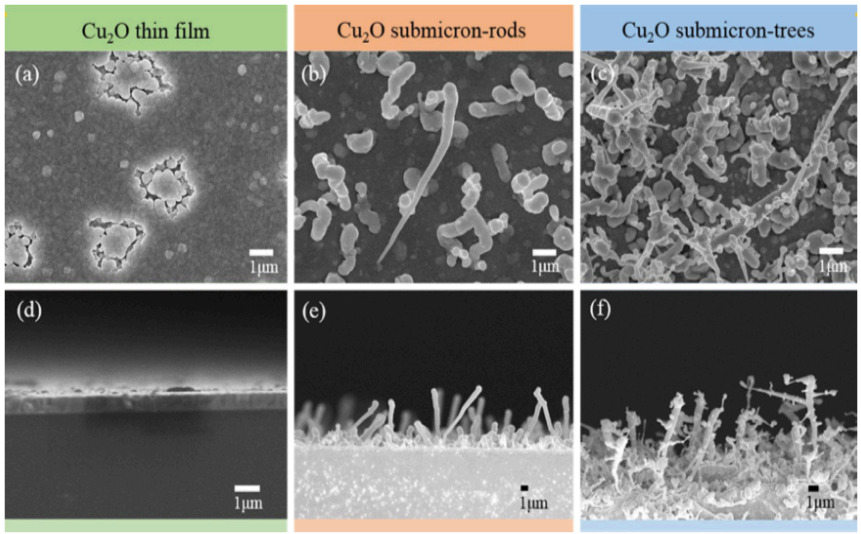

Figure 7. Reprinted from Sensors and Actuators B-Chemical, vol. 202, V. Hien, J. You, K. Jo, S. Kim, et al., "H2S-sensing properties of Cu2O submicron-sized rods and trees synthesized by radio-frequency magnetron sputtering," pp. 330-338, Copyright 2014, with permission from Elsevier.

2.4 MEMRISTORS ADVANCES IN SENSING

Though the main focus of memristor research continues to be in electronics, a few of the more recent literature have exploited memristive effects for sensing. For example, in 2012, Carrara et al demonstrated bio-sensing based on memristive signals obtained on silicon freestanding nanowires (SiNW) [54]. (Silicon nanowires already manifest a memory effect due to charge trapping occurring inside the structures [55].) As shown in Figure 8, the silicon channels were functionalized by covalent attachment of rabbit polyclonal antibodies with GPTS (glycidoxypropyltrimethoxysilane), which contributed positive charges. This contribution resulted in a virtual “all-around bio-gate” around the channels, thus affecting the hysteresis. The functionalized SiNWs were then exposed to antigens,

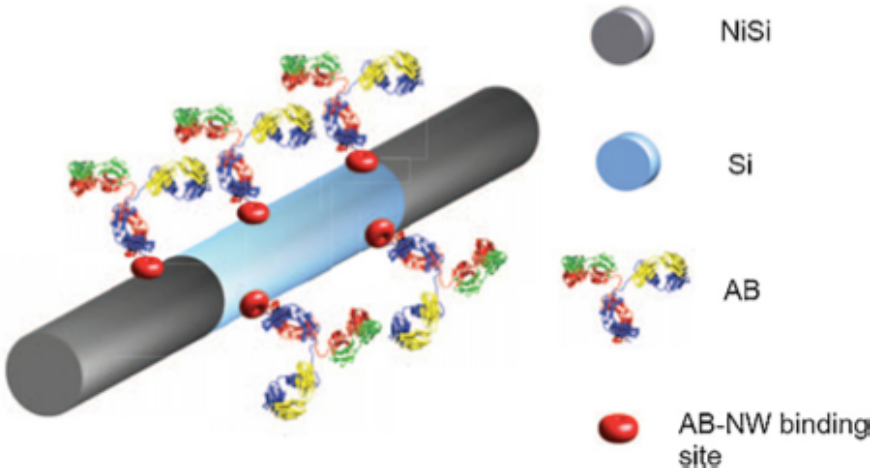

Figure 8. Reprinted from Sensors and Actuators B-Chemical, vol. 171, S. Carrara, D. Sacchetto, M. Doucey, C. Baj-Rossi, G. De Micheli, and Y. Leblebici, "Memristive-biosensors: A new detection method by using nanofabricated memristors,” pp. 449-457, Copyright 2012, with permission from Elsevier.

which further impacted the hysteresis. Thus, the authors of this study demonstrated that both probe antibodies and target antigens affect the memristive behavior of SiNWs.

Following that research, the same authors reported also using SiNWs for the detection of different concentrations of H^+, and thus pH detection in 2014 [55]. H+ ions from a solution go to form OH^- groups with the native oxide on the nanowires causing an increase in conductance and hysteresis of the wires. The observed change in the electrical properties with pH in dry conditions is related to the formation of a wet film at the nanowire surface. Ions from the initial solution were free to move in the final water thin film at the sensing interface with consequent polarization of the NW surface. Carrara and his colleagues [55] believed that the detection of hydrogen ions after the device had dried was due to adsorption of water molecules from the surrounding environment to the native oxide of the nanowire. According to the Gouy-Chapman-Stern model, “the only ion species that approaches the surface of the insulator is the H^+ ions, since these ions are small enough and poorly hydrated by water molecules, unlike the ions of other dissolved species, such as NaCl [55]”.

In 2012, Ungureanu and his colleagues demonstrated sensing via a memristor in which the resistance was not only controlled by means of voltage pulses, but also by light [56]. The device allowed for dual functions: 1) data encoding by using a certain light irradiance during the writing process and 2) capability to work as a light sensor in the ultraviolet (UV) to infrared (IR) range. To

fabricate this memristor, an Al_2O_3 film was deposited on a SiO_2/Si substrate, followed by the fabrication of Pd top contacts. As displayed in Figure 9, light-exposed Al_2O_3/SiO_2/Si rings were fabricated around the circular Pd contacts, thus allowing for light to reach the optically active Si after passing through the transparent oxide layers. Ungureanu interpreted the change in the remnant current as a modulation of the trapped electrons in the Al_2O_3 layer, where the resistivity increases upon the introduction of electrons from the Si layer. The photo-generated electrons are injected in the Al_2O_3 layer only if the electric field is high enough to overcome this energy barrier [56]. Consequently, the observed behavior of the memristor was attributed to the Al_2O_3 layer and the Al_2O_3/SiO_2 interface. Many other researchers have since looked at using light as a second control mechanism for the memristor [57, 58, 59, 60], inlcluding most recently, Wei Wang and his colleagues with a MoS_2-based memristor in 2016 [61].

Lastly, in 2010, Xiaobin Wang and others proposed a spintronic memristor acting as a temperature sensor whereby the resistance dependence was achieved through a combination of magnetoresistance and spin-torque-induced magnetization motion [62]. As shown in Figure 10, the resistance of the memristor depends on the domain wall position, which is moved through current-induced spin torque excitation. The domain wall velocity at finite temperature depends on spin-torque excitation strength and thermal fluctuation magnitude [62, 63]. (As temperature increases, domain wall velocity increases.) For temperature sensing, a biasing voltage pulse with constant magnitude is applied to the device, and the

resistance before and after the voltage pulse is measured. This resistance difference is calibrated to sense temperature.

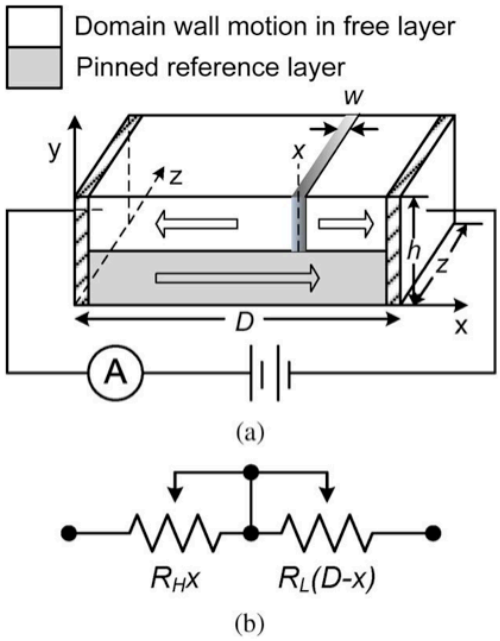

Figure 9. X. Wang, Y. Chen, Y. Gu, and H. Li, "Spintronic Memristor Temperature Sensor," IEEE Electron Device Letters, vol. 31, pp. 20-22, JAN 2010. © 2010 IEEE.

2.5 SUMMARY

In summary, this chapter was a review of literature regarding memristor research over the past decade. Much of this research involves a movement from the basic metal-insulator-metal (MIM) design of the device to a bilayer structure of the metal-oxide switching thin film for improved performance and endurance. These enhancements are essential for memristor applications in electronics, including for memory and logic. Though much memristor research continues to be

in the area of electronics, more recent literature shows an extension to applications in sensing, especially light sensing. However, there remains to be an investigation of metal-oxide based memristors for passive gas sensing, despite the inherent ability of oxides to respond to such stimuli. Thus, this dissertation, to our knowledge, is the first exploration of memristor research into this area.

REFERENCES

REFERENCES

1. J. J. Yang, M. D. Pickett, X. Li, D. A. A. Ohlberg, D. R. Stewart, and R. S. Williams. “Memristive switching mechanism for metal/oxide/metal nanodevices,” *Nature Nanotechnology*, vol. 3, pp. 429-433, Jun. 2008.

2. P. R. F. Rocha, A. Kiazadeh, D. M. De Leeuw, S. C. J. Meskers, F. Verbakel, D. M. Taylor, and H. L. Gomes. “The role of internal structure in the anomalous switching dynamics,” *Journal of Applied Physics*, vol. 113, no. 13, art no. 134504, Jul. 2013.

3. M. Ismail, C.-Y. Huang, D. Panda, C.-J. Hung, T.-L. Tsai, J.-H. Jieng, C.-A. Lin, U. Chand, A. Rana, E. Ahmed, I. Talib, M. Nadeem, and T.-Y. Tseng, “Forming-free bipolar resistive switching in nonstoichiometric ceria films,” *Nanoscale Research Letters*, vol. 9, no. 1, art. no. 45, Jan. 2014.

4. R. Waser and M. Aono, “Nanoionics-based resistive switching memories,” *Nature Materials*, vol. 6, pp. 833-840, Nov. 2007.

5. Y. Yang, S. Choi, and W. Lu, “Oxide heterostructure resistive memory,” *Nano Letters*, vol. 13, pp. 2908-2915, May 2013.

6. A. Mehonic, S. Cueff, M. Wojdak, S. Hudziak, O. Jambois, C. Labbe´, B. Garrido, R. Rizk, and A. J. Kenyon. “Resistive switching in silicon suboxide films,” *Journal of Applied Physics*, vol. 111, art. no. 074507, Feb. 2012.

7. T.-M. Tsai, K.-C. Chang, T.-C. Chang, R. Zhang, T. Wang, C.-H. Pan, and K.-H. Chen, “Resistive switching mechanism of oxygen-rich indium tin oxide resistance random access memory,” *IEEE Electron Device Letters*, vol. 37, no. 4, pp. 408-411, Apr. 2016.

8. Y.-J. Huang, S.-C. Chao, D.-H. Lien, C.-Y. Wen, J.-H. He, and S.-C. Lee, “Dual-functional memory and threshold resistive switching based on the push-pull mechanism of oxygen ions,” *Scientific Reports |*, vol. 6, art. no. 23945, Apr. 2016.

9. H. B. Lv, M. Yin, Y. L. Song, X. F. Fu, L. Tang, P. Zhou, C. H. Zhao, T. A. Tang, B. A. Chen, and Y. Y. Lin. “Forming process investigation of Cu_xO memory films,” IEEE *Electron Device Letters*, vol. 29, no. 1, pp. 47-49, Jan. 2008.

10. N. Mcdonald, S. Bishop, B. Briggs, J. V. Nostrand, and N. Cady, “Influence of the plasma oxidation power on the switching properties of Al/Cu_xO/Cu memristive devices,” *Solid-State Electronics*, vol. 78, pp. 46–50, Dec. 2012.

11. P. Zhou, H. B. Lv, M. Yin, L. Tang, Y. L. Song, T. A. Tang, Y. Y. Lin, A. Bao, A. Wu, S. Cai, H. Wu, C. Liang, and M. H. Chi, “Performance improvement of CuO_x with gradual oxygen concentration for nonvolatile memory application,” *Journal of Vacuum Science & Technology B*, vol. 26, pp. 1030-1032, Apr. 2008.

12. L. L. Wei, D. S. Shang, J. R. Sun, S. B. Lee, Z. G. Sun, and B. G. Shen, “Gradual electroforming and memristive switching in Pt/CuO_x/Si/Pt systems,” *Nanotechnology*, vol. 24, no. 32, art. no. 325202, Aug. 2013.

13. K.-D. Liang, C.-H. Huang, C.-C. Lai, J.-S. Huang, H.-W. Tsai, Y.-C. Wang, Y.-C. Shih, M.-T. Chang, S.-C. Lo, and Y.-L. Chueh, “Single CuO_x Nanowire Memristor: Forming-Free Resistive Switching Behavior,” *ACS Applied Materials & Interfaces*, vol. 6, no. 19, pp. 16537-16544, Oct. 2014.

14. P. Bousoulas, I. Michelakaki, and D. Tsoukalas, “Influence of oxygen content of room temperature TiO_{2-x} deposited films for enhanced resistive switching memory performance,” *Journal of Applied Physics*, vol. 115, no. 3, art. no. 034516, Jan. 2014.

15. K. Tsunoda, Y. Fukuzumi, J. R. Jameson, Z. Wang, P. B. Griffin, and Y. Nishi, “Bipolar resistive switching in polycrystalline TiO_2 films,” *Applied Physics Letters*, vol. 90, no. 11, art. no. 113501, Dec. 2007.

16. E. Goren, M. Ungureanu, R. Zazpe, M. Rozenberg, L. E. Hueso, P. Stoliar, Y. Tsur, and F. Casanova, “Resistive switching phenomena in TiO_x nanoparticle layers for memory applications,” *Applied Physics Letters*, vol. 105, no. 14, art. no. 143506, Jun. 2014.

17. R. Huang, L. Zhang, D. Gao, Y. Pan, S. Qin, P. Tang, Y. Cai, and Y. Wang, “Resistive switching of silicon-rich-oxide featuring high compatibility with CMOS technology for 3D stackable and embedded applications,” *Applied Physics A*, vol. 102, no. 4, pp. 927–931, Mar. 2011.

18. Y.-F. Chang, B. Fowler, Y.-C. Chen, Y.-T. Chen, Y. Wang, F. Xue, F. Zhou, and J. C. Lee, “Intrinsic SiO_x-based unipolar resistive switching memory. II. Thermal effects on charge transport and characterization of multilevel programing,” *Journal of Applied Physics*, vol. 116, no. 4, art. no. 043709, Jul. 2014.

19. Y.-F. Chang, B. Fowler, Y.-C. Chen, Y.-T. Chen, Y. Wang, F. Xue, F. Zhou, and J. C. Lee, “Intrinsic SiO_x-based unipolar resistive switching memory. I. Oxide stoichiometry effects on reversible switching and program window

optimization," *Journal of Applied Physics*, vol. 116, no. 4, art. no. 043708, Jul. 2014.

20. C.-Y. Liu, Y.-Y. Tsai, and C.-H. Lai, "Effect of plasma treatment of resistive layer on a Cu/SiO_x/Pt memory device," *Journal of Vacuum Science & Technology A: Vacuum, Surfaces, and Films*, vol. 32, no. 2, art. no. 02B111, Mar. 2014.

21. C. Ho, E. K. Lai, M. D. Lee, C. L. Pan, Y. D. Yao, K. Y. Hsieh, R. Liu, and C. Y. Lu, "A Highly Reliable Self-Aligned Graded Oxide WO_x Resistance Memory: Conduction Mechanisms and Reliability," *2007 IEEE Symposium on VLSI Technology*, 2007.

22. D. S. Shang, L. Shi, J. R. Sun, B. G. Shen, F. Zhuge, R. W. Li, and Y. G. Zhao, "Improvement of reproducible resistance switching in polycrystalline tungsten oxide films by in situ oxygen annealing," *Applied Physics Letters*, vol. 96, no. 7, art. no. 072103, Feb. 2010.

23. K. P. Biju, X. Liu, M. Siddik, S. Kim, J. Shin, I. Kim, A. Ignatiev, H. Huang, "Resistive switching characteristics and mechanism of thermally grown WO_x thin films," *Journal of Applied Phyics*, vol. 110, art. no. 064505, Sep. 2011.

24. R. Yang, K. Terabe, T. Tsuruoka, T. Hasegawa, and M. Aono, "Oxygen migration process in the interfaces during bipolar resistance switching behavior of WO_{3-x}-based nanoionics devices," *Applied Physics Letters*, vol. 100, no. 23, art. no. 231603, Apr. 2012.

25. G. Chen, C. Song, C. Chen, S. Gao, F. Zeng, and F. Pan, "Resistive Switching and Magnetic Modulation in Cobalt-Doped ZnO," *Advanced Materials*, vol. 24, no. 26, pp. 3515–3520, Aug. 2012.

26. X. Zhu, W. Su, Y. Liu, B. Hu, L. Pan, W. Lu, J. Zhang, and R.-W. Li, "Observation of Conductance Quantization in Oxide-Based Resistive Switching Memory," *Advanced Materials*, vol. 24, no. 29, pp. 3941–3946, 2012.

27. J.-J. Ke, Z.-J. Liu, C.-F. Kang, S.-J. Lin, and J.-H. He, "Surface effect on resistive switching behaviors of ZnO," *Applied Physics Letters*, vol. 99, no. 19, art. no. 192106, Jul. 2011.

28. X.B. Yan, K. Li, J. Yin, Y. D. Xia, H. X. Guo, L. Chen, and Z. G. Liua, "The resistive switching mechanism of Ag/$SrTiO_3$/Pt memory cells," *Electrochemical and Solid State Letter*s, vol. 13, pp. H87-H89, Jan. 2010.

29. Y. Li, S. Long, M. Zhang, Q. Liu, L. Shao, S. Zhang, Y. Wang, Q. Zuo, S. Liu, and M. Liu, "Resistive Switching Properties of Au/ZrO_2/Ag Structure for Low-Voltage Nonvolatile Memory Applications," *IEEE Electron Device Letters*, vol. 31, pp. 117-119, Feb. 2010.

30. N. Ge, M-X Zhang, L. Zhang, J. Joshua Yang*, Z. Li, and R S. Williams, "Electrode-material dependent switching in TaO_x memristors", *Semiconductor Science and Technology*, vol. 29, no. 10, art. no.104003, Oct. 2014.

31. C. Schindler, S. C. P. Thermadam, R. Waser, and M. N. Kozicki, "Bipolar and unipolar resistive switching in Cu-doped SiO_2," *IEEE Transactions Electron Devices*, vol. 54, pp. 2762-2768, Sep 2007.

32. T. Sakamoto, K. Lister, N. Banno, T. Hasegawa, K. Terabe, and M. Aono, "Electronic transport in Ta_2O_5 resistive switch," *Applied Physics Letters*, vol. 91, art. no. 092110, Aug 2007.

33. Y. Li, S. Long, Q. Liu, Q. Wang, M. Zhang, H. Lv, L. Shao, Y. Wang, S. Zhang, Q. Zuo, S. Liu, and M. Liu, "Nonvolatile multilevel memory effect in Cu/WO_3/Pt device structures," *Physica Status Solidi (RRL) – Rapid Research Letters*, vol. 4, no. 5-6, pp. 124-126, Apr 2010.

34. H. Z. Zhang, D. S. Ang, K. S. Yew, and X. P. Wang, "Enhanced stability of complementary resistance switching in the TiN/HfO_x/TiN resistive random-access memory device via interface engineering," *Applied Physics Letters*, vol. 108, art. no. 083505, Feb 2016.

35. C.H. Huang, J. S. Huang, S. M. Lin, W. Y. Chang, J. H. He, and Y. L. Chueh, "ZnO_{1-x} nanorod arrays/ZnO thin film bilayer structure: from homojunction diode and high-performance memristor to complementary 1D1R application," *ACS Nano*, vol. 6, no. 9, pp. 8407-8414, Aug. 2012.

36. S.-M. Lin, J.-S. Huang, W.-C. Chang, T.-C. Hou,. H.-W. Huang, C.-H. Huang, S.- J. Lin and Y.-L. Chueh, "Single-step formation of ZnO/$ZnWO_x$ bilayer structure via interfacial engineering for high performance and low energy consumption resistive memory with controllable high resistance states," *ACS Applied Materials & Interfaces*, vol. 5, no. 16, pp. 7831-7837, Aug. 2013.

37. M.J. Lee, C. B. Lee, D. Lee, S. R. Lee, M. Chang, J. H. Hur, Y. B. Kim, C. J. Kim, D. H. Seo, S. Seo, U. I. Chung, I. K. Yoo, and K. Kim, "A fast, high-endurance and scalable non-volatile memory device made from asymmetric TaO_2O_{5-x} /TaO_{2-x} bilayer structures," *Nature Materials*, vol. 10, no. 8, pp. 625-630, Jul. 2011.

38. C Pi, Y. Ren, Z. Q. Liu, and W. K. Chima, “Unipolar memristive switching in yttrium oxide and RESET current reduction using a yttrium interlayer,” *Electrochemical and Solid-State Letters*, vol. 15, no. 3, pp. G5-G7, Dec. 2011.

39. S. Gao, F. Zeng, M. Wang, G. Wang, C. Song and F. Pan, “Tuning the switching behavior of binary oxide-based resistive memory devices by inserting an ultra-thin chemically active metal nanolayer: a case study on the Ta_2O_5–Ta system,” *Physical Chemistry Chemical Physics*, vol. 17, no. 19, pp. 12849-12856, 2015.

40. A. Prakash, S. Maikap, C. S. Lai, T. C. Tien, W. S. Chen, H. Y. Lee, F. T. Chen, M.-J. Kao, and M.-J. Tsai, “Bipolar resistive switching memory using bilayer TaO_x/WO_x films,” *Solid-State Electronics*, vol. 77, pp. 35-40, Nov. 2012.

41. A. Siemon, T. Breuer, N. Aslam, S. Ferch, W. Kim, J. van den Hurk, V. Rana, S. Hoffmann-Eifert, R. Waser, S. Menzel, E. Linn, “Realization of boolean logic functionality using redox-based memristive devices,” *Advanced Functional Materials*, vol. 25, pp. 6414-6423, Oct. 2015.

42. D.B. Strukov and H. Kohlstedt, “Resistive switching phenomena in thin films: Materials, devices, and applications,” *MRS Bulletin*, vol. 37, pp. 108-114, Feb. 2012.

43. J. Hou, S.S. Nonnenmann, W. Qin, and D.A. Bonnell, “Size dependence of resistive switching at nanoscale metal-oxide interfaces", *Advanced Functional Materials*, vol. 24, no. 26, pp. 4113-4118, Jul. 2014.

44. R. Dittmann, R. Muenstermann, I.K. D. Park, T. Menke, J. Mayer, A. Besmehn, F. Kronast, C. Schneider, and R. Waser, “Scaling potential of local redox processes in memristive $SrTiO_3$ thin-film devices,” *Proceedings of the IEEE 100*, vol. 6, pp. 1979-1990, Jun. 2012.

45. Y. Yang, P. Gao, S. Gaba, T. Chang, X. Pan, and W. Lu, “Observation of conducting filament growth in nanoscale resistive memories,” *Nature Communications*, vol. 3, art. no. 732, Mar. 2012.

46. S. Jo, T. Chang, I. Ebong, B. Bhadviya, P. Mazumder, and W. Lu, "Nanoscale memristor device as synapse in neuromorphic systems," *Nano Letters*, vol. 10, pp. 1297-1301, Apr. 2010.

47. L. G. Wang, W. Zhang, Y. Chen, Y. Q. Cao, A. D. Li, and D. Wu, “Synaptic plasticity and learning behaviors mimicked in single inorganic synapses of

Pt/HfO_x/ZnO_x/TiN memristive system," *Nanoscale Research Letters*, vol 12, art. no. 65, Jan. 2017.

48. T. Chang, Y. Yang, and W. Lu, "Building neuromorphic circuits with memristive devices," *IEEE Circuits and Systems Magazine*, vol. 13, pp. 56-73, 2013.

49. K. Cantley, A. Subramaniam, H. Stiegler, R. Chapman, and E. Vogel, "Neural learning circuits utilizing nano-crystalline silicon transistors and memristors," *IEEE Transactions on Neural Networks and Learning Systems*, vol. 23, pp. 565-573, Apr. 2012.

50. T. Chang, S-H Jo, K-H Kim, P. Sheridan, S. Gaba, and W. Lu, "Synaptic behaviors and modeling of a metal oxide memristive device," *Applied Physics A*, vol. 102, no. 4, pp. 851-855, Mar. 2011.

51. N. Barsan and U. Weimar, "Conduction model of metal oxide gas sensors," *Journal of Electroceramics*, vol. 7, no. 3, pp. 143–167, Dec. 2001.

52. V. Hien, J. You, K. Jo, S. Kim, J. Lee, J. Kim, et al., "H_2S-sensing properties of Cu_2O submicron-sized rods and trees synthesized by radio-frequency magnetron sputtering," *Sensors and Actuators B-Chemical*, vol. 202, pp. 330-338, Oct. 2014.

53. M. Ahmad, A. Sadek, J. Ou, M.H. Yaacob, et al., "Facile synthesis of nanostructured WO_3 thin films and their characterization for ethanol sensing," *Materials Chemistry and Physics*, vol. 141, pp. 912-919, Jun. 2013.

54. S. Carrara, D. Sacchetto, M. Doucey, C. Baj-Rossi, G. De Micheli, and Y. Leblebici, "Memristive-biosensors: A new detection method by using nanofabricated memristors," *Sensors and Actuators B-Chemical*, vol. 171, pp. 449-457, Sep. 2012.

55. F. Puppo, M. Di Ventra, G. De Micheli, and S. Carrara, "Memristive sensors for pH measure in dry conditions," *Surface Science*, vol. 624, pp. 76-79, Jun. 2014.

56. M. Ungureanu, R. Zazpe, F. Golmar, P. Stoliar, R. Llopis, F. Casanova, et al., "A light-controlled resistive switching memory," *Advanced Materials*, vol. 24, pp. 2496-2500, May 2012.

57. B. Sun, X. Li, D. Liang, and P. Chen, “Effect of visible-light illumination on resistive switching characteristics in Ag/$Ce_2W_3O_{12}$/FTO devices,” *Chemical Physics Letters*, vol. 643, pp. 66-70, Jan. 2016.

58. A. Chiolerio, I. Roppolo, V. Cauda, M. Crepaldi, S. Bocchini, K. Bejtka, A. Verna, and C. F. Pirri, “Ultraviolet mem-sensors: Flexible anisotropic composites featuring giant photocurrent enhancement,” *Nano Research*, vol. 8, no. 6, pp. 1956-1963, Jun. 2015.

59. B. Sun, J. Wu, X. Jia, F. Lou, and P. Chen, “Preparation and light-controlled resistive switching memory behavior of $CuCr_2O_4$,” *Journal of Sol-Gel Science and Technology*, vol. 75, no. 3, pp. 664-669, May 2015.

60. B. Sun, X. J. Jia, J. H. Wu, and P. Chen, “Photo-electron double regulated resistive switching memory behaviors of Ag/$CuWO_4$/FTO device,” *Solid State Communications*, vol. 223, pp. 1-5, Dec. 2015.

61. W. Wang, G. N. Panin, X. Fu, L. Zhang, P. Ilanchezhiyan, V. O. Pelenovich, D. Fu and T. W. Kang, “MoS_2 memristor with photoresistive switching,” *Scientific Reports*, vol. 6, pp. 1-10, Nov. 2016.

62. X. Wang, Y. Chen, Y. Gu, and H. Li, "Spintronic memristor temperature sensor," *IEEE Electron Device Letters*, vol. 31, pp. 20-22, Jan. 2010.

63. H. Mahmoudi, V. Sverdlov, and S. Selberherr, "Influence of geometry on the memristive behavior of the domain wall spintronic memristors and its applications for measurement," *Journal of Superconductivity and Novel Magnetism*, vol. 26, pp. 1745-1748, May 2013.

CHAPTER 3 MEMRISTOR DESIGN AND FABRICATION

3.1 INTRODUCTION

The metal-insulator-metal (MIM) memristor design was chosen for ease and repeatability in fabrication for this project. A nonstoichiometric metal oxide (copper oxide) was sandwiched between an inactive metal electrode (tungsten) and an active electrode (copper). Further design and fabrication details are covered in this chapter.

3.2 PROTOTYPE MEMRISTOR DESIGN

3.2.1 Design Overview

The prototype was designed using a crossbar array structure, as demonstrated in Fig. 11, to increase device yield per substrate. Five 15-µm copper (Cu) bottom electrodes were overlaid with non-stoichiometric copper oxide (Cu_xO) switching layers. They shared a 10-µm tungsten (W) top electrode, which resulted in five 10-µm-x-15-µm memristors per substrate. As depicted in the schematic, a portion of the Cu_xO layer is left uncovered by the W top layer to allow for sensing via oxygen exposure. Figure 12 displays a scanning electron microscopy (SEM) image of the fabricated device. This design overview is reproduced from publication [1].

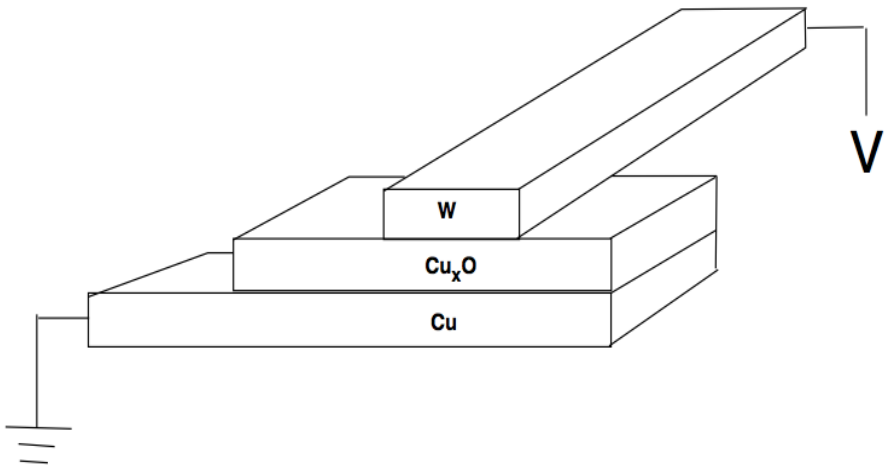

Figure 10. Initial memristor design. During testing of the memristor, the bottom electrode is grounded.

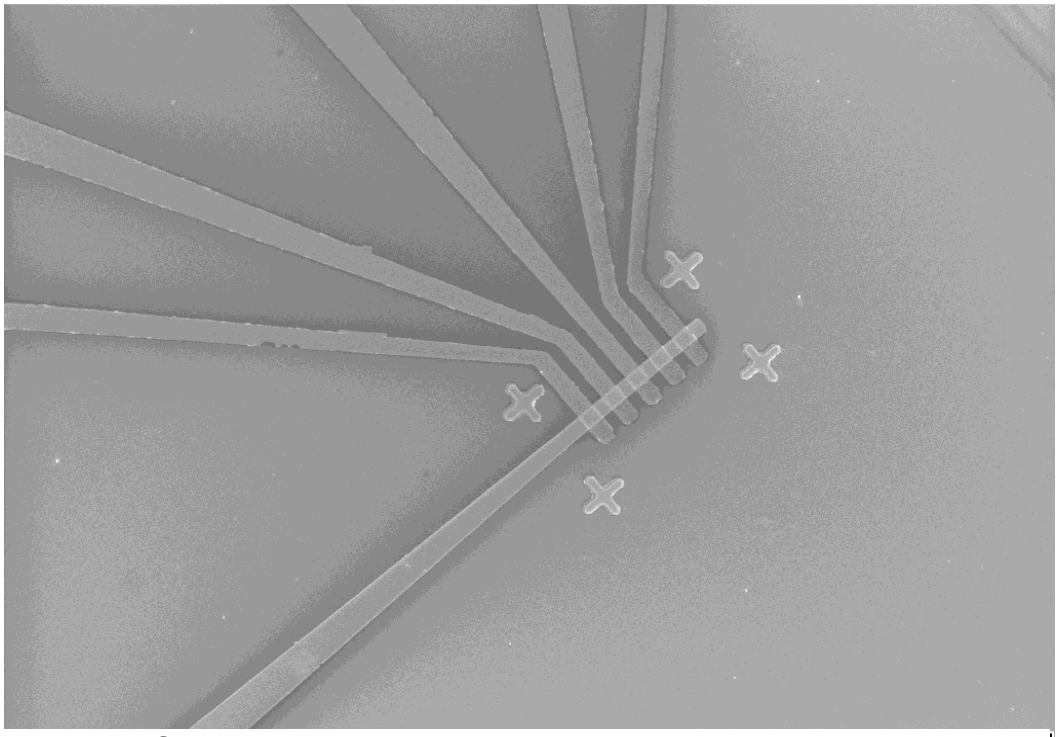

Figure 11. SEM of prototype – crossbar array memristor There are a total of five bottom electrodes and one top electrode. The copper oxide switching layer (which is not easily seen here) sits between the copper bottom electrode and top tungsten electrode with regions exposed for sensing. This design results in five 10-micron-x-15-micron memristors.

3.2.2 Fabrication Process

The fabrication process for this initial memristor was as follows and is reproduced from publication [1]:

Silicon substrates underwent plasma-enhanced chemical vapor deposition of 500-nanometer thick silicon dioxide (SiO_2) via an Oxford PECVD System PlasmaLab 80 plus. This process was necessary to provide an insulating layer between the to-be-deposited Cu bottom electrodes and the substrate. The

substrates were then subjected to photolithography for patterning of these bottom electrodes. W/Cu_xO/Cu devices were prepared on the SiO_2/Si substrates using DC magnetron sputtering via a Kurt Lesker Axxis PVD System at room temperature. A copper layer of 30 nanometers was first deposited onto the pattern using a 99.9% pure Cu target, which was presputtered to remove any native oxide layer. The Cu electrodes were then partially shielded, and a non-stoichiometric copper oxide (Cu_xO) switching layer was deposited using the same Cu target but with an Ar/O_2 mixture injected into the system. The parameters for the Cu_xO deposition were as follows: power of 200 Watts, ~27 cubic centimeters per minute of argon, and ~7 cubic centimeters per minute of oxygen. After deposition of the Cu and Cu_xO layers, lift-off was performed to complete patterning of the bottom electrode and switching layer, respectively. The substrate was then prepared for patterning of the top electrode by photolithography. A tungsten (W) layer of 30 nanometers was sputtered using a 99.9% pure W target that had been pre-sputtered to remove any oxide layer or surface contamination. A final metal lift-off was then performed to complete the W top electrode. The fabrication process is illustrated in Fig. 13.

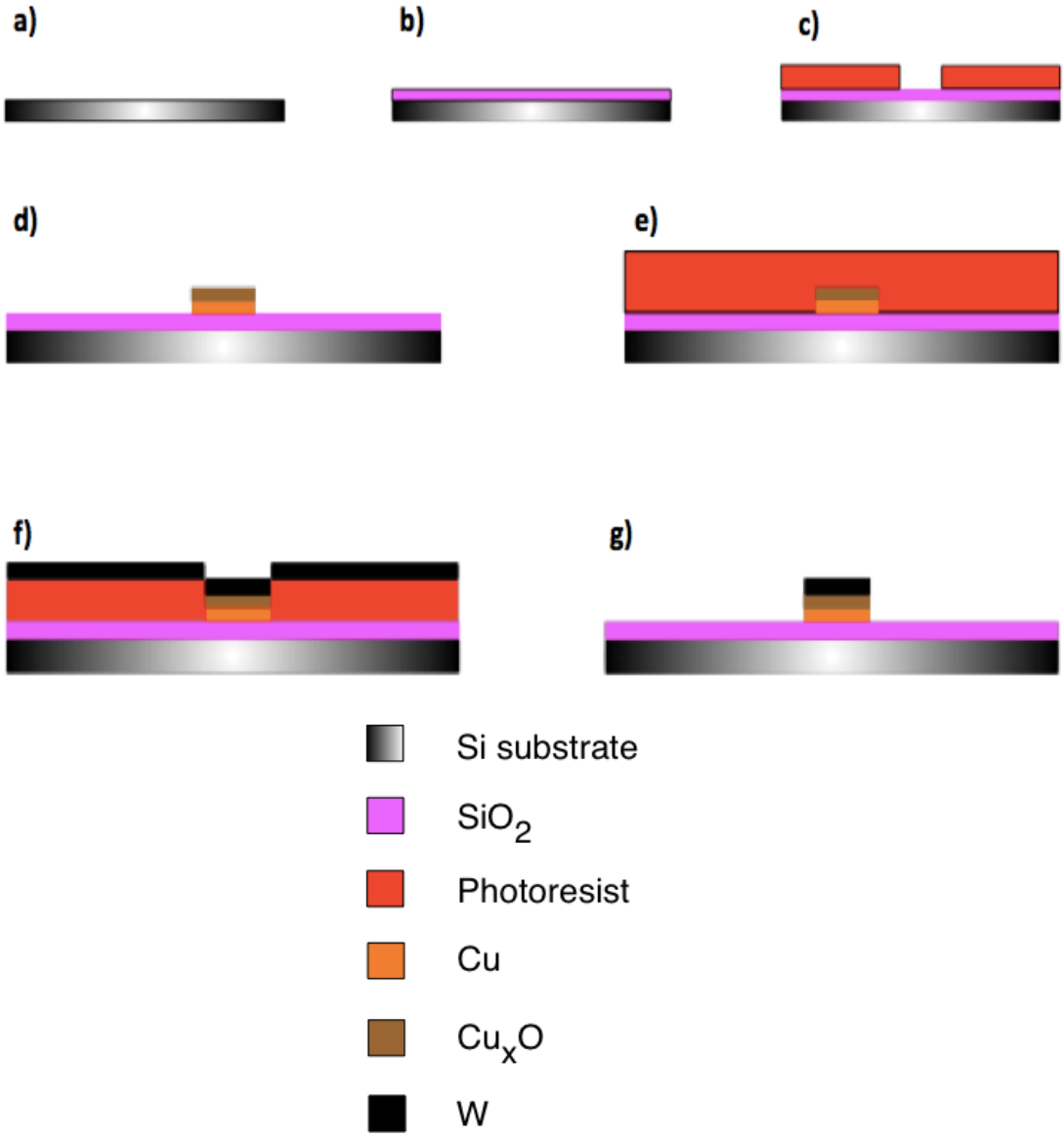

Figure 12. Fabrication process. (a) The fabrication begins on a clean silicon die. (b) PECVD of silicon dioxide is performed to provide an insulating layer between the memristor and silicon surface. (c) Photoresist is spun and baked onto the die followed by photolithography. (d) Cu and CuxO are deposited and lift-off reveals a bottom electrode and switching layer, respectively. (e-f) The procedures are repeated for the W top electrode.

3.2.2 Maskplate Design

In order to achieve this memristor design, a maskplate was drawn using Nanometer Pattern Generation Software (NPGS) in combination with CAD software for construction by PhotoSciences. The maskplate was to consist of two sections as pictured in Figures 14 and 15. Each section corresponded to a layer of metal that would be exposed to ultraviolet light (via the mask aligner) and remain after metal lift-off.

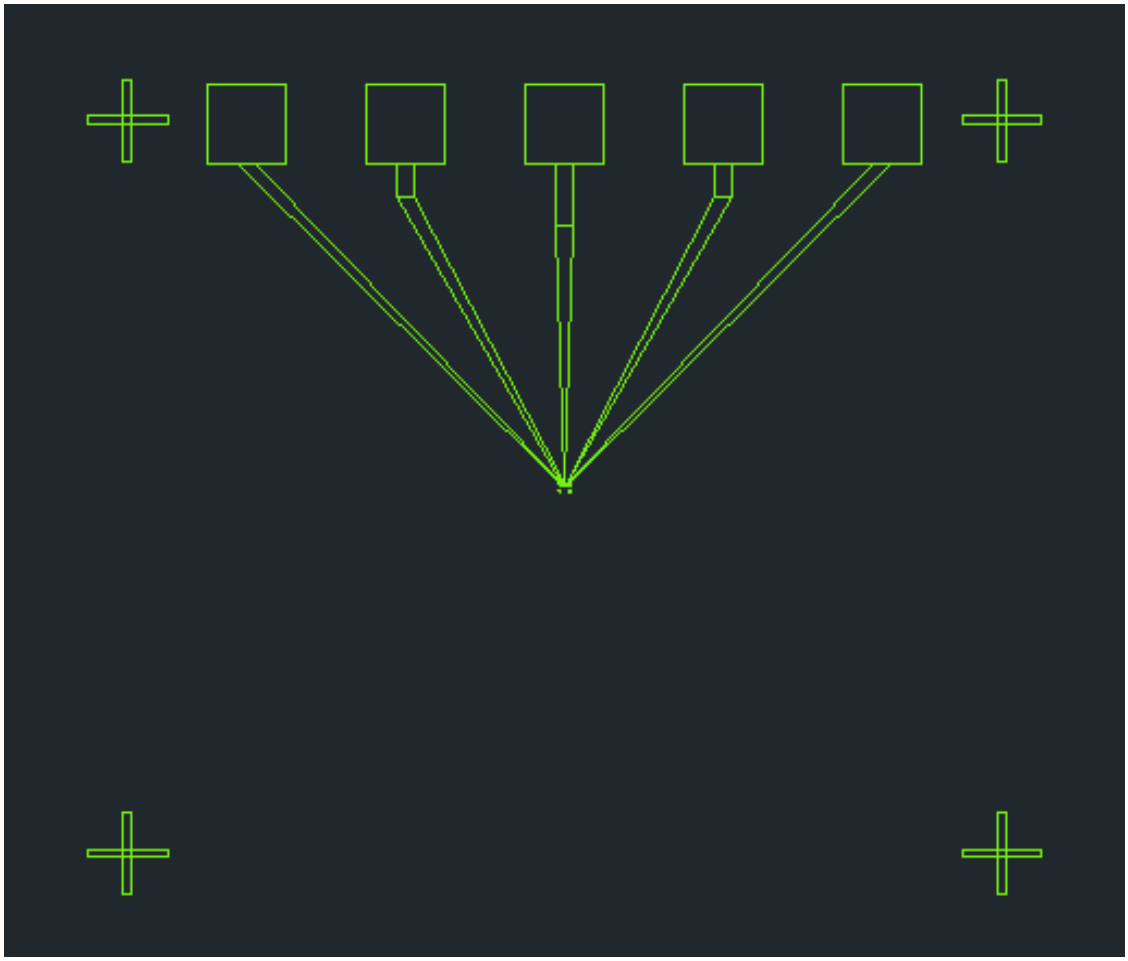

Figure 13. Maskplate design for layering of copper electrodes and contacts.

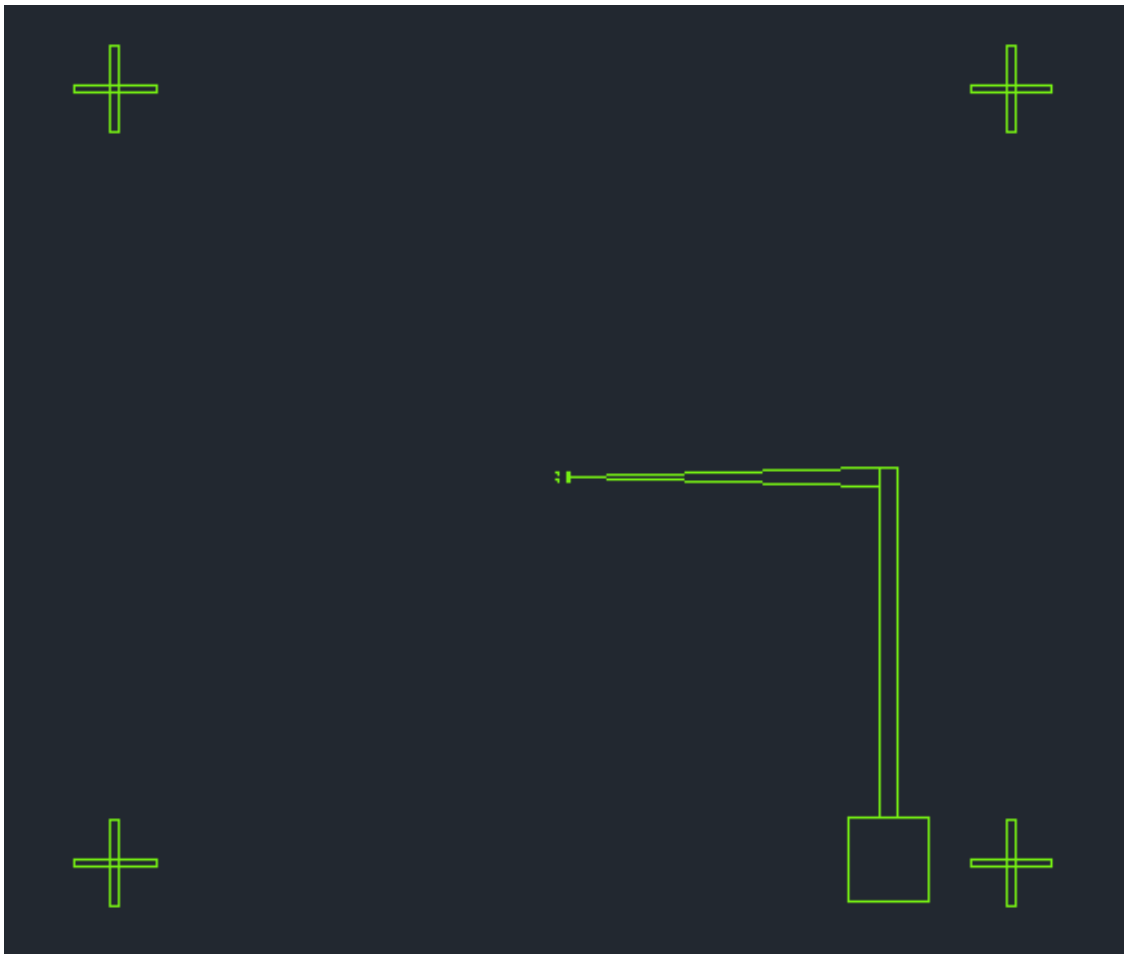

Figure 14. Maskplate design for layering of tungsten electrode and contact.

3.3 IMPROVED DEVICE - MEMRISTOR WITH SUB-MICRON HOLES

3.3.1 Design Overview

The device, which is shown in Fig. 16, was designed using a larger crossbar array structure to increase memristor yield. Ten 10-um bottom electrodes were overlaid with switching layers followed by ten 10-um top electrodes resulting in 100 memristors per substrate. Additionally, holes were etched through the tungsten top layer to allow for sensing via oxygen exposure to the copper oxide layer, as illustrated in Fig. 17. This design overview references publications [2] and [3].

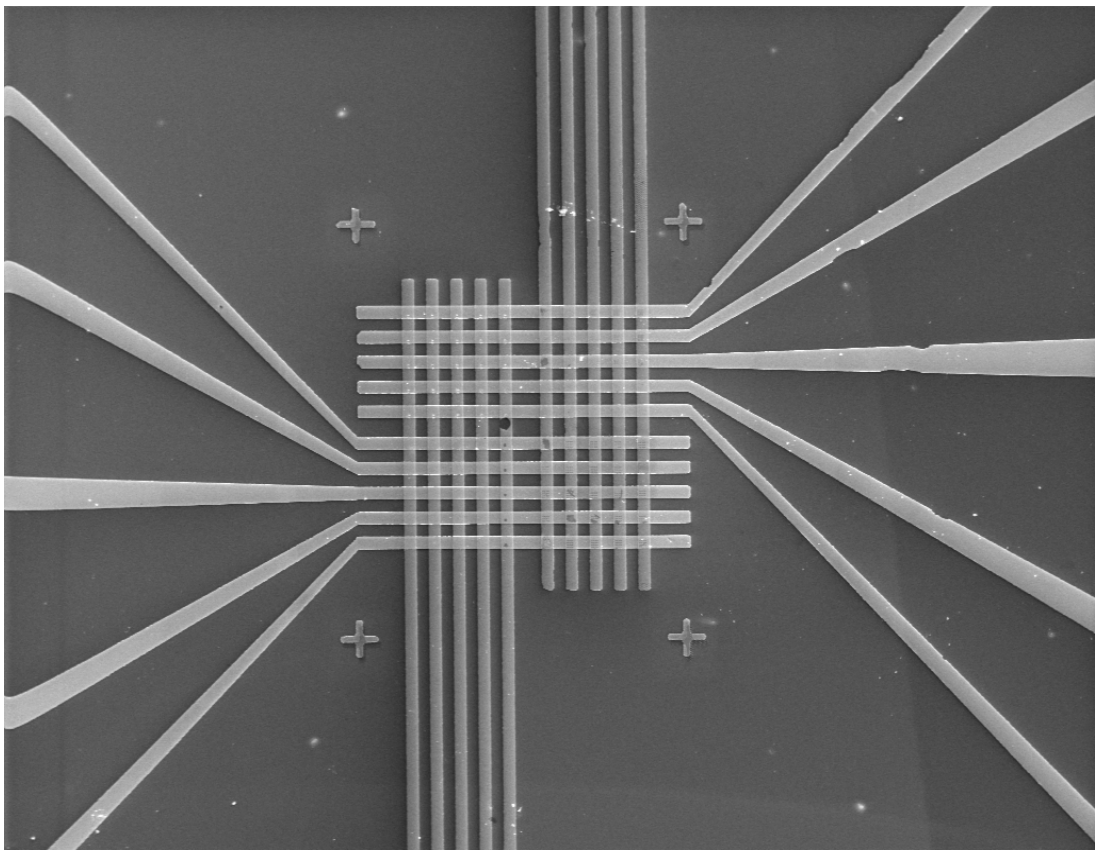

Figure 15. SEM of memristor array.

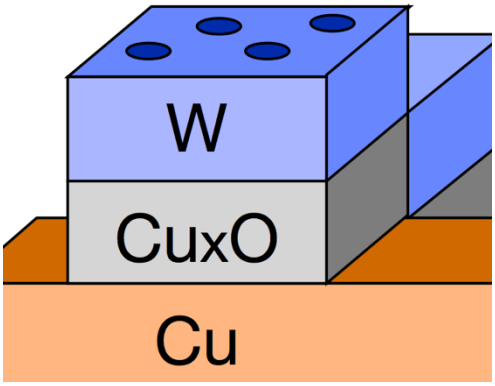

Figure 16. Holes in tungsten layer.

3.3.2 Fabrication Process

Fabrication of the device consisted of the following procedure and is reproduced from publications [2] and [3]:

Silicon substrates underwent plasma-enhanced chemical vapor deposition of 500-nm thick SiO_2 to provide an insulating layer. Next, photolithography was performed to pattern the bottom electrodes. A 30-nm W layer was then deposited onto the SiO_2/Si substrate using a 99.9% pure W target, which had been pre-sputtered to remove any native oxide layer or surface contamination. Next, a 30-nm Cu layer was deposited — except onto the W contact pads — using a 99.9% pure Cu target, which had also been pre-sputtered. (W contact pads explained further in Section 3.3.5) After deposition of the W and Cu layers, lift-off was performed to complete patterning of the bottom electrode with contacts. The substrate was then prepared for patterning of the switching layer and top electrodes by photolithography. A 40-nm layer of oxygen-deficient copper oxide,

Cu_xO, was then deposited using a pre-sputtered 99.9% Cu target with a mixture of Ar and O_2 gases. Next, a W layer of 30 nm was sputtered, and a final metal lift-off was performed to complete the Cu_xO switching layer and W top electrode.

3.3.3 Maskplate Design

A second maskplate was constructed for this new memristor design by PhotoSciences after sending new drawings created with Nanometer Pattern Generation Software (NPGS) in combination with CAD software. These drawings are included in the following figures:

.

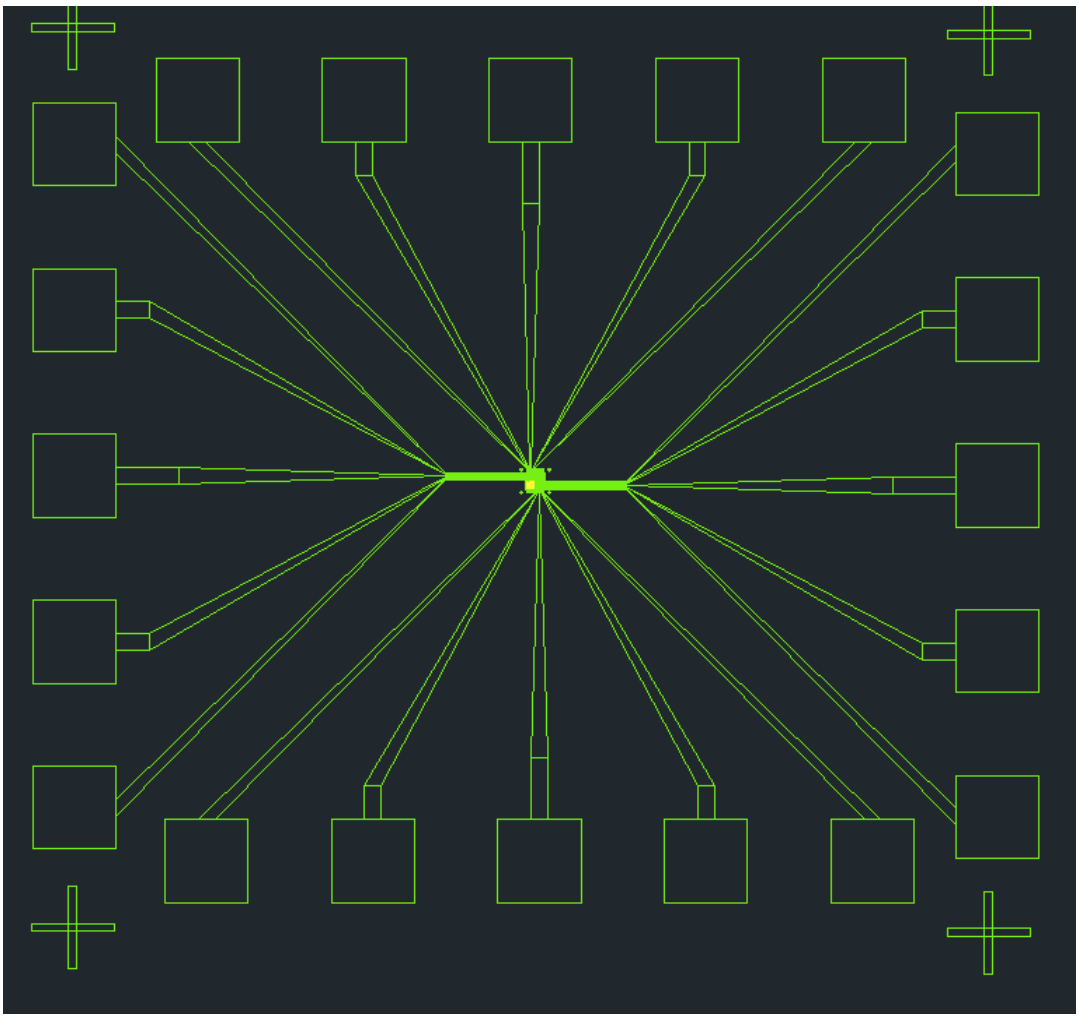

Figure 17. Maskplate design for photolithography. This is the complete design.

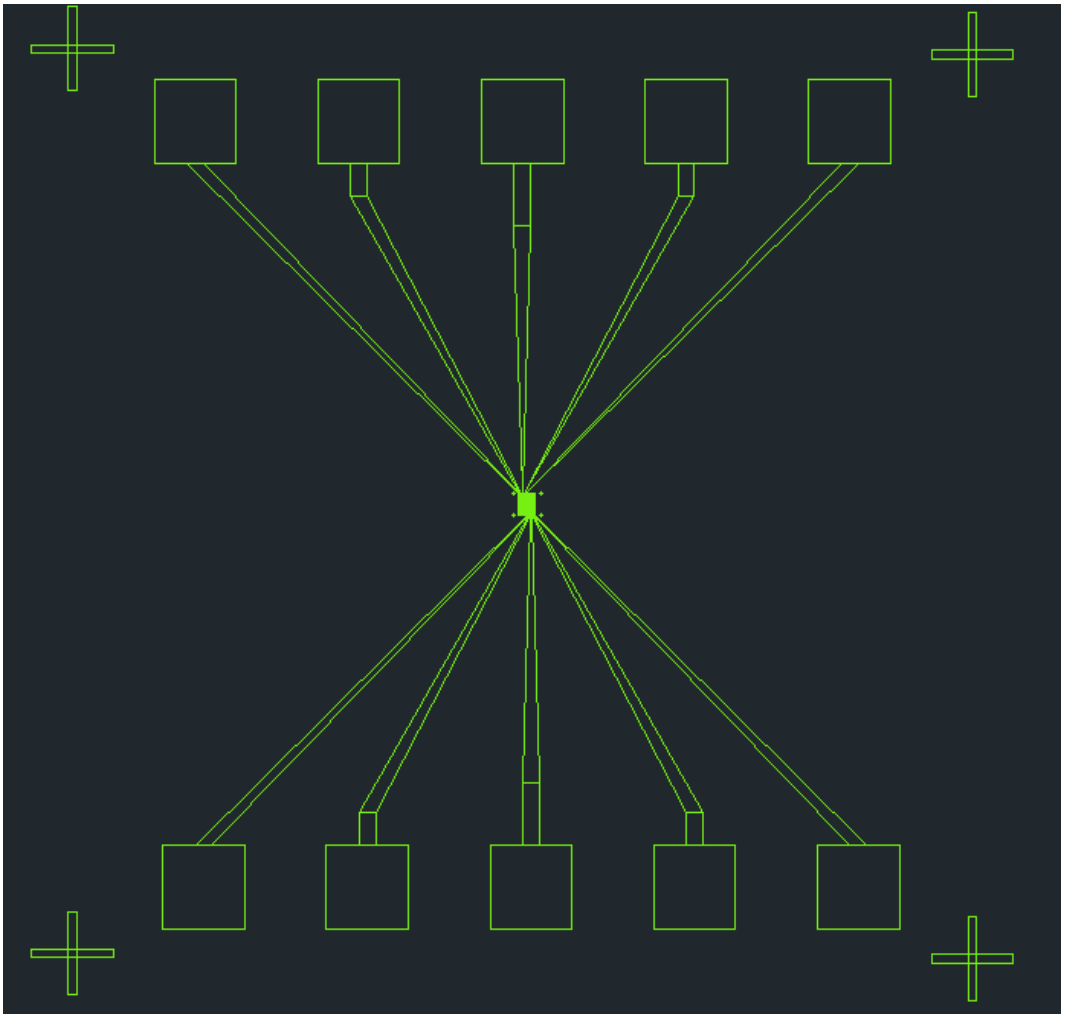

Figure 18. Maskplate design for photolithography. This is the first layer consisting of the bottom electrodes, bottom contacts, and markers.

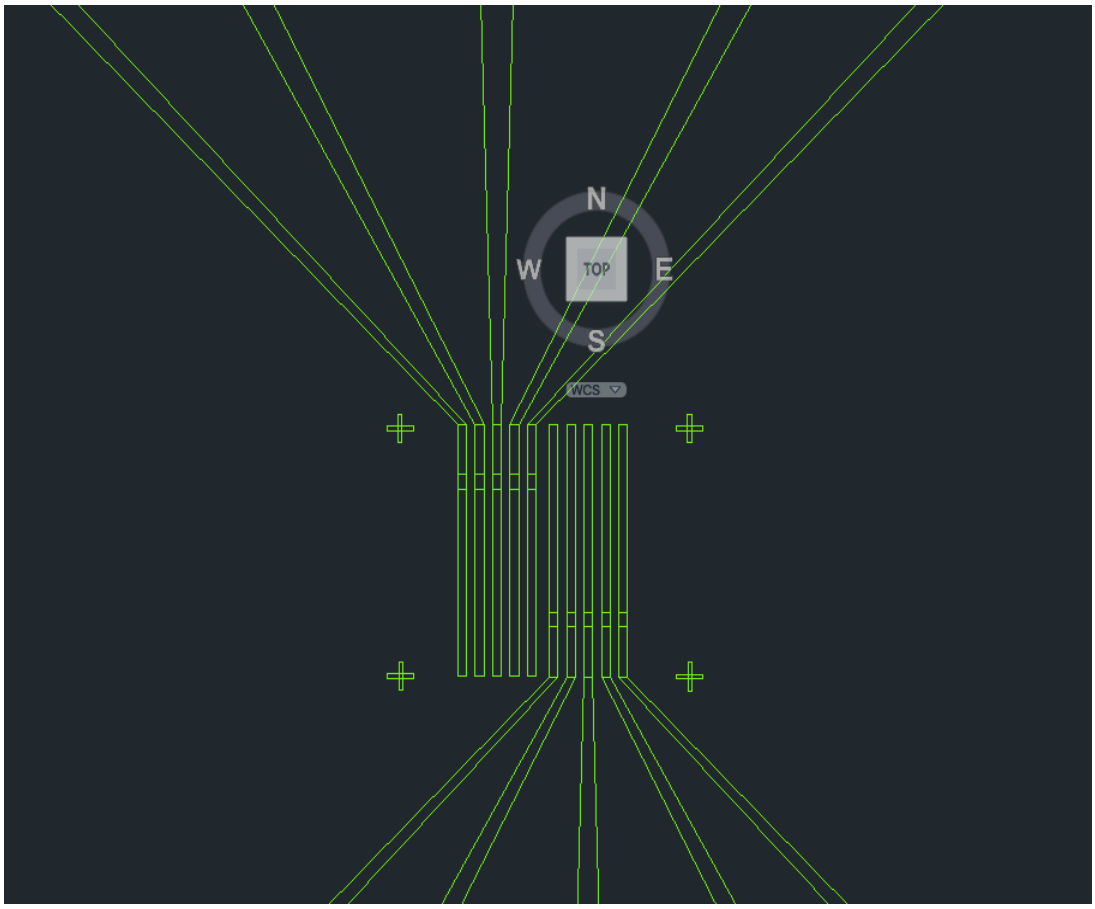

Figure 19. Closeup of the first layer.

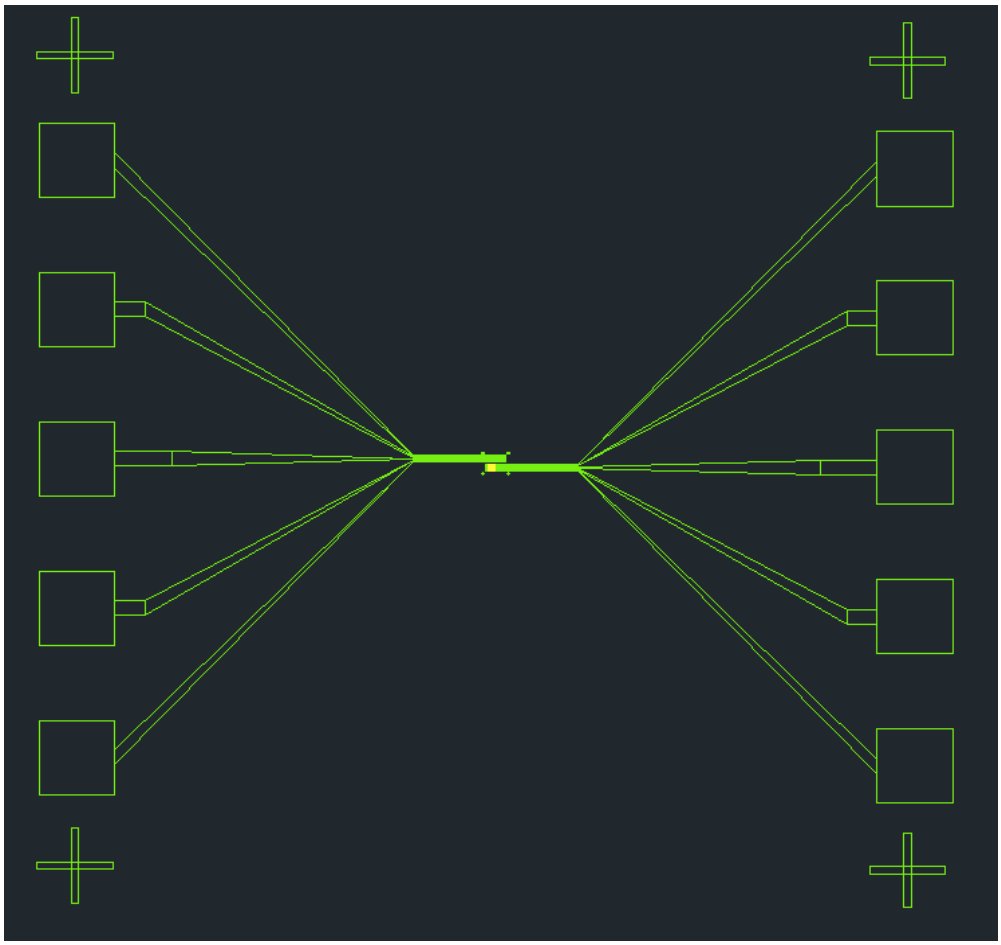

Figure 20. Maskplate design for photolithography. This is the first layer consisting of the top electrodes, top contacts, and markers.

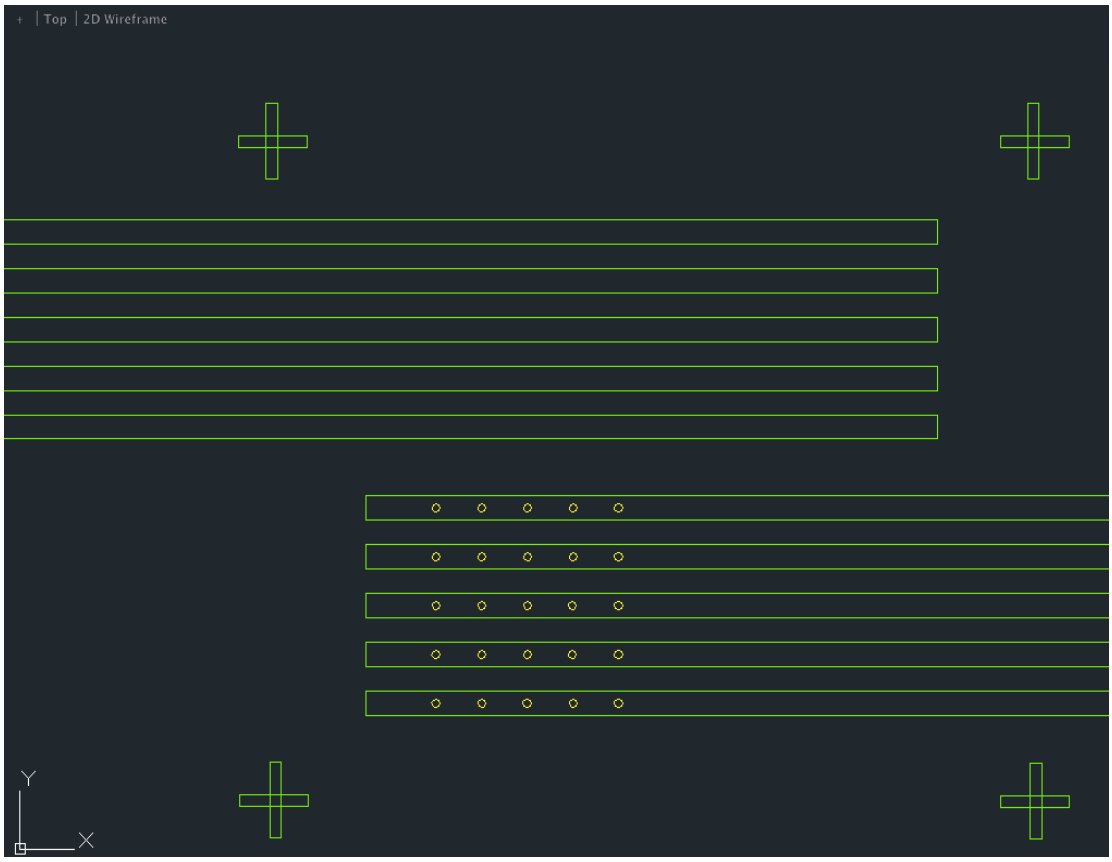

Figure 21. Closeup of the second layer.

3.3.4 Improving Sensitivity with Holes

Electron beam lithography was employed in order to pattern sub-micron holes into the tungsten layer for gas sensing. (This sub-section is reproduced from publications [2] and [3].) The crossbar structure was visually divided into four quadrants of twenty-five devices each. One quadrant was patterned with meshes of 300-nm diameter holes while a second quadrant was patterned with meshes of 700-nm diameter holes. A third quadrant consisting of larger holes was used as a visual guide. The remaining quadrant was left unpatterned for comparison.

After patterning, the device was submerged in a $NH_4OH:H_2O_2:H_2O$ (1:100:100) solution for a total of 11 seconds in order to wet etch the sub-micron holes. The device was then thoroughly rinsed in DI water to stop etching. Figs. 27-28 is an SEM image of the etched 500-nm (actual of 700-nm) holes, which will be referred to as “micro meshes” for the remainder of this paper. Twelve testable devices were successfully etched in this case. Figures 29-31 is an SEM image of successfully etched 200-nm (actual of 300-nm) holes, which will be referred to as “nano meshes” for the remainder of this paper. Most of the meshes were under-etched or not etched at all, while a few were over-etched, which resulted in only two testable devices.

.

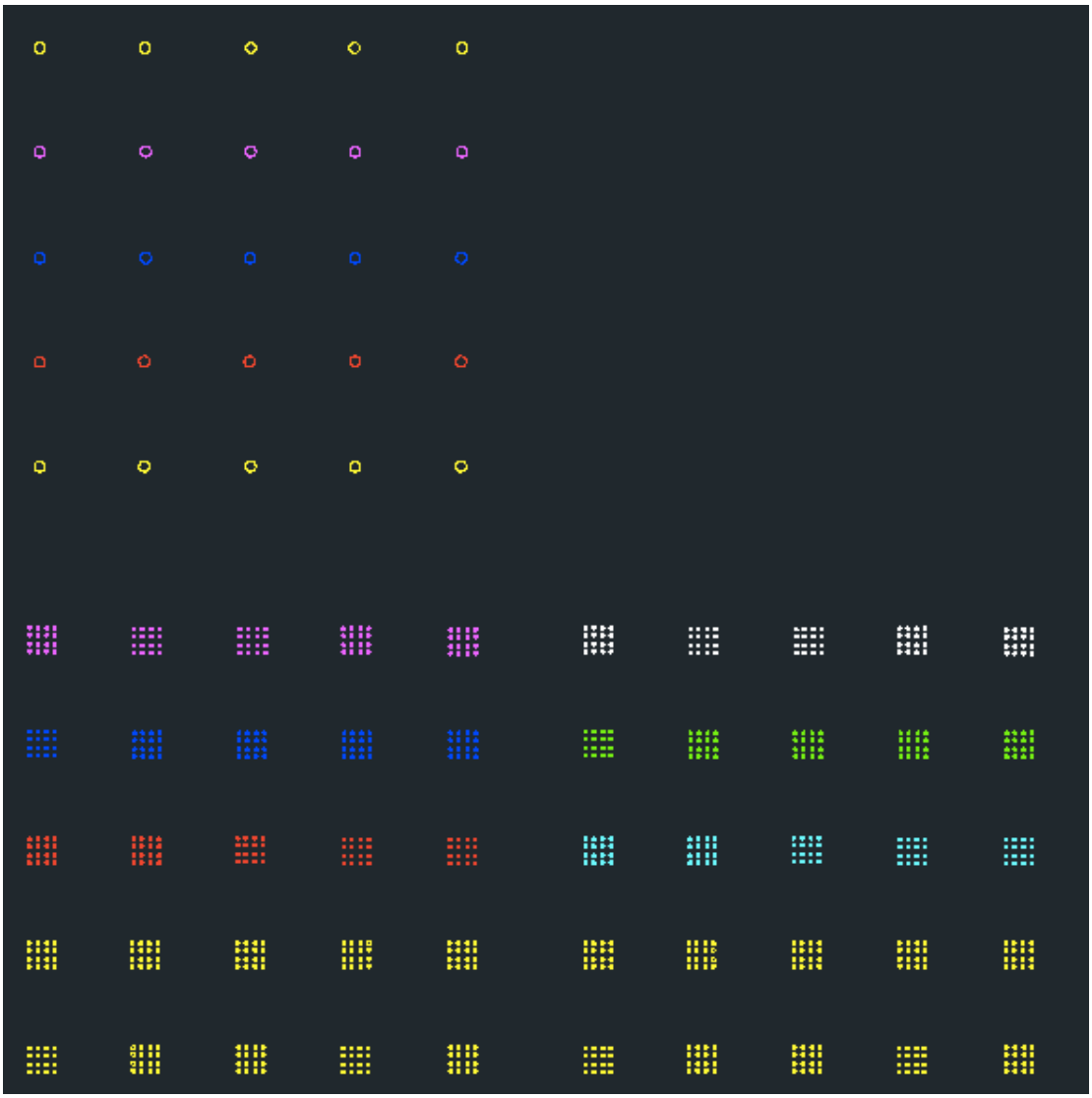

Figure 22. Initial NPGS design with two sets of 4x4 500-nm holes (in two quadrants) and one set of larger holes.

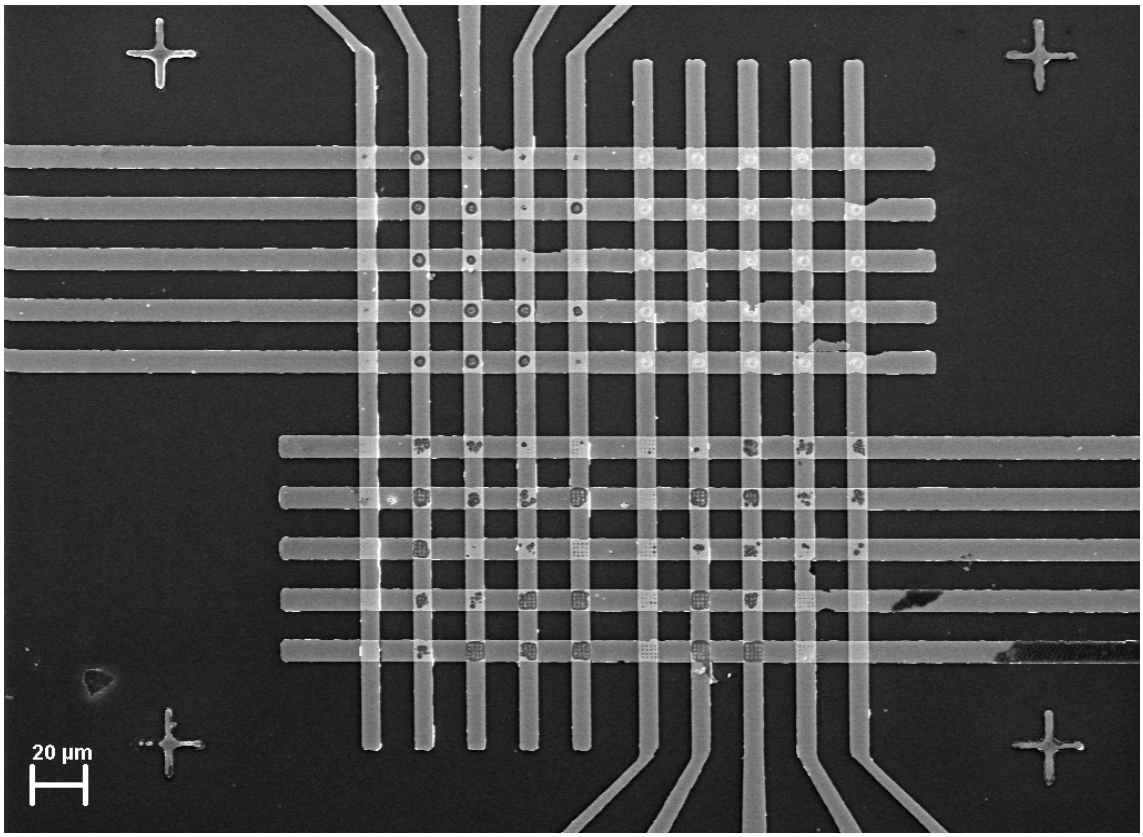

Figure 23. Failed etching attempt. Note that much of the tungsten layer has been etched through for numerous memristors.

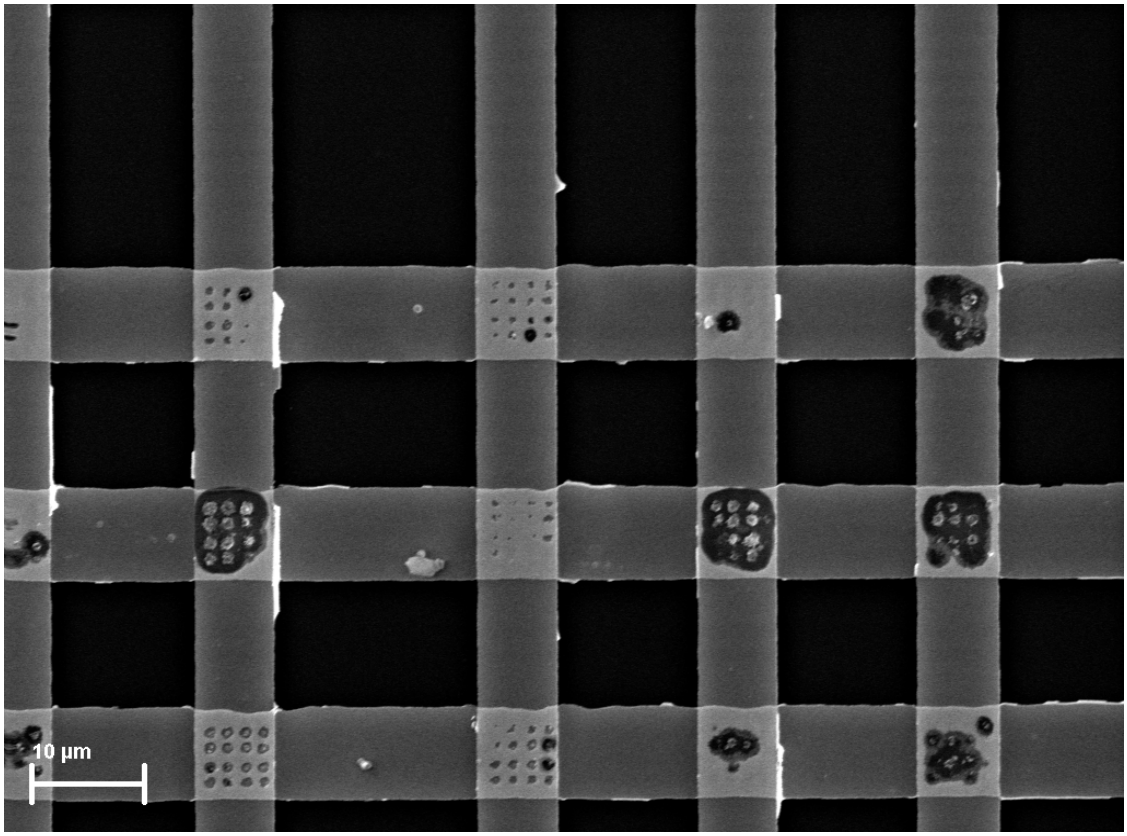

Figure 24. Closeup of failed etching attempt.

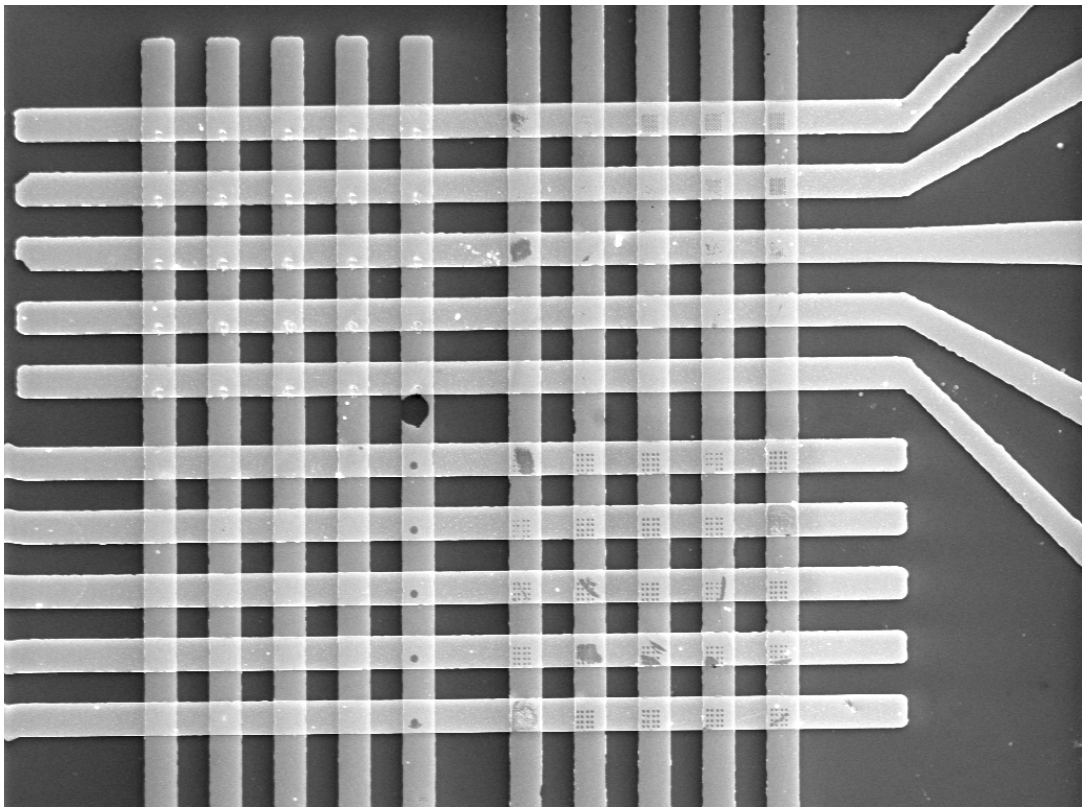

Figure 25. Improved attempt.

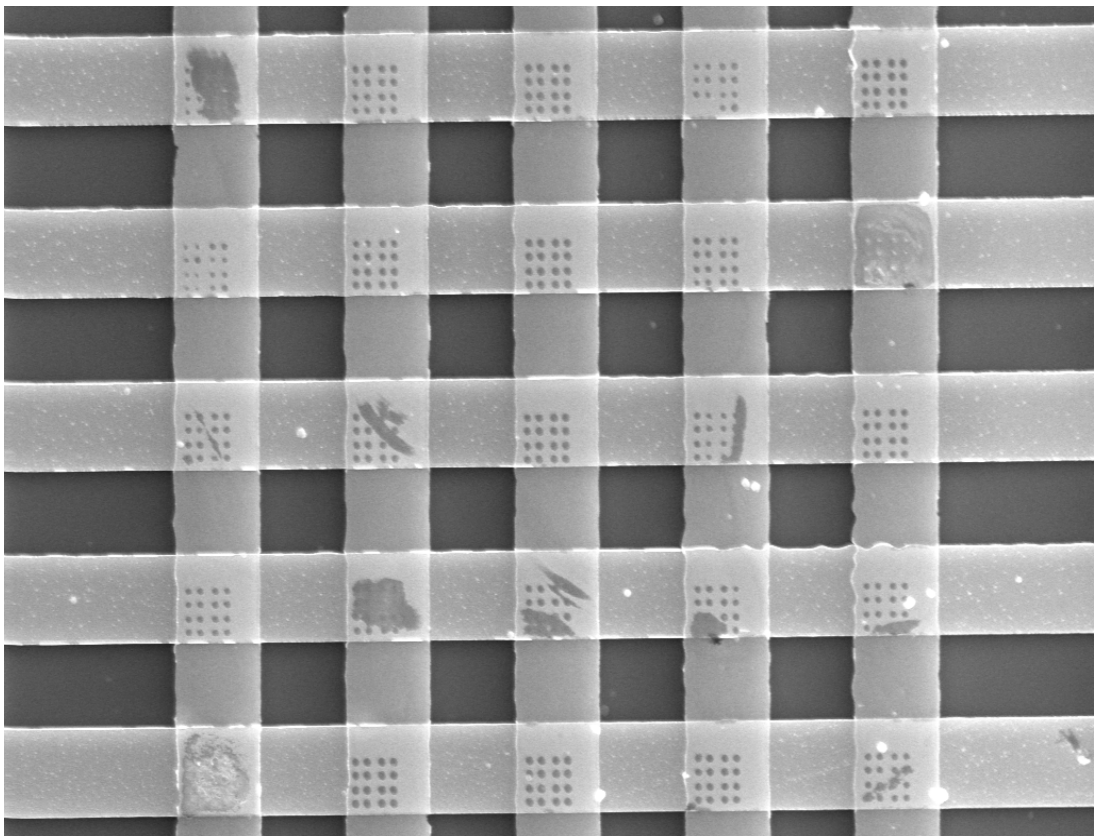

Figure 26. Closeup SEM of 700nm-diameter meshes ("micro meshes").

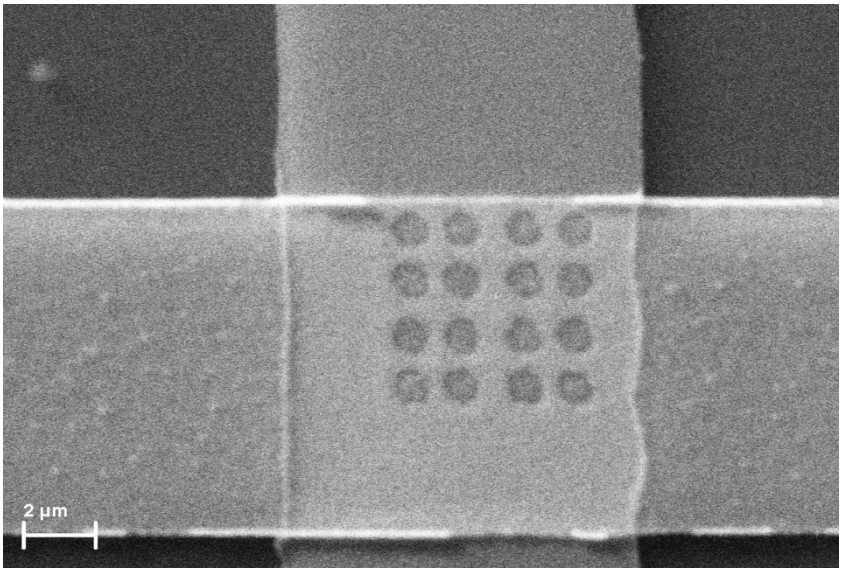

Figure 27. One of the micro meshes.

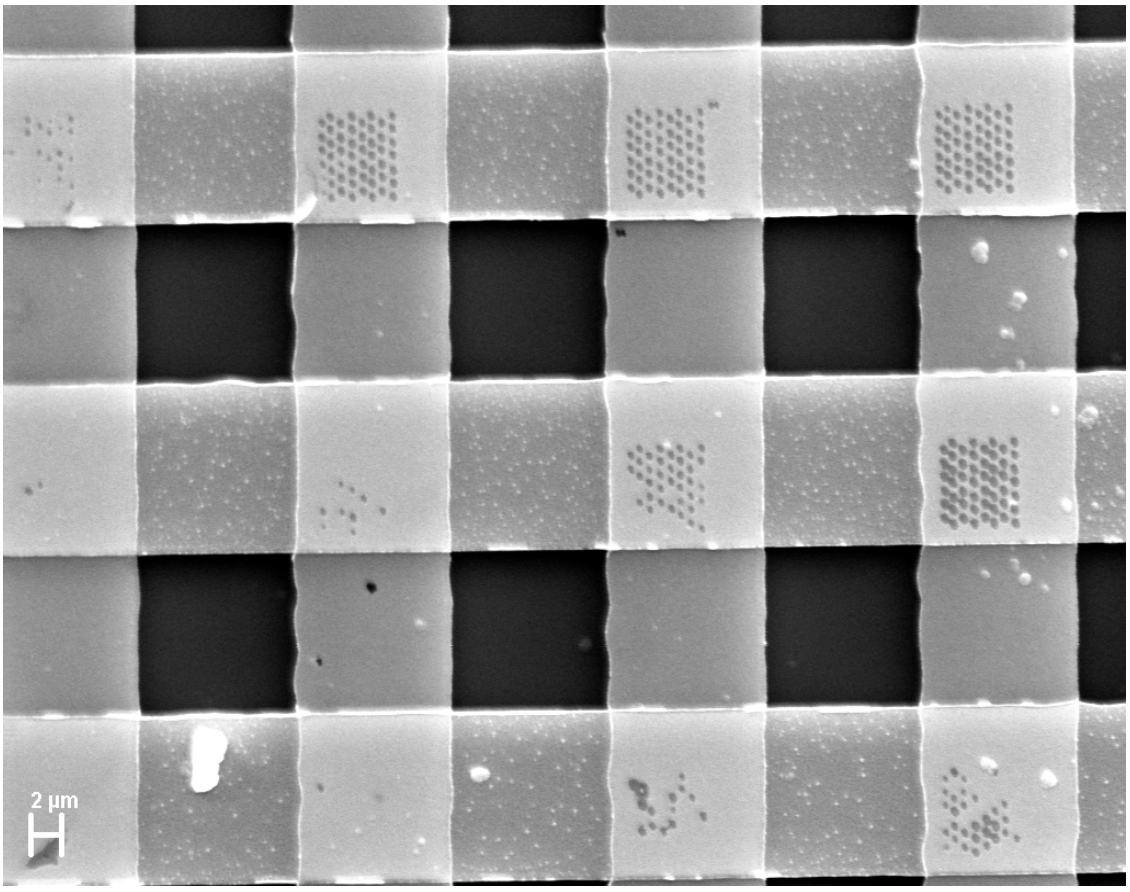

Figure 28. Closeup of 300-nm holes ("nano meshes").

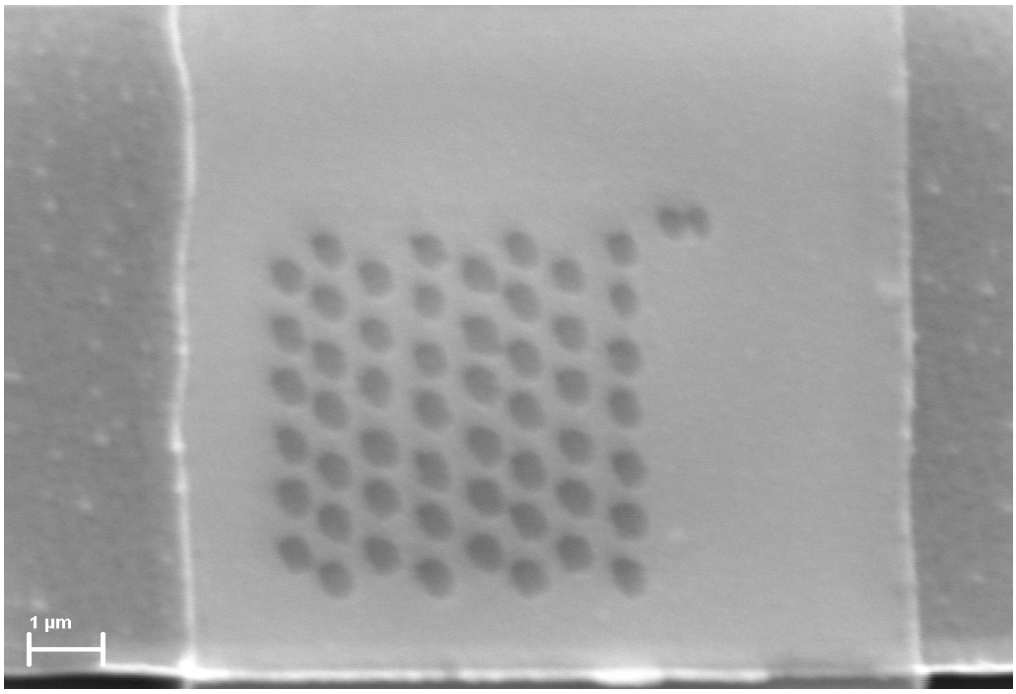

Figure 29. One of the nano meshes.

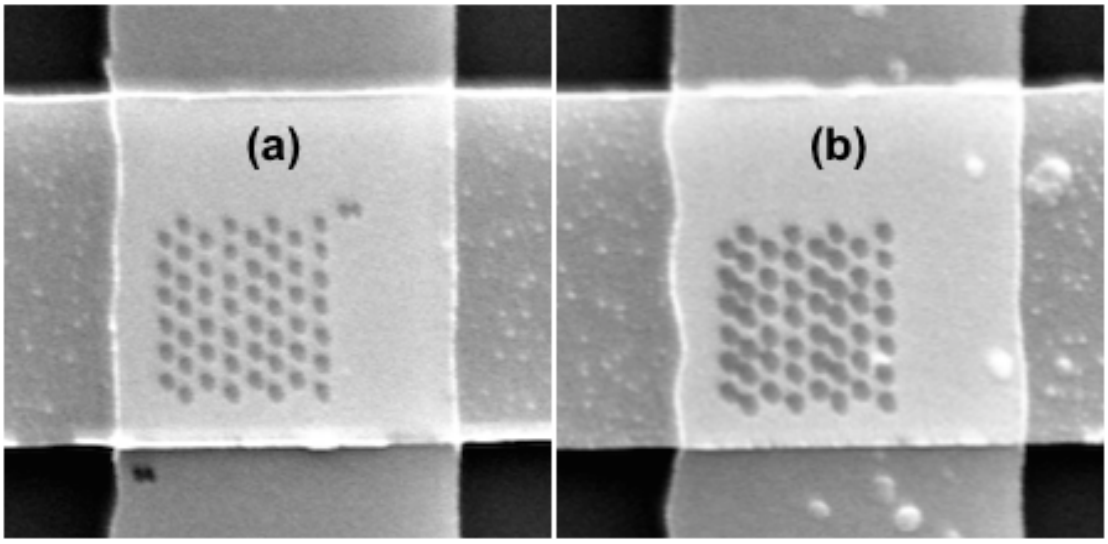

Figure 30. Comparison of (a) usuable nano mesh and over-etched nano mesh.

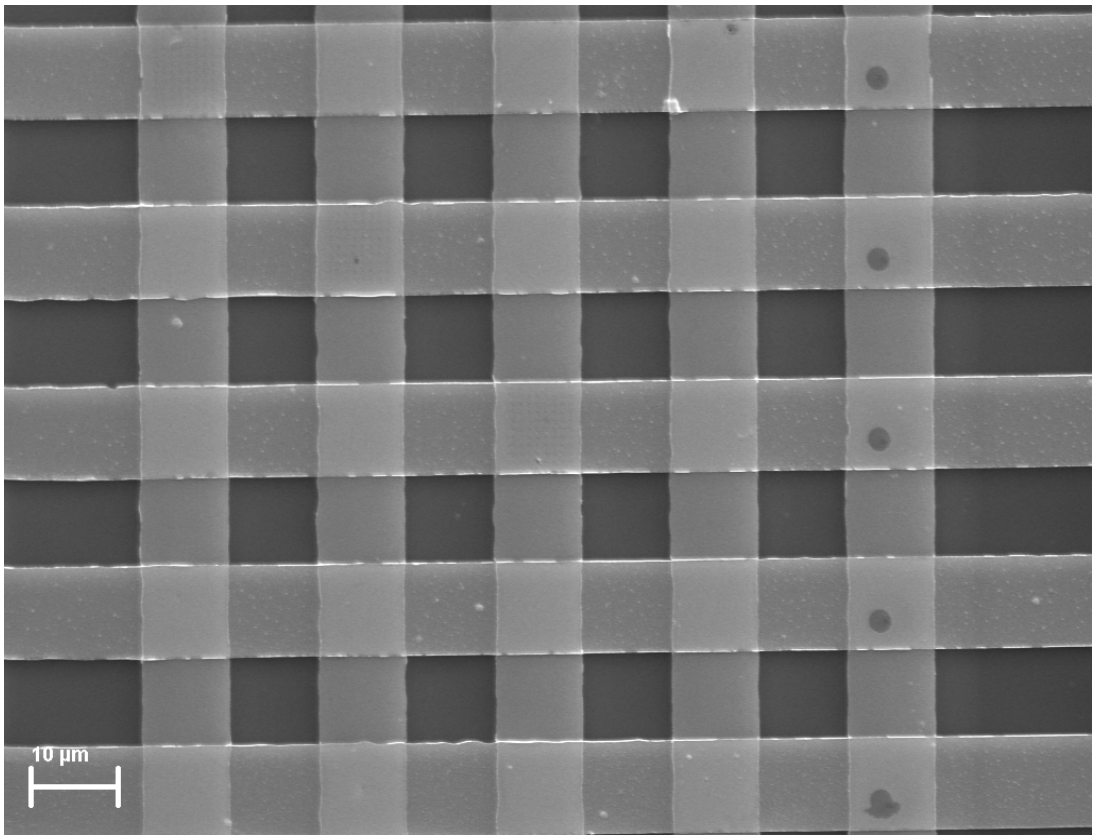

Figure 31. Closeup of final quadrant. The holes on the right were not used for testing but for etching guidance. The remaining non-etched devices were used as a control group (“non meshes”).

3.3.5 Preventing Contact Oxidation

In our previous fabrication trials, only a copper layer was deposited for the bottom electrode and contact pads. However, with continued exposure to heat during fabrication and testing, the copper contact pads would oxidize thus rendering the device unusable. Because W does not oxidize as easily, it was deposited prior to the copper electrodes to create repeatedly usable contacts, as illustrated in Fig. 33. This sub-section is reproduced from publications [2] and [3].

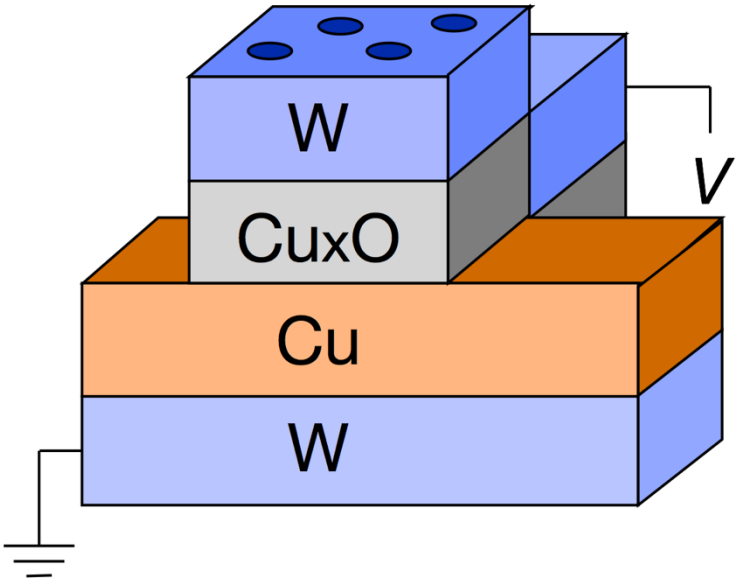

Figure 32. Schematic of memristor with etched tungsten layer.

3.4 SUMMARY

This chapter details the memristor design and fabrication for the three studies in this dissertation. A prototype memristor was designed and constructed early on in the research to determine feasibility of the sensing application for the first study. This prototype device consisted of a nonstoichiometric copper oxide sandwiched between two metal contacts. The second memristor was designed and fabricated later in the project with holes in the top metal contact. This design was used for the remaining two studies in this dissertation to expose more of the copper oxide switching layer and further investigate the sensing mechanism.

APPENDICES

APPENDIX A: SPUTTERING PARAMETERS

Sputtering Parameters for Section 4 Memristors:

W/Cu_xO (11 nm)/Cu device:

- Cu - Ar: ~1ccm, gas pressure: 3.47e-03 Torr, power: 50W, time: 60 sec
- Cu_xO - Ar: ~27ccm, O2: ~6ccm, gas pressure: 1.4e-01 Torr power: 200W, time: 11 sec
- W - Ar: ~1ccm, gas pressure: 9e-03 Torr, power: 60W, time: 3.5 min

W/Cu_xO (23 nm)/Cu device:

- Cu - Ar: ~1ccm, gas pressure: 4.89e-03 Torr, power: 50W, time: 111 sec
- Cu_xO - Ar: ~27ccm, O2: ~5ccm, gas pressure: 1.4e-01 Torr power: 200W, time: 22 sec
- W - Ar: ~1ccm, gas pressure: 9e-03 Torr, power: 60W, time: 3 min

W/Cu_xO (35 nm)/Cu device:

- Cu - Ar: ~1ccm, gas pressure: 4.89e-03 Torr, power: 50W, time: 111 sec
- Cu_xO - Ar: ~27ccm, O2: ~7ccm, gas pressure: 1.52e-01 Torr power: 200W, time: 35 sec
- W - Ar: ~1ccm, gas pressure: 9e-03 Torr, power: 60W, time: 3 min

Sputtering Parameters for Section 5 Memristors:

The Ar:O_2 ratio was adjusted to increase oxygen vacancies.

- W - Ar: ~1ccm; gas pressure: 7.6e-3; power: 65 W; time: 3 min
- Cu - Ar: ~1ccm; gas pressure: 7.7e-3; power: 85 W; time: 3 min
- Cu_xO - Ar: ~48ccm, O_2: 8ccm, gas pressure: 2.6e-1 Torr, power: 200 W, time: 3 min
- W - Ar: ~1ccm; gas pressure: 7.6e-3; power: 65 W; time: 3 min

APPENDIX B: RECIPES

Recipe for Photolithography of Memristors:

- Apply Shipley S1318 photoresist
- Spin at 3500 RPM for 1 minute
- Bake at 115 deg Celsius for 1 minute
- Undergo photolithography (MJB 3 Mask Aligner for 10 seconds)
- Develop with Shipley Microposit MF 319 for 30 seconds
- Rinse in deionized water for 1 minute

Recipe for Electron Beam Lithography of Memristors (Section 5):

- Apply PMMA C2 (electron beam lithography)
- Spin at 1500 RPM for 40 seconds
- Bake at 180 deg Celsius for 180 seconds
- Undergo electron beam lithography (JEOL 840A Scanning Electron Microscope and Electron Beam Lithography)
- Develop with 2:3 ration MIBK (methyl isobutyl ketone):IPA (isopropyl alcohol) solution for 10 secs
- Rinse in deionized water for 1 minute

Resist removal (both photoresist and electro beam resist)

- Rinse substrate in acetone for 1 minute
- Rinse in isopropanol or methanol for 1 minute
- Rinse in deionized water for 1-2 minutes

REFERENCES

REFERENCES

1. C. Nyenke and L. Dong, “Sensing ambient oxygen using a W/CuxO/Cu memristor,” *IEEE 10th International Conference on Nano/Micro Engineered and Molecular Systems*, pp. 254-258, Apr. 2015. © 2015 IEEE.

2. C. Nyenke and L. Dong, “Fabrication of a W/CuxO/Cu memristor with sub-micron holes for passive sensing of oxygen,” *Microelectronic Engineering*, vol. 164, pp. 48-52, Oct. 2016.

3. C. Nyenke and L. Dong, “Effect of NO2 and NH3 on the resistive switching behavior of W/CuxO/Cu memristors,” *Journal of Micromechanics and Microengineering*, vol. 27, no. 10, art. no. 105013, Oct. 2017. 10.1088/1361-6439/aa8672. © IOP Publishing. Reproduced with permission. All rights reserved.

CHAPTER 4 DETECTION OF AMBIENT OXYGEN USING W/Cu_xO/Cu MEMRISTORS OF DIFFERENT THICKNESSES

4.1 INTRODUCTION

Three sets of memristors with different switching layer thicknesses – 11nm, 23nm, and 35nm – were fabricated using the methodology detailed in Section 3.2. Each set was exposed to ambient oxygen for a period of time (days) to investigate passive sensing. Electrical characteristics and detection of ambient oxygen were investigated for both devices before and after the prolonged exposure to ambient oxygen. A significant portion of this work references publication [1].

4.2 EXPERIMENTAL SETUP

The current-voltage (I-V) characteristics of the device were measured with a Keithley 6487 Picoammeter. For the measurement setup, the copper bottom electrode was grounded while a voltage was applied to the tungsten top electrode. The electrode contacts were connected to the picoammeter via metal probes, as shown in Fig. 34. Electrical measurements – voltage and current – were taken before and after extended exposure to ambient oxygen. This data was sent from the picoammeter to a local computer via an accompanying GPIB cable and stored in Excel.

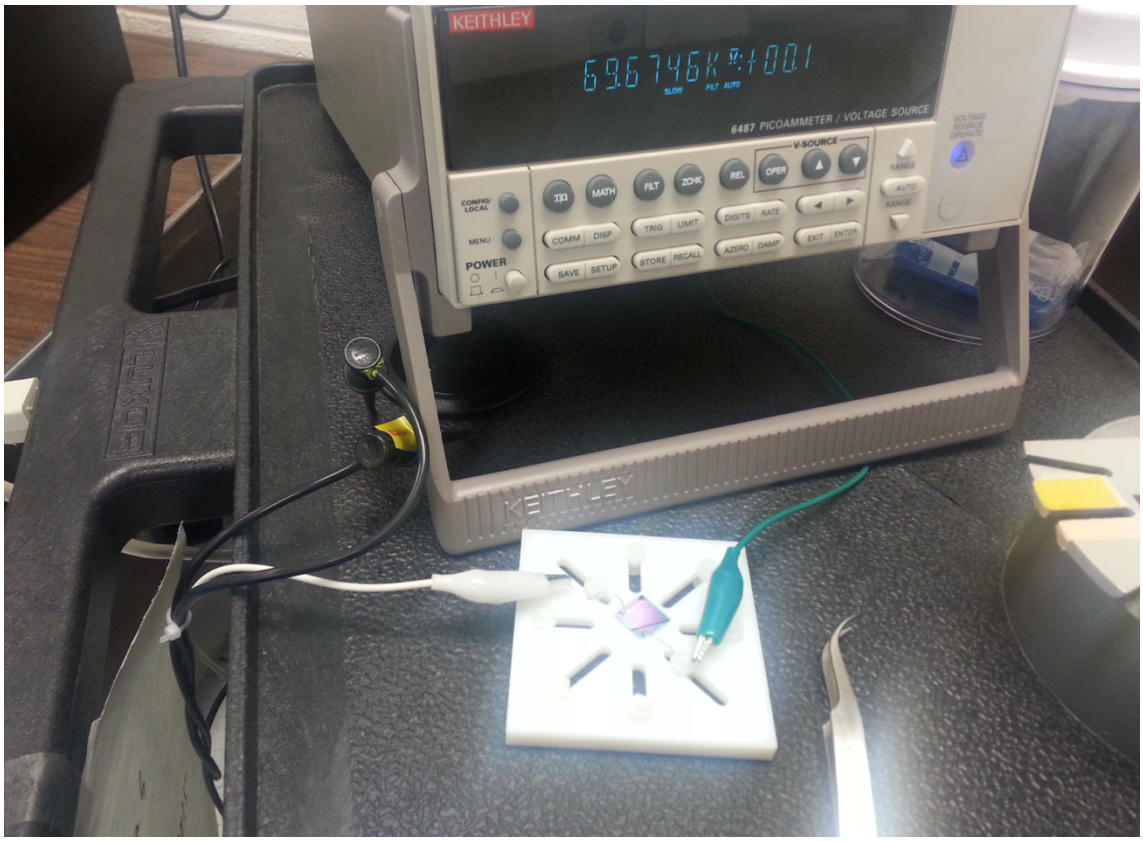

Figure 33. Measurement setup.

Atomic composition of each device layer was determined by energy-dispersive X-ray spectroscopy (EDS) inside a Carl Zeiss Variable Pressure scanning electron microscope (SEM) EVO LS25. EDS analyses were performed twice – once before the experiment and again after extended exposure to ambient air. The thickness of each layer in the memristor was measured using a Veeco Dektak3 surface profiler with a 0.5-nanometer vertical resolution before the experiment.

4.3 DISCUSSION OF RESISTIVE SWITCHING BEHAVIOR

4.3.1 Formation of Conductive Filaments

It has been shown that formation of conductive filaments from oxygen vacancies within the switching layer converts the metal oxide layer to a resistive switching layer for the device to be functional as memristor [2]. Once formed, application of a sufficient bias voltage can rupture and re-heal these conductive filaments by repelling and attracting oxygen vacancies, respectively. This leads to switching between a low resistance state and high resistance state, resulting in the hysteretic nature of memristors.

In the case of the two devices that were fabricated for this study, the forming process required voltages of -2.1 Volts, -3.8 Volts, and -4 Volts, respectively. The dependence of the forming voltage and switching layer thickness makes sense given the correlation between the anodizing voltage and forming voltage [3], (The anodizing voltage, V_a, is what is required to oxidize a metal layer.) Because voltage is proportional to distance, an increase in layer thickness will translate to an increase in V_a. The correlation between Va and the forming voltage V_f means that a thicker metal oxide layer will require a higher V_f. Thus, we observe a higher forming voltage for the W/Cu_xO (35 nm)/Cu device versus the W/Cu_xO (11 nm)/Cu W/Cu_xO (23 nm)/Cu devices. A similar relationship between the breakdown voltage and V_f can be used to explain this thickness-dependent voltage as well [4].

4.3.2 Characterizing Memristive Behavior

Figs. 35 and 38 display the current-voltage (IV) characteristics for each memristor set after two voltage sweeps. For the W/Cu_xO (11 nm)/Cu device in Fig. 35, we observe bipolar resistive switching between ±2.5 V. The low resistance state (LRS) and high resistance state (HRS) are 10.7 k-ohms and 12.4-35.0 k-ohms, respectively. In contrast, the W/Cu_xO (35 nm)/Cu device in Fig. 36 has a larger LRS and HRS due to the thicker switching layer. Additionally, we observe inherent complementary resistive switching (CRS) for the W/Cu_xO (35 nm)/Cu device unlike for the thinner device. From ± 1 V, the device is in HRS at ~ 400 k-ohms before switching to an LRS of ~ 70k-ohms at ± 1 V. The W/Cu_xO (35 nm)/Cu

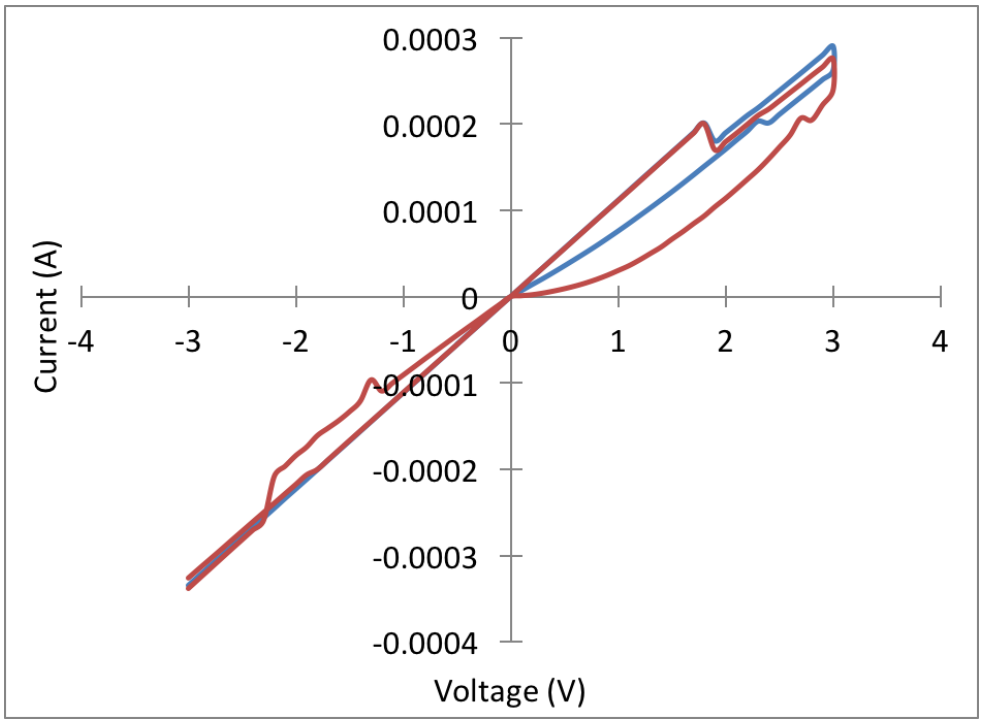

Figure 34. Current-voltage characteristics of the W/Cu_xO(11nm)/Cu memristor.

device maintains this LRS until it switches again to a higher and nonlinear resistance at ± 4 V. When the voltage approaches ± 1 V, the device becomes linear again with a maximum HRS of ~400 k-ohms. The memristance of this device between ±1 V is better observed in Figure 37.

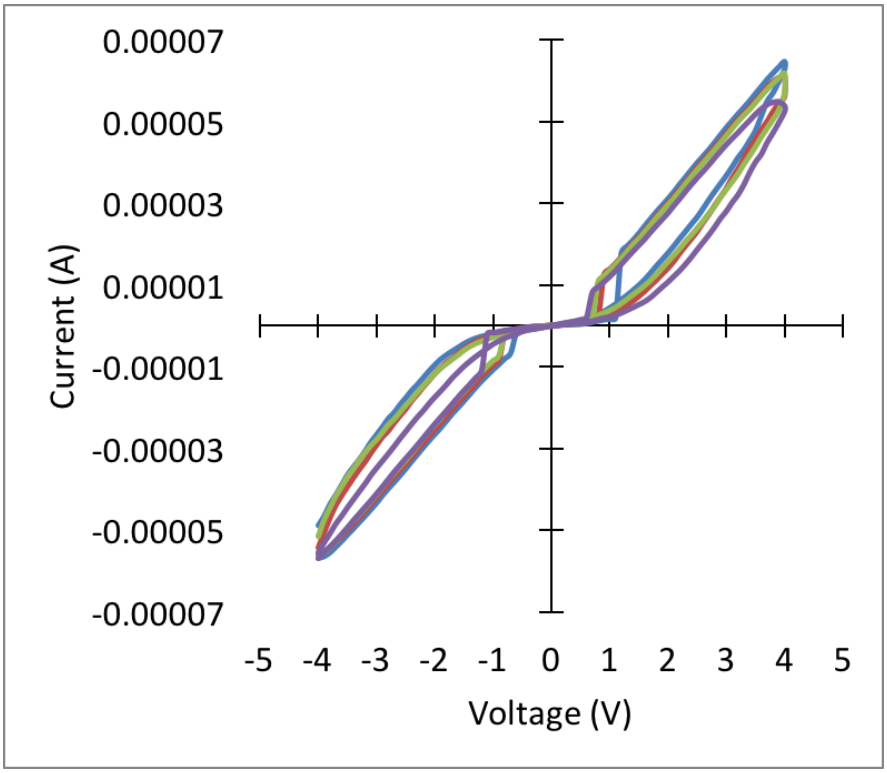

Figure 35. Current-voltage characteristics of the W/Cu_xO(35nm)/Cu memristor.

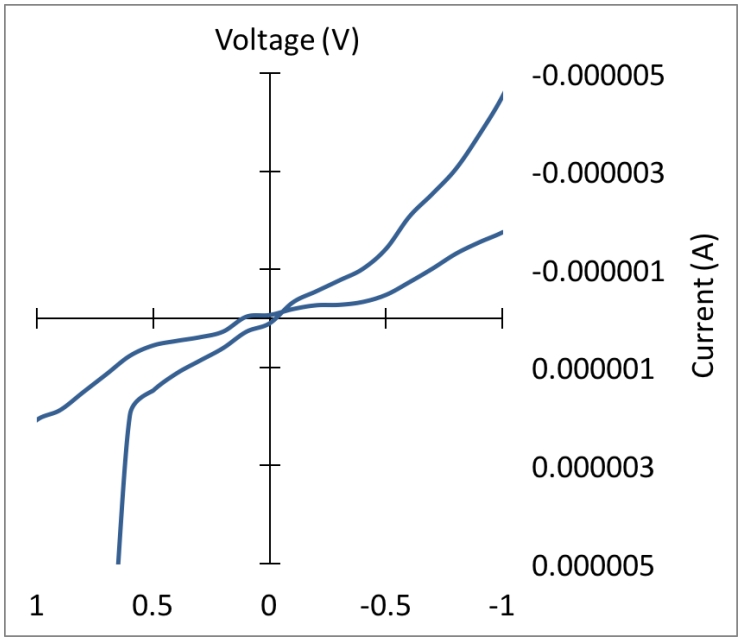

Figure 36. Close-up of the W/Cu_xO(35nm)/Cu memristor current-voltage characteristics between -1 and 1 V.

4.3.3 Identifying the Conduction Mechanism

In order to identify the conduction mechanisms for the W/Cu_xO (35 nm)/Cu device, Fig. 38 displays a double logarithmic plot for the positive bias region of Fig. 37. Here we see four segments with slopes ending and/or beginning at 1 V and 4 V. (The sweep direction is indicated by the letters a.-d.) This double logarithmic plot is then split into four distinct graphs in Fig. 39 so as to better capture the slope information. In Fig. 39(a), the log-log graph is linear with a slope of ~1, which indicates Ohmic conduction *(I α V)* for voltages < 1 V. For voltages of 1 V through 4 V, the graph in Fig. 39(b) is also in agreement with Ohmic conduction. Thus, the transition from HRS in the low-voltage region to LRS in the high-voltage region

corresponds with the transition from one form of Ohmic conduction to another. At 4 V, however, the device transitions from Ohmic conduction to space-charge-limited conduction (SCLC) as indicated by the slope of ~2 in Fig. 39(c). This slope is in agreement with $I \alpha V^2$, which describes the square law dependence of SCL current due to the dominance of hole injection [5,6]. This conduction also corresponds with the nonlinear portion of the HRS in Fig. 18, from 4 V to 1 V. The device then returns to Ohmic conduction at 1 V with a slope of ~1 in Fig. 39(d). This conduction mechanism correlates with the switch to linear HRS in the low-voltage region.

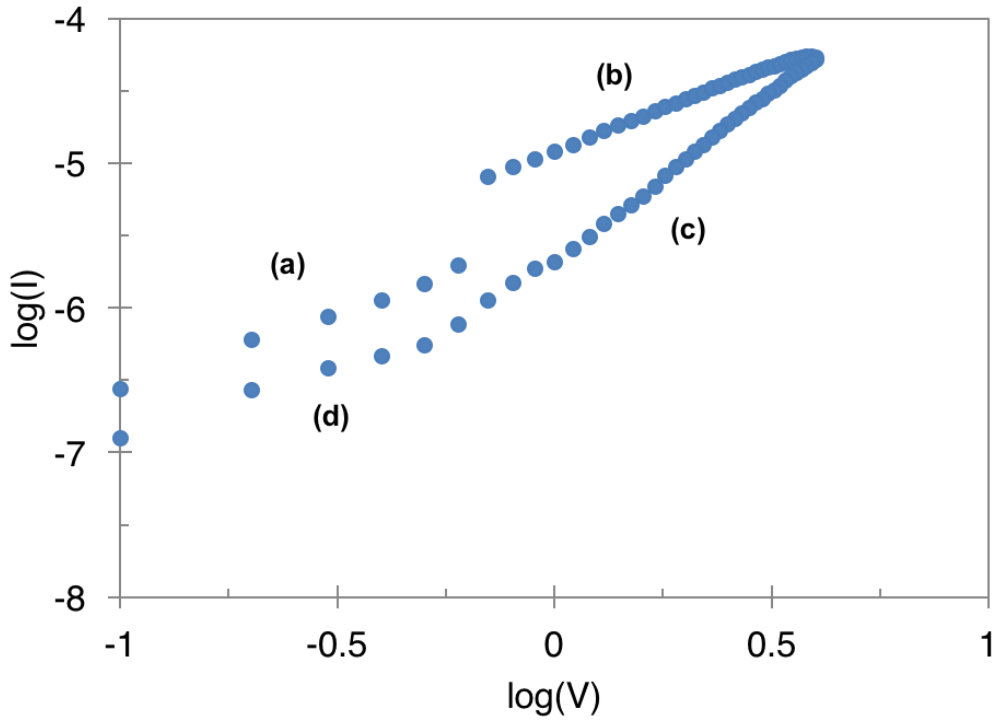

Figure 37. Log (I) vs. log (V) plot of memristor in the positive bias region.

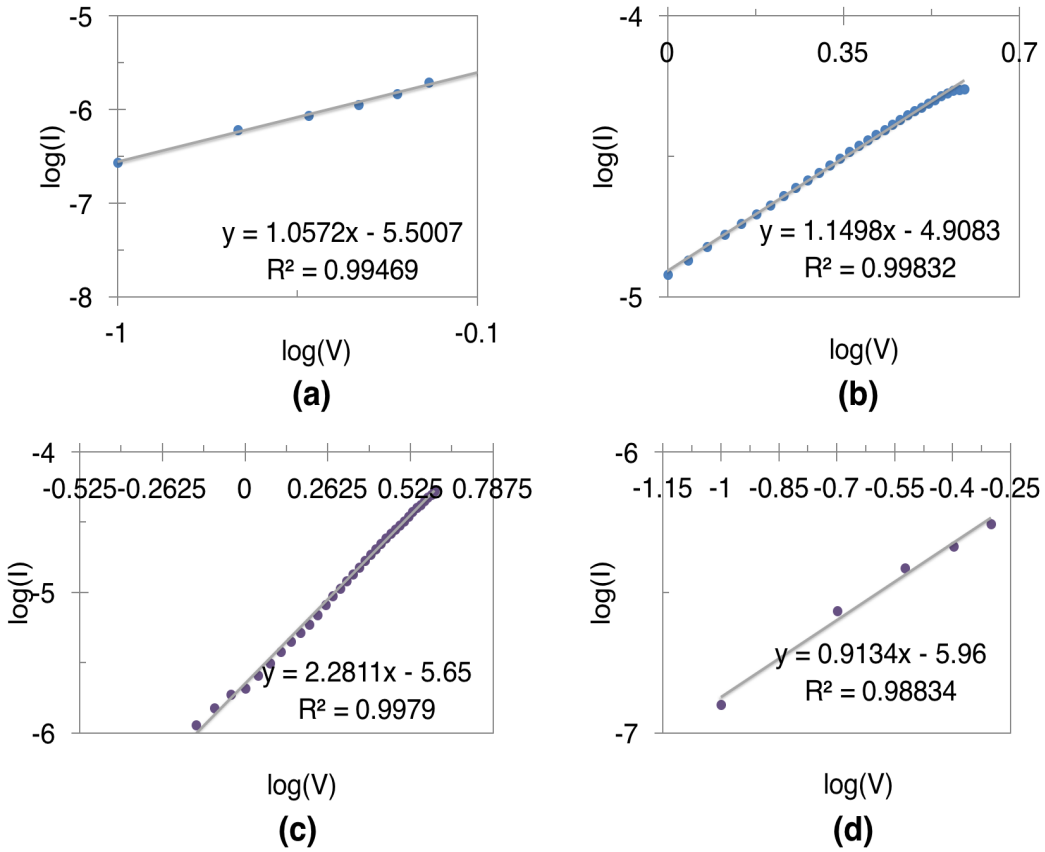

Figure 38. Best fit lines on log-log plots of memristor in the positive bias region.

4.4 DISCUSSION OF PASSIVE SENSING RESULTS

4.4.1 Increased Oxygen Composition with Time

Tables 1 and 2 show EDS results for W/Cu_xO (35 nm)/Cu memristor five and eight weeks after exposure to ambient oxygen, respectively. (Because the SEM penetration depth is greater than 0.5 microns, the oxygen content includes that of the SiO_2/Si substrate.) Comparison of both tables reveals a 0.44 % increase

of oxygen in those three weeks. Comparison of Tables 4 and 5 for a second memristor, W/Cu_xO (23 nm)/Cu, reveals a 0.55 % increase. This observation is consistent with adsorption of oxygen to copper atoms on the exposed copper oxide surface in those few weeks. Additionally, there were no new elements detected (such as nitrogen) by EDS after analysis. (NOTE: Only W/CuxO (35 nm)/Cu and W/CuxO (23 nm)/Cu were analyzed with EDS.)

Table 1. EDS Quantitative Results for Cu_xO (35 nm).

Elemen	Weight	Atomic	Net Int.	Net Int.
O	72.52	91.29	279.32	0.02
Cu	27.48	8.71	39.24	0.11

Table 2. EDS Quantitative Results after 22 Days.

Elemen	Weight	Atomic	Net Int.	Net Int.
O	73.63	91.73	183.03	0.02
Cu	26.37	8.27	23.97	0.13

Table 3. EDS Quantitative Results for Cu_xO (23 nm).

Elemen	Weight	Atomic	Net Int.	Net Int.
O	73.24	91.57	329.57	0.01
Cu	26.76	8.43	44.25	0.11

Table 4. EDS Quantitative Results after 22 Days.

Elemen	Weight	Atomic	Net Int.	Net Int.
O	74.63	92.12	159.04	0.02
Cu	25.37	7.88	19.51	0.15

4.4.2 Progression of Resistance with Time under Exposure

Resistances were computed from current and voltage data that were collected before and after exposure to ambient oxygen. Fig. 40 shows plots of the resistance versus voltage, as opposed to current versus voltage, to better illustrate the qualitative effects on resistance states. (These plots are of the W/Cu_xO (11 nm)/Cu device.) Exposure to oxygen over the course of 48 days has changed the shape of the original plot, yielding an average increase in resistance states. Fig. 41 is a plot of the low resistance state only and between +-2.1 V, which is the setting voltage for this particular memristor. Similarly, exposure to oxygen over the

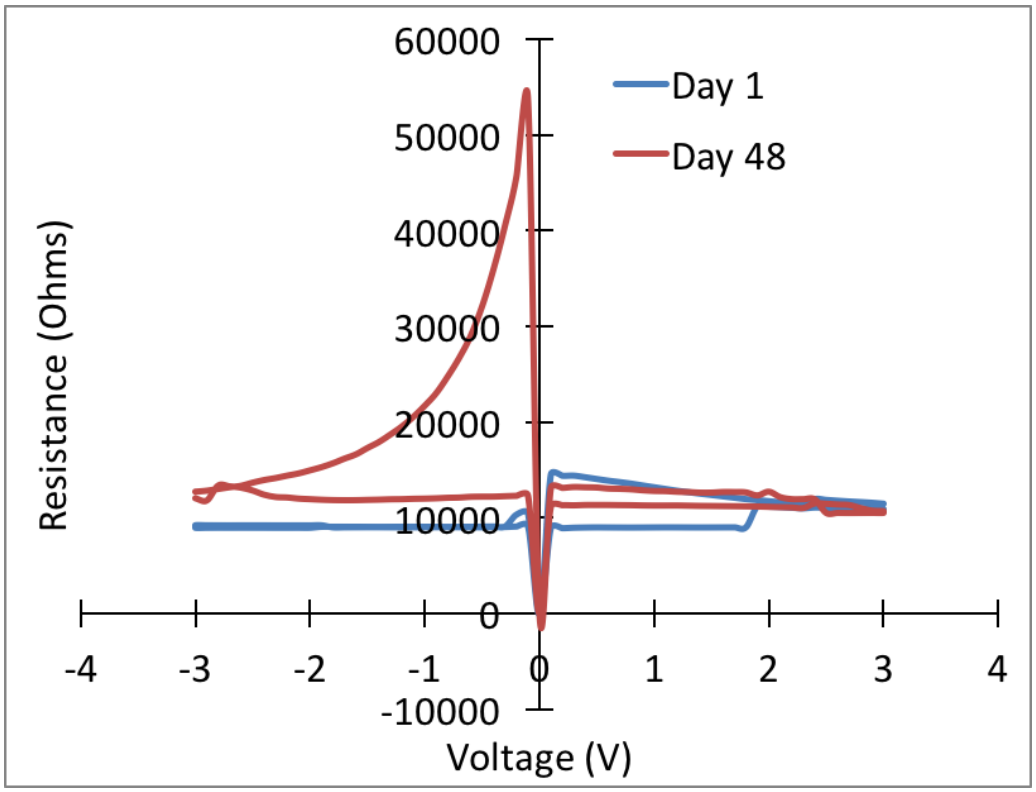

Figure 39. Plot of resistance versus applied voltage before and after exposure to ambient oxygen.

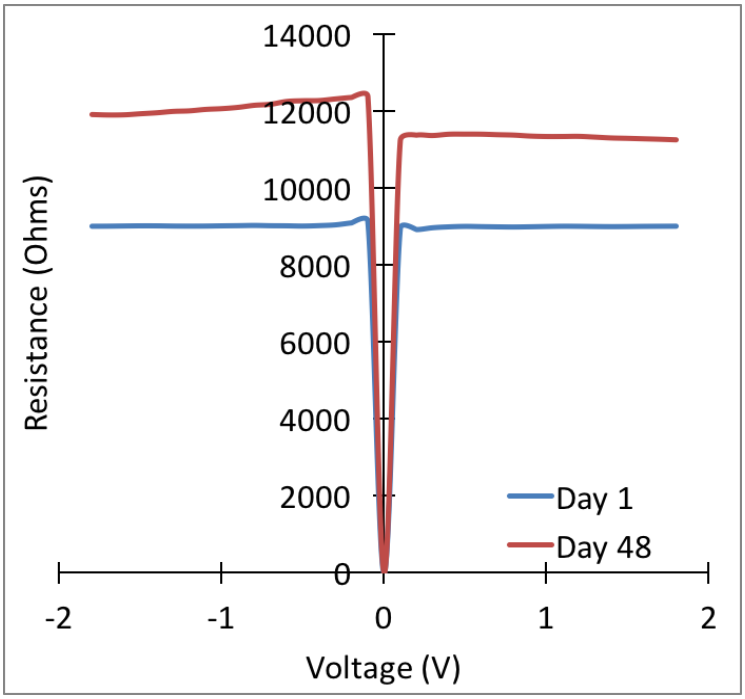

Figure 40. Closeup of low resistance state (LRS).

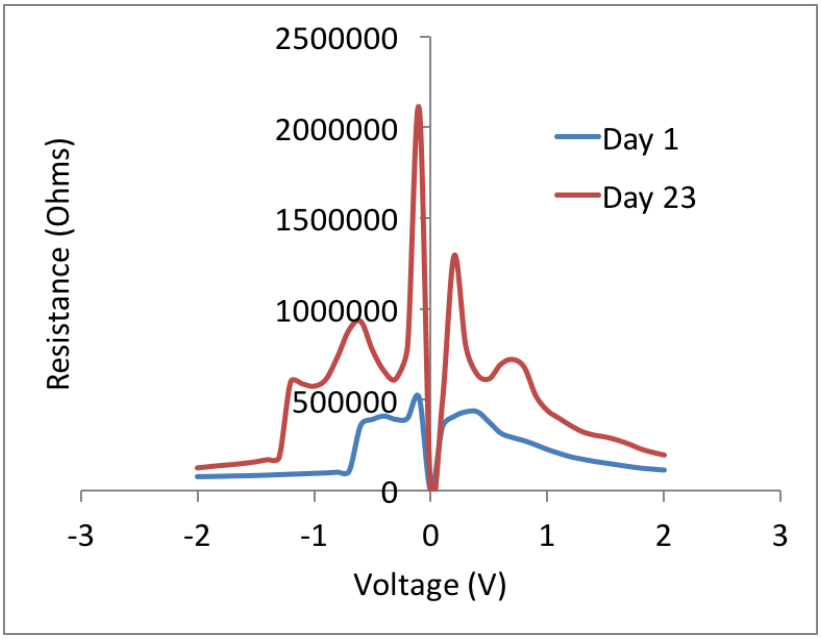

Figure 41. Comparison of LRS states of W/CuxO(35nm)/Cu device.

course of 23 days correlates with an increase in low resistance states for the W/Cu_xO (35 nm)/Cu device in Figure 42.

The results of exposure to ambient oxygen as a function of time are shown numerically in Tables 5 and 6 for the two memristors. The low resistance states increased by 6.8 %, 2.1 %, and 0.6 % for the 11-nm, 23-nm, and 35-nm memristors, respectively, after three days. The devices were measured again after three to six weeks and revealed an increase of 31.3 %, 24.2 %, and 28.2 %, respectively, from their original values. These increases in resistance states are believed to be the result of ionically adsorbed oxygen in ambient air to the copper oxide surface, which is then followed by the filling of oxygen vacancies in the layer [14-15]. These results also indicate that the adsorption of oxygen was not immediate but rather progressed over time.

Table 5. Progression of low resistance states with time

Cu_xO thickness	**Forming voltage**	**Resistance**		
		Day 1	**Day 3**	**Day 23-48**
11 nm	+/-2.1 V	8990 Ω	9600 Ω	11800 Ω (day 48)
23 nm	+/- 3.8 V	48300 Ω	49300 Ω	60000 Ω (day 23)
35 nm	+/- 4 V	69900 Ω	70300 Ω	89600 Ω (day 23)

Table 6. Percentage change in low resistance states with time

Cu_xO thickness	**Forming voltage**	**Resistance**		
		3 days	**23 days**	**48 days**
11 nm	+/-2.1 V	6.8 %	--	31.3 %
23 nm	+/- 3.8 V	2.1 %	24.2 %	--
35 nm	+/- 4 V	0.6 %	28.2 %	--

4.5 SUMMARY

In summary, memristors were designed, fabricated, and tested for passive sensing of ambient oxygen at room temperature. Comparisons of resistance states before and after exposure to ambient oxygen demonstrate increases with time (i.e., days). EDS profiles are consistent with the adsorption of oxygen to the copper oxide switching layers with time. Early results also indicate an initial dependence of sensitivity on thickness of the copper-oxide switching layer, but more experiments are required to further investigate this observation. Future work will also research the oxygen concentration of the switching layer with resistance changes more quantitatively as well as the effect of temperature on sensing. In conclusion, we have demonstrated a step towards the use of a memristor as a passive sensor by taking advantage of the device's ability to memorize (or record) historical information.

REFERENCES

REFERENCES

1. C. Nyenke and L. Dong, “Sensing ambient oxygen using a W/CuxO/Cu memristor,” *IEEE 10th International Conference on Nano/Micro Engineered and Molecular Systems*, pp. 254-258, Apr. 2015. © 2015 IEEE.

2. J. Tedesco, L. Stephey, M. Hernandez-Mora, C. Richter, and N. Gergel-Hackett, "Switching mechanisms in flexible solution-processed TiO_2 memristors," *Nanotechnology*, vol. 23, art. no. 305206, Aug. 2012.

3. F. A. Chudnovskii, L. L. Odynets, A. L. Pergament, and G. B. Stefanovich, “Electroforming and switching in oxides of transition metals: The role of metal-insulator transition in the switching mechanism,” *Journal of Solid State Chemistry*, vol. 122, pp. 95-99, 1996.

4. F. Verbakel, S. C. J. Meskers, R. A. J. Janssen, H. L. Gomes, M. Cölle, M. Büchel, and D. M. de Leeuw, “Reproducible resistive switching in nonvolatile organic memories,” *Applied Physics Letters*, vol. 91, art. no. 192103, Nov. 2007.

5. A. Rose, “Space-Charge-Limited Currents in Solids,” *Physical Review*, vol. 97, no. 6, pp. 1539-1544, Mar. 1955.

6. Y-J. Huang, S-C. Chao, D-H. Lien, C-Y. Wen, J-H. He, et al., “Dual functional memory and threshold resistive switching based on the push-pull mechanism of oxygen ions,” *Scientific Reports*, vol. 6, art. no. 23945, Apr. 2016.

7. R. Waser and M. Aono, “Nanoionics-based resistive switching memories,” *Nature Materials*, vol. 6, pp. 833-840, Nov 2007.

8. Y. Yang, S. Choi, and W. Lu, “Oxide heterostructure resistive memory,” *NanoLetters*, vol. 13, pp. 2908-2915, May 2013.

9. S. Kim, S. Choi, and W. Lu. “Comprehensive physical model of dynamic resistive switching in an oxide memristor,” *ACS Nano*, vol. 8, no. 3, pp. 2369-2376, Feb. 2014.

10. H. Z. Zhang, D. S. Ang, C. J. Gu, K. S. Yew, X. P. Wang, et al., “Role of interfacial layer on complementary resistive switching in the TiN/HfO_x/TiN resistive memory device,” *Applied Physics Letters*, vol. 105, art. no. 222106, Dec. 2014.

11. H. Z. Zhang, D. S. Ang, K. S. Yew, and X. P. Wang, “Enhanced stability of complementary resistance switching in the TiN/HfO_x/TiN resistive random-access memory device via interface engineering,” *Applied Physics Letters*, vol. 108, art. no. 083505, Feb. 2016.
12. Y. Yang, P. Sheridan, and W. Lu, “Complementary resistive switching in tantalum oxide-based resistive memory devices,” *Applied Physics Letters*, vol. 100, art. no. 203112, May 2012.

13. S. Brivio, J. Frascaroli, and S. Spiga, “Role of metal-oxide interfaces in the multiple resistance switching regimes of Pt/HfO_2/TiN devices,” *Applied Physics Letters*, vol. 107, art. no. 023504, Jul. 2015.

14. H. Freund, “Metal oxide surfaces: electronic structure and molecular adsorption,” *Basic Solid State Physics (Physica Status Solidi B)*, vol. 192, pp. 407-440, Dec. 1995.

15. A. Goswami, *Thin Film Fundamentals*, first ed. New Delhi: New Age International Pvt Ltd Publishers, 1996.

CHAPTER 5 INVESTIGATION OF W/Cu_xO/Cu MEMRISTORS WITH SUB-MICRON HOLES FOR PASSIVE SENSING OF OXYGEN

5.1 INTRODUCTION

This chapter, which references publication [1], discusses the influence of surface area on passive sensing of oxygen. Two sets of memristors were fabricated with sub-micron holes etched into the top W electrodes to reveal the oxide surface. One set consisted of fifty-two holes each 300 nm in diameter. The second set consisted of sixteen holes each 700 nm in diameter. Additionally, a larger crossbar array (10x10) was constructed to increase memristor yield per substrate. Each substrate was then exposed to ambient oxygen at 180 degrees Celsius to induce passive sensing in minutes.

5.2 EXPERIMENTAL SETUP

Electrical measurements of each testable device were acquired using a Keithley 6487 Picoammeter. The copper bottom electrode was grounded while a bias voltage was applied to the tungsten top electrode for this setup. In order to bring about passive oxygen sensing, the substrate was placed inside a thermal oven and subjected to 5-25 min of surrounding air at a working temperature of 180 °C. (The devices were not tested at other temperatures or oxygen pressures since this process was irreversible.) The electrical properties were collected at the

beginning and end of the experiment then analyzed for each of the devices. Atomic composition analyses were performed, as well, by energy-dispersive X-ray spectroscopy (EDS) inside a Carl Zeiss Variable Pressure scanning electron microscope (SEM) EVO LS25.

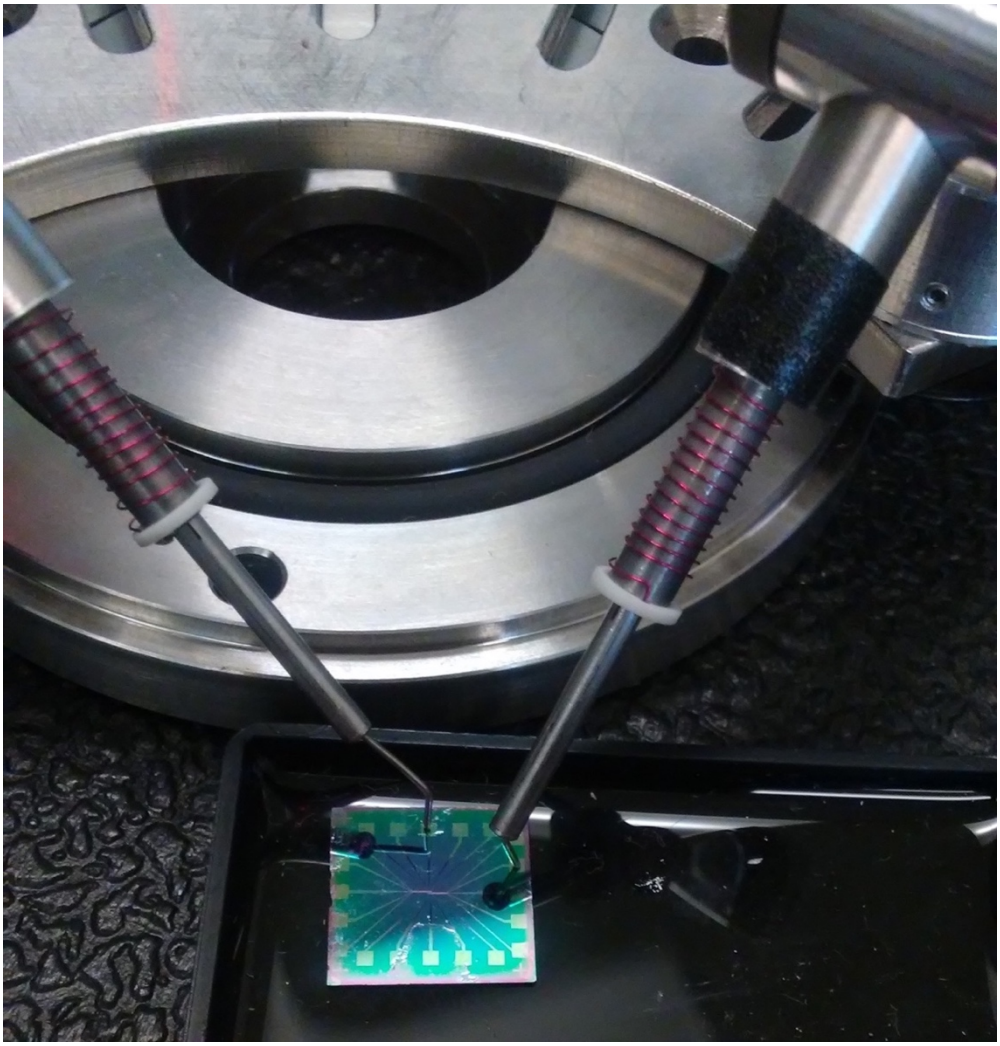

Figure 42. Measurement setup.

5.3 DISCUSSION OF RESULTS

5.3.1 Characterizing Memristive Behavior

Figs. 44-51 show current-voltage (IV) plots for each nano mesh (Figs. 44-46), micromesh (Figs. 47-49), and devices without meshes (Figs. 50-51) before sensing. All the devices exhibit visually similar thin hystereses, which is indicative of similar levels of memristance. After the substrate is subjected to 25 minutes of ambient air at the working temperature of 180 deg C, each set of devices behaves differently from the other as will now be discussed.

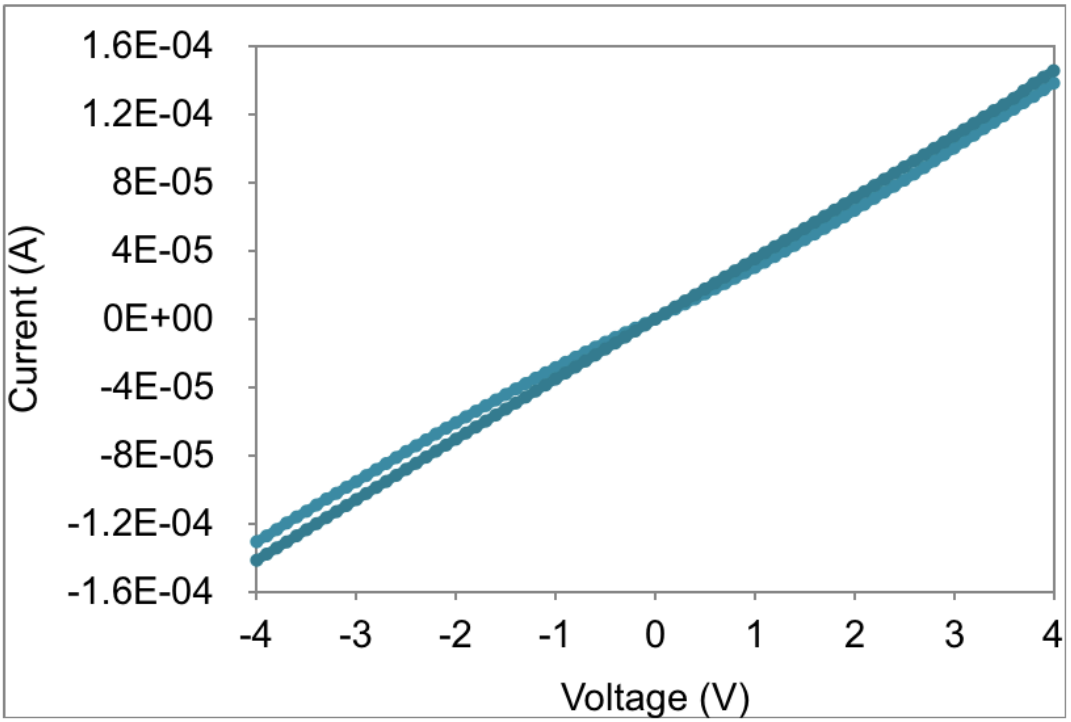

Figure 43. Current-voltage characteristics of nano-mesh before testing.

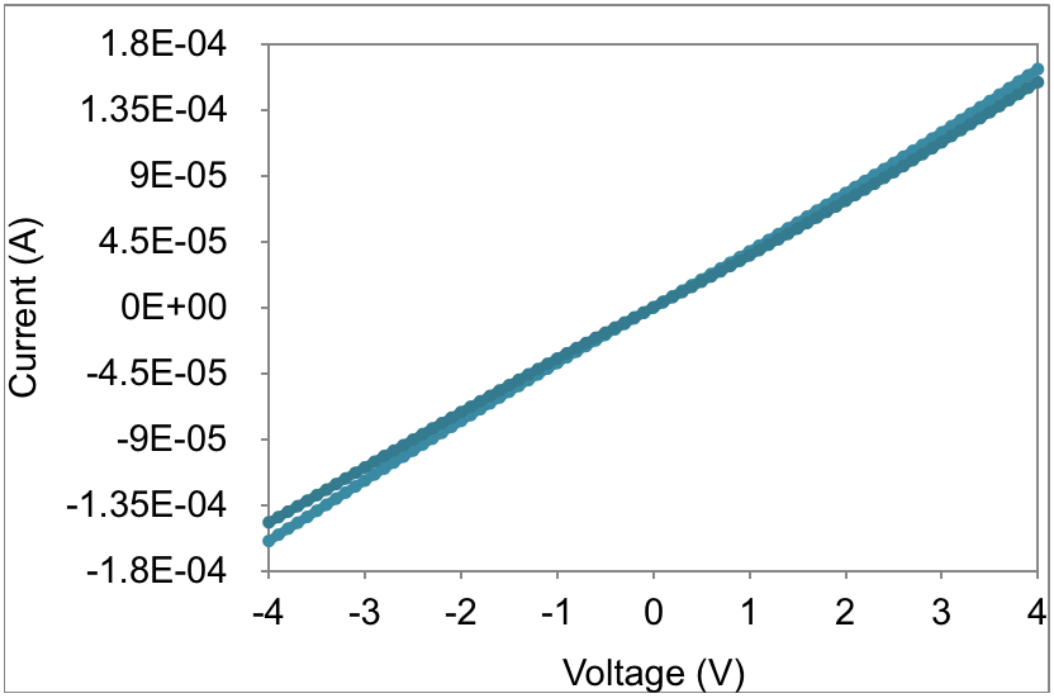

Figure 44. Current-voltage characteristics of nano-mesh before testing.

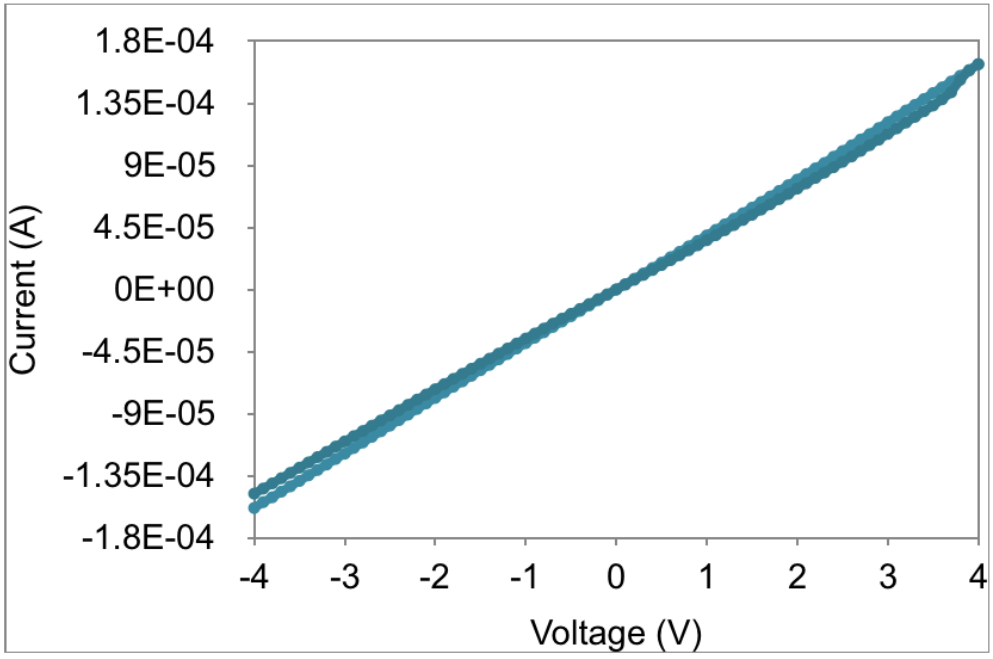

Figure 45. Current-voltage characteristics of nano-mesh before testing.

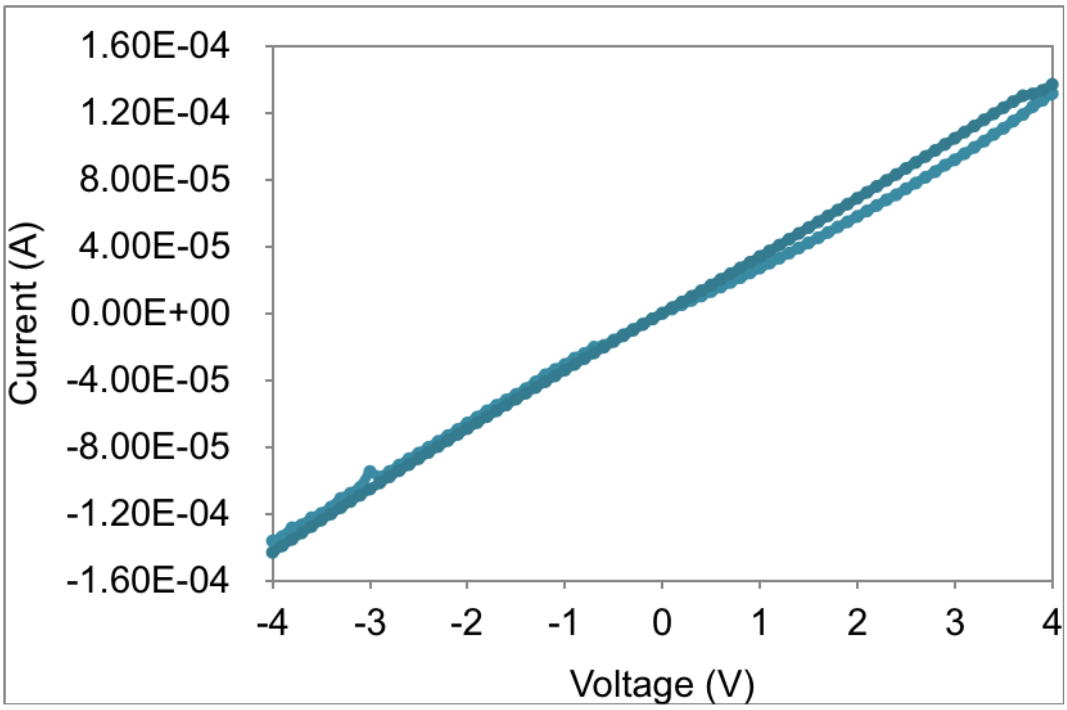

Figure 46. Current-voltage characteristics of micro-mesh before testing.

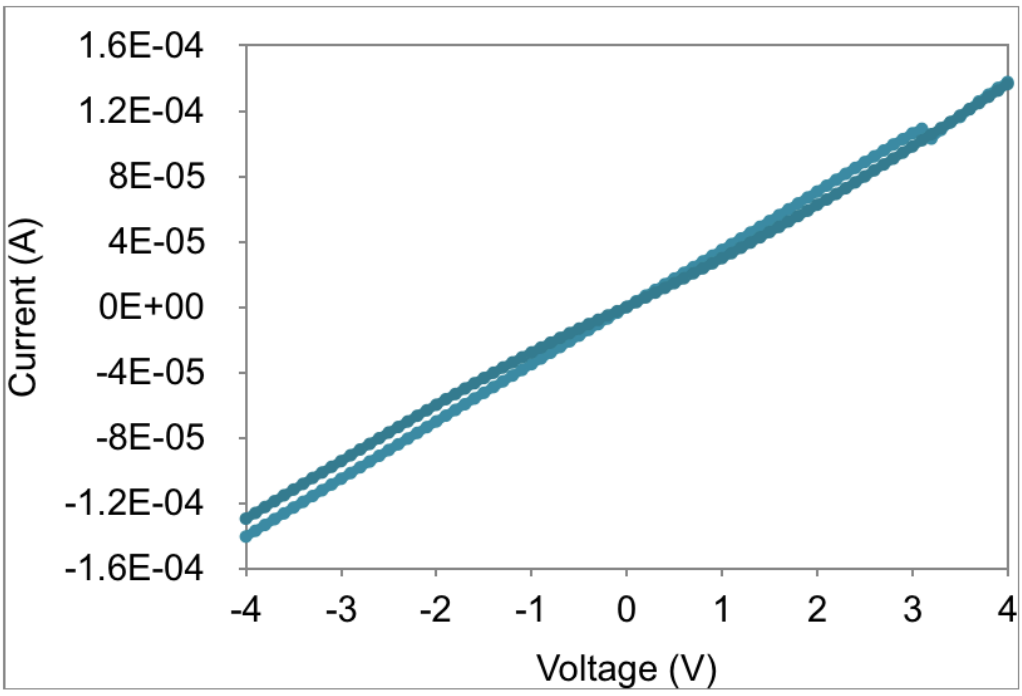

Figure 47. Current-voltage characteristics of micro-mesh before testing.

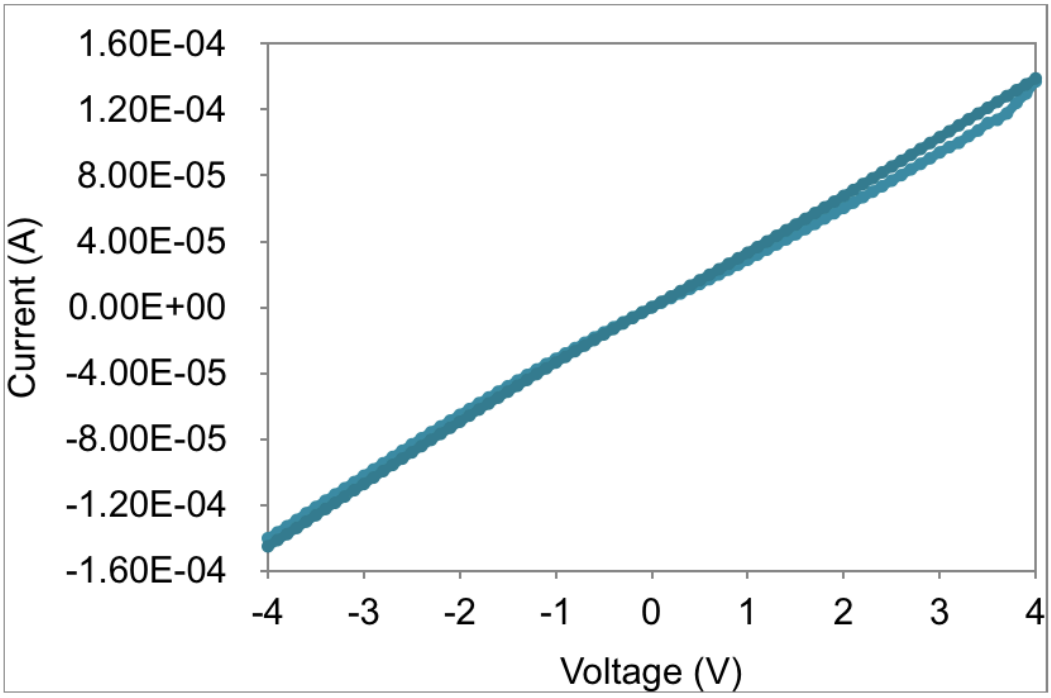

Figure 49. Current-voltage characteristics of micro-mesh before testing.

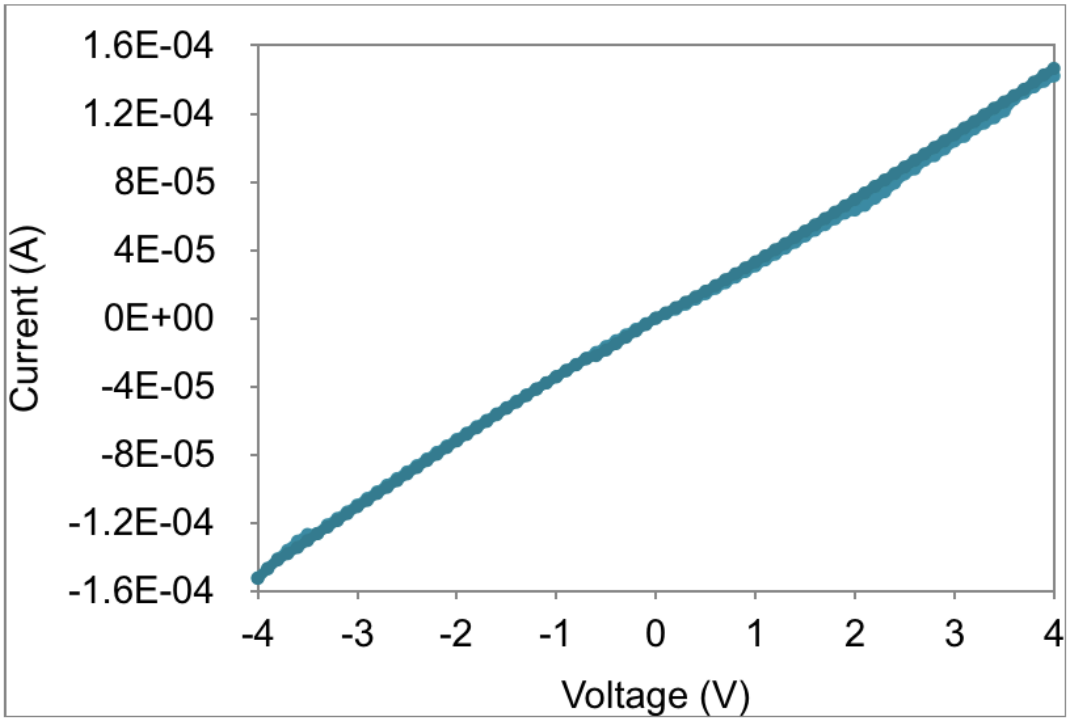

Figure 48. Current-voltage characteristics of non-mesh before testing.

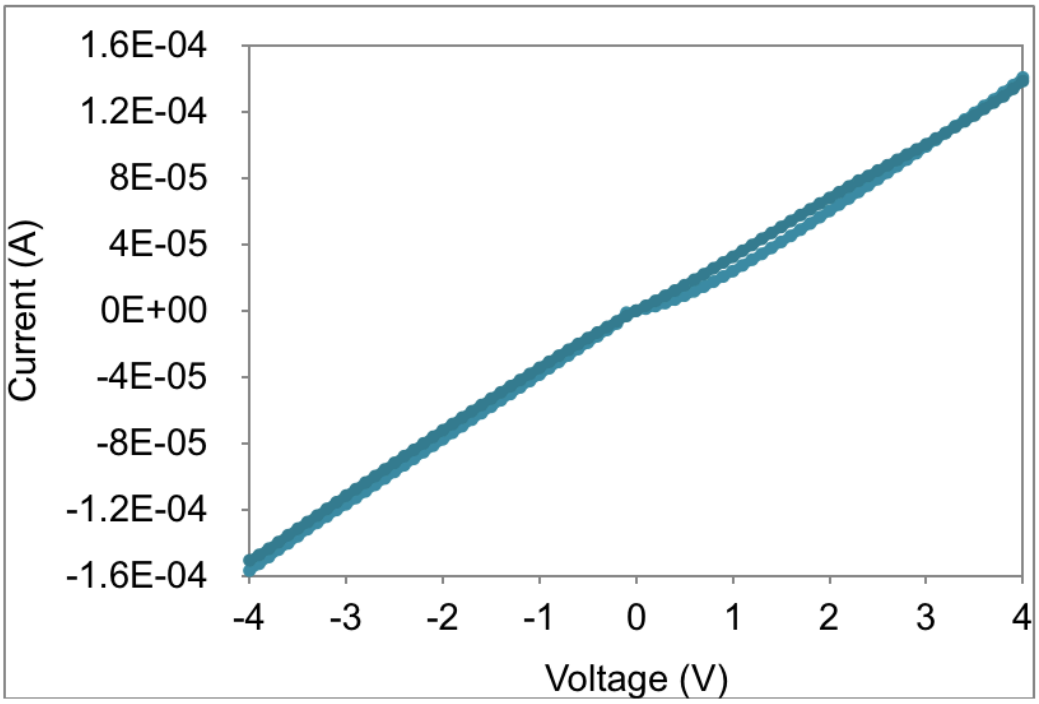

Figure 50. Current-voltage characteristics of non-mesh before testing.

5.3.2 Sensing of Ambient Oxygen under Heat

In Fig. 53, IV plots for the nano meshes and the devices without meshes are shown after 25 minutes in heated ambient air (black) and again after an additional 5 minutes of exposure (red). In Fig. 53(a) and 53(b), the devices without meshes lose their memristance after the 25-minute exposure and become strictly resistive in behavior. Additionally, the overall resistance of the device increases from 25-27 kilo-ohms to 89-107 kilo-ohms. Other devices without meshes displayed similar resistive behavior at this juncture.

After another 5 minutes of exposure to ambient air at 180 deg C, the resistances of these same devices without meshes remain virtually unchanged, as

shown by the overlapping plots in red. This is to be expected considering that the diffusion of oxygen into the sides of the switching layer has a depth limit well under the width of the Cu_xO. EDS analyses of these devices, which are shown in Table 6, show a 1.03%+-0.05% increase in oxygen composition after the total 30 minutes of exposure. (The data in Table 6 are unpaired.) This slight increase in composition is not unreasonable given that the switching layer is not completely enclosed by the top W layer. More importantly, this measurement is used as a type of control for comparison to the mesh devices. (The oxygen content includes that of the SiO2/Si substrate.)

Table 7. EDS Results - Oxygen Composition for Non-Mesh

O % (before)	**O % (after)**	**Error %**
30.22	30.62	<=0.05
27.25	30.1	<=0.05
30.05	28.72	<=0.05
29.62	31.83	<=0.05
AVERAGE = 29.285	**AVERAGE = 30.3175**	

On the other hand, the nano meshes in 52(c) and 52(d) maintain memristance after being subjected to 25 minutes of ambient air, thus making memristive sensing feasible. (The devices also increase in overall resistance from 28-31 kilo ohms to 128-240 kilo-ohms.) After an additional 5 minutes of exposure to ambient air at the operating temperature of 180 deg C, distinguishable shifts in hystereses are observed for these same nano meshes (in red). For the case of the

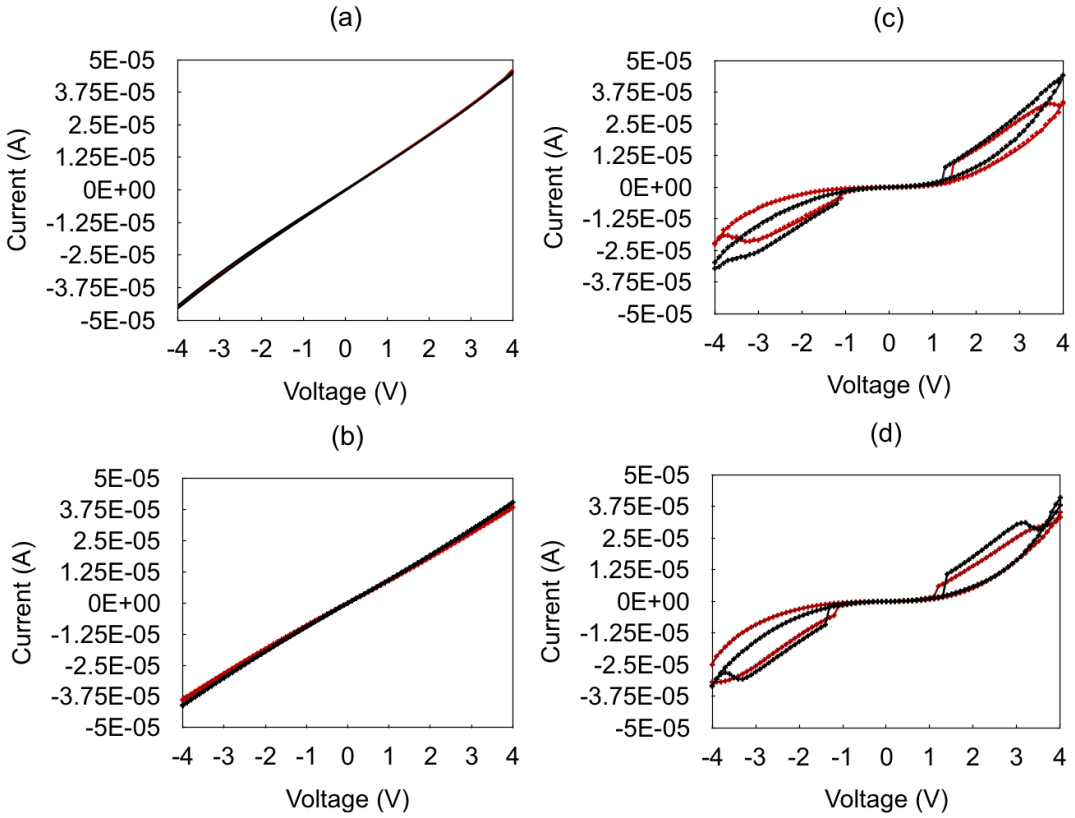

Figure 51. Current-voltage plots for two non mesh devices in (a) and (b) and for two nano mesh devices in (c) and (d). The black data points are after substrate has been subjected to ambient air at 180 deg C for 25 minutes while the red is after an additional five minutes.

device in 52(c), the high resistance state (HRS) and low resistance state (LRS) increase up to 74.8% and 25.0%, respectively. Meanwhile, for the case of the nano mesh in 53(d), the HRS increases by up to 72.4% while the LRS increases by up to 22.8%. EDS analyses further show a 1.45%+-0.05% increase in oxygen composition, which is higher than that of the control group (i.e., the devices without meshes). (The data in Table 7 are unpaired.)

Table 8. EDS Results - Oxygen Composition for Nano-Mesh

O % (before)	O % (after)	Error %
31.69	32	<=0.05
31.46	32.49	<=0.05
31.5	33.29	<=0.05
31.4	34.06	<=0.05
AVERAGE = 31.5125	**AVERAGE = 32.96**	

For further comparison, Fig. 53 and 54 show current-voltage (IV) plots for two micro mesh devices that were subjected to ambient air at the working temperature of 180 deg C. Initially, the micro-mesh device measured in 53(a) displays slight resistive switching (black). After 25 minutes of exposure to ambient air at 180 deg C, this same micro mesh becomes capacitor-like, with a resistance on the order of 1e10 ohms. Fig. 53(b) is a single plot of the micro mesh after exposure for better clarity of this capacitance. In Fig. 54(a), we show a second

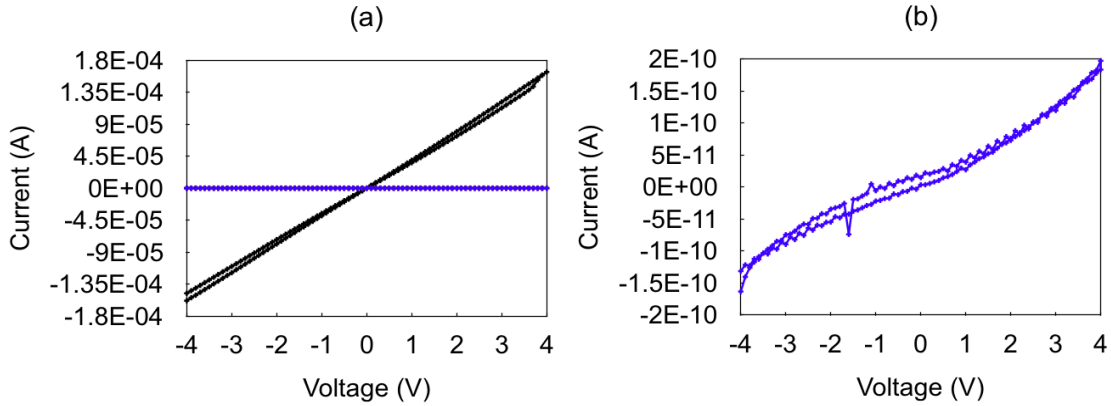

Figure 52. Current-voltage plots for a micro mesh. The black data points are before testing while the blue is after substrate has been subjected to ambient air at 180 deg C for a total of 30 minutes. The plot in (a) is an overlay of both sets of data while (b) is a closeup of the latter set.

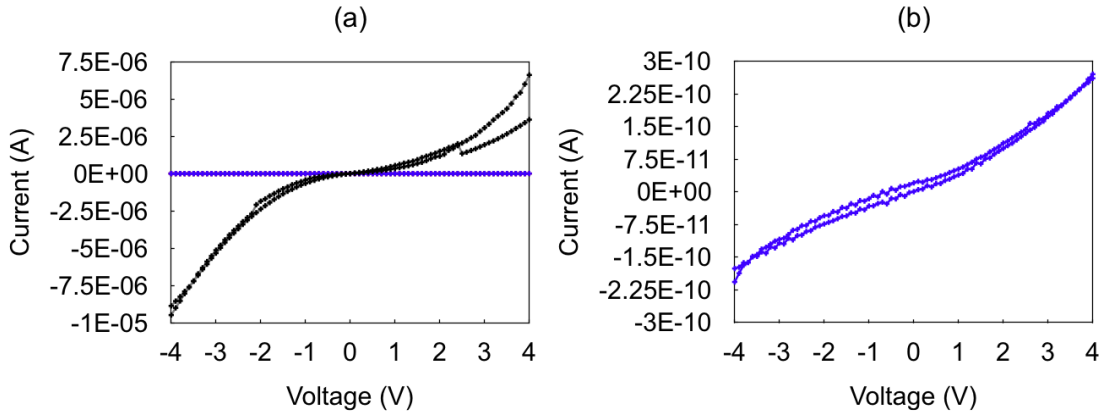

Figure 53. Current-voltage plots for a second micro mesh. The black data points are after substrate has been subjected to ambient air at 180 deg C for 25 minutes while the blue is after an additional five minutes. The plot in (a) is an overlay of both sets of data while (b) is a closeup of the latter set.

micro mesh which maintained slight memristance (black) after 25 minutes in heated hair. However, after an additional five minutes of exposure, this second micro mesh shifts from slight resistive switching (black) to capacitor-like (blue). All other micro meshes tested on the substrate behaved similarly. It is believed that these micro meshes develop a capacitance and high resistance after exposure to ambient air at 180 deg C because the CuxO switching layer becomes oversaturated with oxygen. Atomic composition results from EDS analyses show a 1.96%+-0.05% increase in oxygen composition after exposure, which is higher than those of both the control group and the nano meshes. (The data in Table 8 are unpaired.)

Table 9. EDS Results - Oxygen Composition for Micro-Mesh

O % (before)	O % (after)	Error %
31.75	33.22	<=0.05
31.92	33.29	<=0.05
31.8	33.57	<=0.05
31.52	34.73	<=0.05
AVERAGE = 31.7475	**AVERAGE = 33.7025**	

5.3.3 Sensing Mechanism – Adsorption and Diffusion

Thin film metal oxides can undergo adsorption and diffusion of oxygen [2-6] in the presence of ambient air. As demonstrated in Fig. 55(a), oxygen is first ionically adsorbed (O_2 = O_2-+ h+) onto the surface from the surrounding environment [3], [6]. We can write the change in oxygen concentration C with time across a thin region of thickness dx at a depth x from the Cu_xO surface as the difference between the flux F of oxygen per unit area entering the region and that leaving the region [5]

$$\frac{\partial C}{\partial t} dx = F(x) - F(x + dx). \tag{12}$$

A Taylor-series expansion then allows us to approximate the last term as

$$F(x + dx) \approx F(x) + \left(\frac{\partial F}{\partial x}\right) dx, \tag{13}$$

which allows us to rewrite the change in oxygen concentration as

$$\frac{\partial C(x)}{\partial t} \approx -\frac{\partial F}{\partial x}. \tag{14}$$

Fick's first law states that the flux density is proportional to the concentration gradient, where D is the diffusivity:

$$F \approx -D\frac{\partial C}{\partial x} \tag{15}$$

Combining (14) and (15), we obtain Fick's second law

$$\frac{\partial C}{\partial t} \approx D\frac{\partial^2 C}{\partial x^2}, \tag{16}$$

which states that diffusion causes the concentration in the layer to change with time. In our case, it is the diffusion of ionically adsorbed oxygen that causes the oxygen concentration in the Cu_xO layer to increase with time. These oxygen ions can then encounter and fill nearby vacancy sites [3, 5, 7-8], as illustrated in Fig. 55(b). It is believed that as the concentration of vacancies is reduced, fewer conductive filament branches may be re-healed during the switching process as modeled in Fig. 55(c). Consequently, the conductivity of the switching layer decreases (or the resistance states increase) which agrees with our results.

As for the memristance differences between the nano meshes (300- nm holes) and the micro meshes (700-nm holes), we look to both the number and size of holes for each set of devices. In the case of the nanomeshes, there were 52 holes per mesh making the total area of exposed Cu_xO surface for each memristor

3.68 μm^2. In the case of the micro meshes, there were 16 holes per mesh making the total area of exposed Cu_xO surface 6.52 μm^2. Consequently, the 700-nm meshes expose 1.77 times (nearly twice) more Cu_xO surface to oxygen than the 300-nm meshes. Hence, more oxygen can be adsorbed and diffused into the 700-nm micro mesh devices.

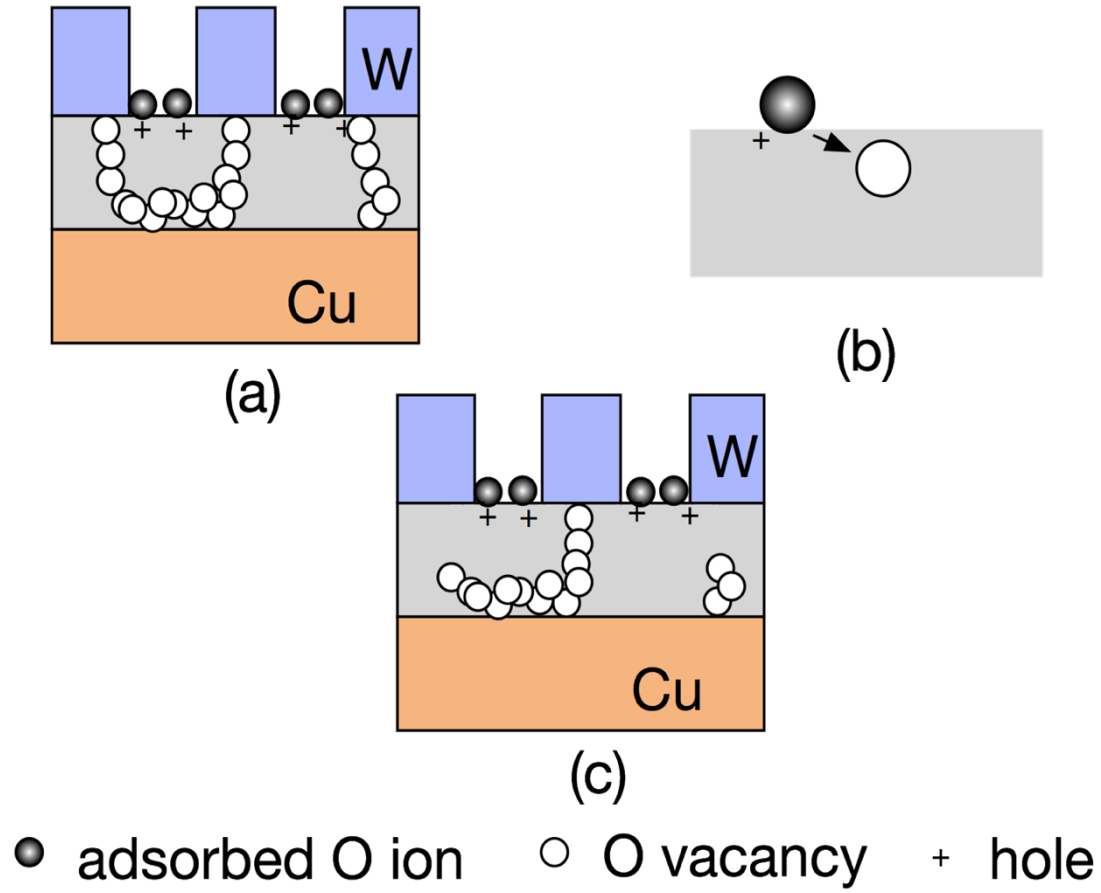

Figure 54. Schematic of adsorption and vacancy filling. (a) Oxygen molecules from the ambient air result in adsorbed oxygen ions and holes near the CuxO surface. (b) Over time, the adsorbed ions fill oxygen vacancies within the layer. (c) The memristor now has higher resistance states due to fewer vacancies.

Other than oxygen content, the detailed arrangement of conductive filaments under the tungsten electrode may have an impact on the resistance difference seen between the micro meshes and nano meshes. Two previous studies demonstrate that conductive filaments are few and localized rather than homogeneous throughout the entire switching layer [9,10] after traditional electroforming. Given the formation of a few local filaments under or near the meshes (rather than strictly outside of the meshes), a conductive filament near a 700-nm hole would experience more exposed Cu_xO surface than one near a 300-nm hole, as shown in Fig. 56.

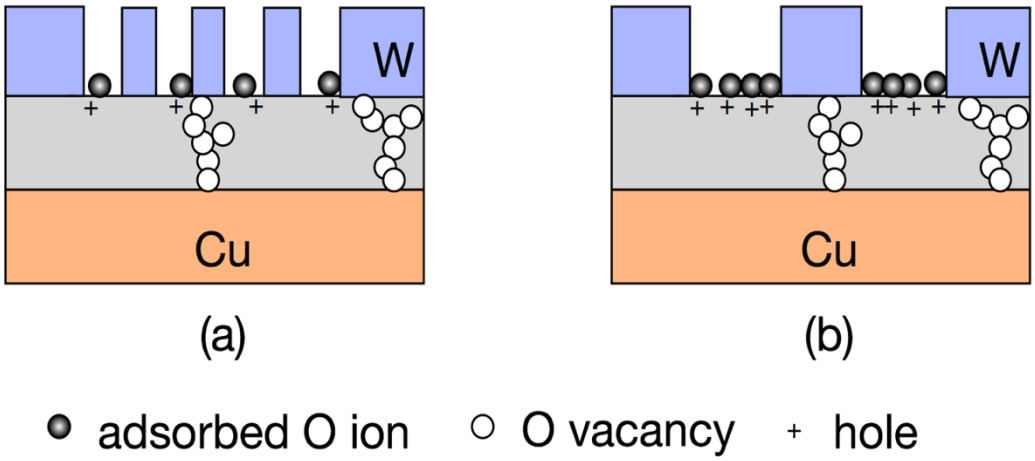

Figure 55. Schematic of (a) nano mesh device and (b) micro mesh device. The micro mesh design experiences more adsorbed oxygen ions.

5.6 SUMMARY

In summary, we have demonstrated the use of memristors for passive sensing by taking advantage of the device's ability to memorize (or record) historical information. There was a notable increase in HRS and LRS when memristors that were designed with 300-nm holes were exposed to ambient oxygen for five minutes at 180 deg C. The mechanism by which this occurred is believed to be the filling of vacancy sites within the switching layer by adsorbed oxygen ions. EDS profiles, which show increases in oxygen composition, are consistent with this adsorption and incorporation of oxygen into the CuxO layer. Additionally, there is evidence to suggest that the size and number of holes is important. In the case of devices with 700-nm holes, the memristance was replaced by capacitance and high resistance after exposure to ambient air at 180 deg C. This observation is believed to be the result of oversaturation of oxygen into the CuxO layer, and EDS profiles support this. There is potential application of passive "memsensors" as sensing alternatives for devices which typically have no batteries integrated due to their small sizes. Such devices may include micro/nanorobots such as catalytically-driven microjets [11] or artificial bacteria flagella [12] designed for medical applications. Additionally, this work increases understanding of environmental effects on memristors, including tunability.

REFERENCES

REFERENCES

1. C. Nyenke and L. Dong, “Fabrication of a W/CuxO/Cu memristor with sub-micron holes for passive sensing of oxygen,” *Microelectronic Engineering*, vol. 164, pp. 48-52, Oct. 2016.

2. A. Goswami, *Thin Film Fundamentals*, first ed. New Delhi: New Age International Pvt Ltd Publishers, 1996.

3. H. Freund, “Metal oxide surfaces: electronic structure and molecular adsorption,” *Basic Solid State Physics (Physica Status Solidi B)*, vol. 192, pp. 407-440, Dec. 1995.

4. P. R. F. Rocha, A. Kiazadeh, D. M. De Leeuw, S. C. J. Meskers, F. Verbakel, D. M. Taylor, and H. L. Gomes, “The role of internal structure in the anomalous switching dynamics,” *Journal of Applied Physics*, vol. 113, art. no. 134504, Apr. 2013.

5. R. S. Muller, T. I. Kamins, and M. Chan, *Device Electronics for Integrated Circuits*. New York: Wiley & Sons, Inc., 2003, pp. 84-86.

6. G. F. Fine, L. M. Cavanagh, A. Afonja, and R. Binions, “Metal oxide semi-conductor gas sensors in environmental monitoring,” *Sensors*, vol.10, pp. 5469-5502, Jun. 2010.

7. J. Tedesco, L. Stephey, M. Hernandez-Mora, C. Richter, and N. Gergel-Hackett, "Switching mechanisms in flexible solution-processed TiO_2 memristors," *Nanotechnology*, vol. 23, art. no. 305206, Aug. 2012.

8. D.H. Kwon, K.M. Kim, J.H. Jang, J.M. Jeon, M.H. Lee, G.H. Kim, X.S. Li, G.S. Park, B. Lee, S. Han, M. Kim, and C.S. Hwang, “Atomic structure of conducting nanofilaments in TiO_2 resistive switching memory,” *Nature Nanotechnology*, vol. 5, no. 2, pp. 148-153, Feb. 2010.

9. R. Dittmann, R. Muenstermann, I.K. D. Park, T. Menke, J. Mayer, A. Besmehn, F. Kronast, C. Schneider, and R. Waser, “Scaling potential of local redox processes in memristive $SrTiO_3$ thin-film devices,” *Proceedings of the IEEE 100*, vol. 6, pp. 1979-1990, 2012.

10. Y. Yang, P. Gao, S. Gaba, T. Chang, X. Pan, and W. Lu, “Observation of conducting filament growth in nanoscale resistive memories,” *Nature Communications*, vol. 3, art. no. 732, Mar. 2012.

11. V. Magdanz, M. Guix, and O. G. Schmidt, “Tubular micromotors: from microjets to spermbots,” *Robotics and Biomimetics*, vol. 1, no. 11, pp. 1-10, Oct. 2014.

12. L. Zhang, J. J. Abbott, L. Dong, B. E. Kratochvil, D. Bell, and B. J. Nelson, “Artificial bacterial flagella: Fabrication and magnetic control,” *Applied Physics Letters*, vol. 94, art. no. 064107, Feb. 2009.

CHAPTER 6 EFFECT OF NITROGEN DIOXIDE AND AMMONIA ON RESISTIVE SWITCHING

6.1 INTRODUCTION

This final work, which references publication [1], set out to investigate the influence of oxidizing and reducing gases on the resistive switching behavior of a Cu_xO-based memristor. This capability has the potential to extend memristor research to reversible gas sensing in the near future. While traditional resistive gas sensors only respond with a change in resistance, the memristor can act as an "enhanced" sensor in that it may respond with changes in resistance states, and in turn hysteresis gap. For this study, the memristive characteristics before, during, and after exposure to nitrogen dioxide (NO_2) — an oxidizing gas — and ammonia (NH_3) — a reducing gas — is examined.

6.2 EXPERIMENTAL SETUP

Current and voltage measurements were collected with a Keithley 6487 Picoammeter and a probe setup in which the bottom Cu electrode was grounded and a bias voltage applied to the top W electrode. The first substrate was directly subjected to 10 then 20 ppm of NO_2 through a 2-mm diameter tube connected to a gas source in order to determine NO_2 detection. A similar setup was used for the second substrate in detecting 100 ppm of NH_3. Both tests were performed at room

temperature, and electrical measurements were collected before, during, and after gas exposure. These measurements were then compared and analyzed. Additionally, sensitivity of the device to stimuli was quantified by dividing the resistances after exposure by the resistances before exposure.

6.3 DISCUSSION OF RESULTS

6.3.1 Evaluation of NO2 Detection

Figs. 57 and 58 shows current-voltage plots for the first device – Fig. 57 is prior to NO_2 exposure, Fig. 62(a)-(d) is after exposure has ceased, and Fig. 58(e)-(f) upon full recovery. Prior to gas exposure, the memristor demonstrates a consistent pinched hysteresis in two consecutive overlapping voltage sweeps shown in Fig. 57. After 10 minutes of exposure to 20 ppm, there is then a notable decrease in resistance state values. Additionally, the hysteresis collapses, or becomes thinner. After the NO_2 source has been shut off, the resistance states remain this way for an additional 5 minutes, as shown in Fig. 58(a). Then 10 minutes after shutoff, the device begins to gradually recover as observed in the slight widening of the hysteresis depicted in Fig. 58(b). In Fig. 58(c) and (d), we observe further widening of the hystereses coupled with increases in resistance states while electrical measurements continue to be taken at 15 minutes, and 20 minutes, respectively, after gas exposure has ceased. It is at 25 minutes after shutoff — shown in Fig. 62(e) — that the original current-voltage characteristics

appear. The complete recovery is confirmed at 30 minutes after shutoff, which is depicted in Fig. 58(f).

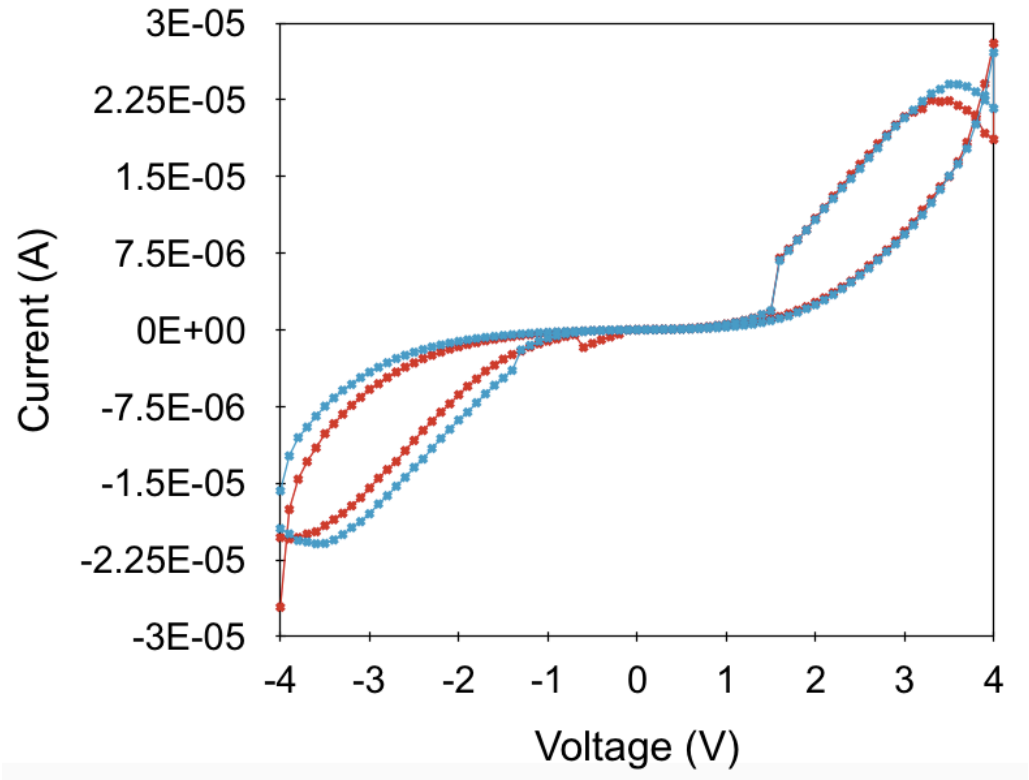

Figure 56. IV characteristics before NO_2 exposure.

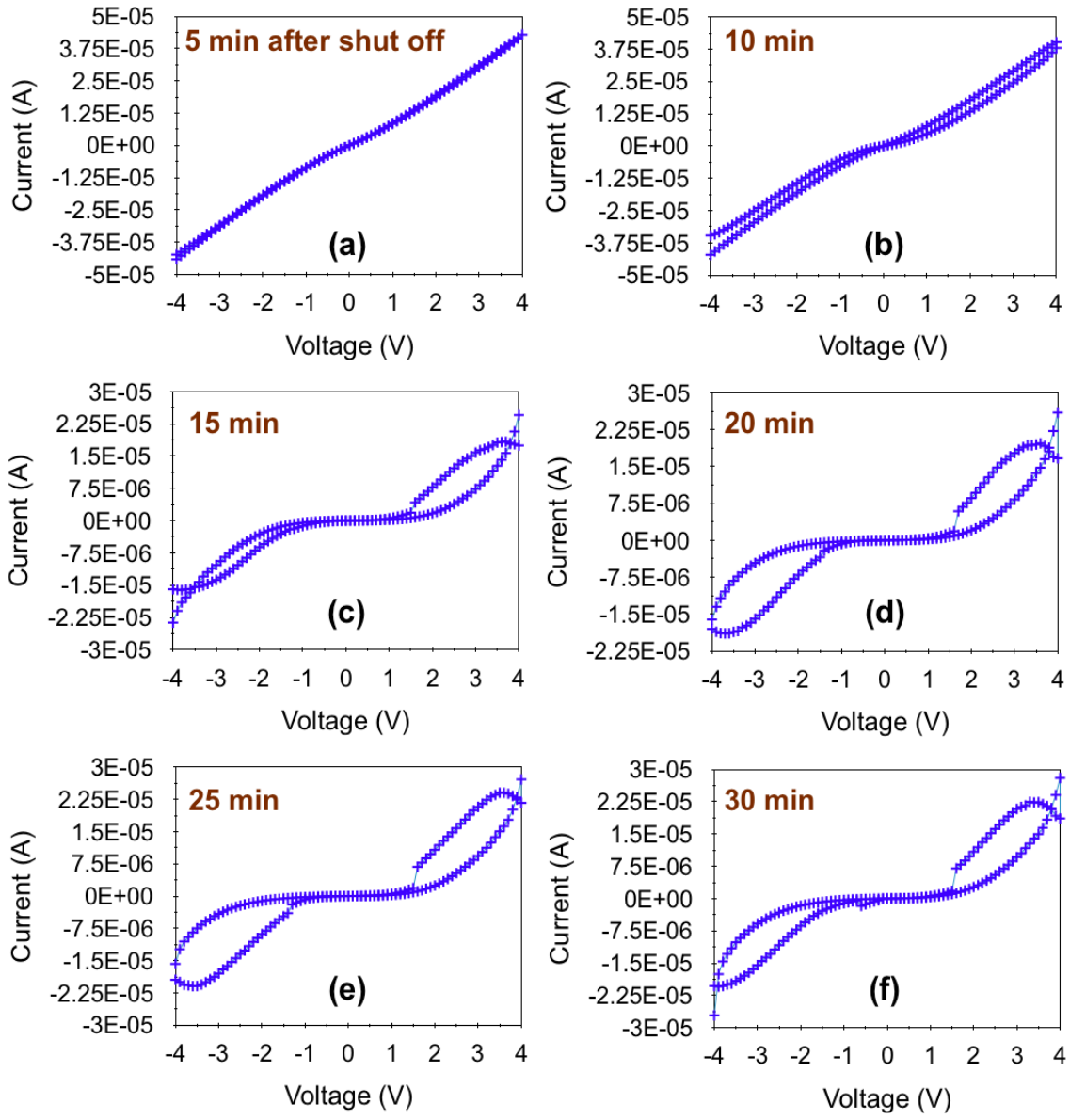

Figure 57. Current-voltage plots for device #1 after 20 ppm NO_2 exposure. Plots (a-f) demonstrate gradual recovery of the device at five-minute intervals. The final plot in (f) is 30 minutes after exposure.

The gas response of the device, which was calculated by the resistance gap in ambient air divided by the resistance gap in 20 ppm NO_2, is 44.5 at 3.5 V and 154.0 at -3.5 V. (These resistance gap values are shown in Tables 10 and 11.)

Table 10. Nitrogen dioxide detection of device #1 (negative bias)

NO2 (negative bias)	Low resistance state (at -3.5V)	High resistance state (at -3.5V)	Resistance gap (HRS minus LRS)
before	1.43E+05 Ω	4.96E+05 Ω	3.53E+05 Ω
after	9.30E+04 Ω	9.53E+04 Ω	2.30E+03 Ω

Table 11. Nitrogen dioxide detection of device #1 (positive bias)

NO2 (positive bias)	Low resistance state (at 3.5V)	High resistance state (at 3.5V)	Resistance gap
before	1.76E+05 Ω	2.57E+05 Ω	8.02E+04 Ω
after	9.47E+04 Ω	9.65E+04 Ω	1.80E+03 Ω

6.3.2 Evaluation of NH3 Detection

In Fig. 59, current-voltage plots depict an opposite trend when the second device is exposed to 100 ppm of NH_3 at room temperature. Initially there is a slight hysteresis prior to detection, as shown in Fig. 63(a), but after 20 minutes of exposure to NH_3 the memristor begins to respond by a widening of the hysteresis gap. Fig. 59(b) shows the device's response after 50 minutes of gas exposure, where the hysteresis widens to its maximum. The resistance states also decrease, as shown in Fig. 59(b) as well as in Tables III and IV. When exposure to NH_3

ceases, electrical measurements continue to be recorded for an additional 30 minutes, at which the memristor demonstrates recovery as shown in Fig. 59(c). The gas response of the device, which was calculated by the resistance gap in 100 ppm NH_3 divided by the resistance gap in ambient air, is 43.2 (for the negative voltage region). These values are also shown in Tables 12 and 13.

Table 12. Ammonia detection of device #2 (negative bias)

NH3 (negative bias)	Low resistance state (at -2.5V)	High resistance state (at -2.5V)	Resistance gap
before	2.43E+09 Ω	2.46E+09 Ω	3.56E+07 Ω
after	5.15E+08 Ω	2.05E+09 Ω	1.54E+09 Ω

Table 13. Ammonia detection of device #2 (positive bias)

NH3 (positive bias)	Low resistance state (at 2.5V)	High resistance state (at 2.5V)	Resistance gap
before	2.43E+09 Ω	2.46E+09 Ω	3.56E+07 Ω
after	4.07E+08 Ω	3.02E+12 Ω	3.02E+12 Ω

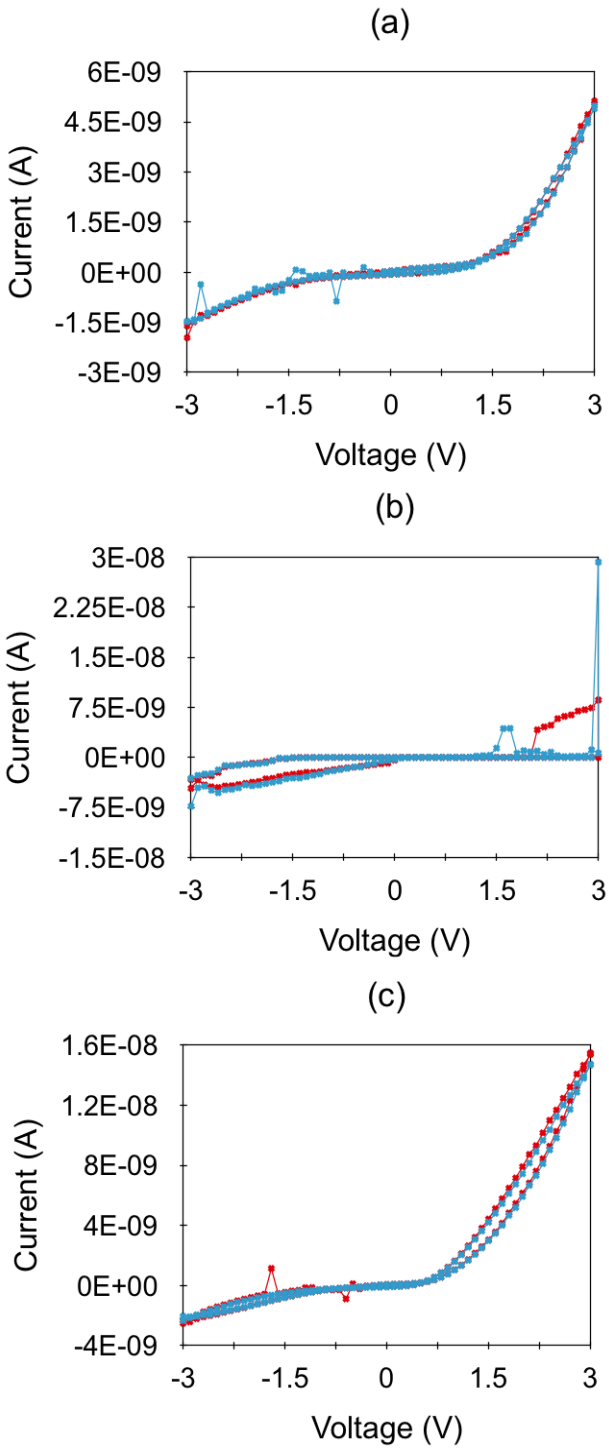

Figure 58. Current-voltage plots for device #1. The three plots are an overlay of two voltages sweeps (a) prior to exposure to 100ppm NH_3, (b) after 50 and 55 minutes of exposure, and (c) after 30 and 35 minutes of recovery.

6.4.3 Mechanism of Gas Detection

The mechanism by which NO_2 detection occurs is related to the surface effects of the metal oxide switching layer [2-3] and illustrated in Fig. 60. After device fabrication, oxygen molecules from the ambient air adsorb to the Cu_xO surface and extract electrons from the conduction band forming ionically adsorbed oxygen (O_2(ads)- = O_2(ads) + e-) [3-5]. This results in an accumulation of holes near the surface which is further increased in the presence of NO_2, an oxidizing gas. (NO_2 takes electrons from the adsorbed oxygen ions and Cu_xO surface.) These chemical reactions are as follows [3-5]:

$$NO_{2(g)} + O^-_{2(ads)} \rightarrow NO^-_{2(ads)} + O_{2(g)} \quad (17)$$

$$NO_{2(ads)} + e^- \rightarrow NO^-_{2(ads)} \quad (18)$$

This increase in hole accumulation causes the p-type Cu_xO to increase in conductivity (or decrease in resistance), which supports the observation made in Fig. 4. What is not immediately clear is why the hysteresis gap also collapses during this process. Once the NO_2 source is cut off, there is an eventual recovery of the original resistance states and hysteresis shape. This is because the chemical process is reversed, and oxygen is readsorbed from the ambient air to the Cu_xO surface [3-5].

Likewise, the mechanism for NH_3 detection involves adsorbed oxygen ions on the Cu_xO surface. Unlike NO_2, NH_3 is a reducing gas, thus giving up electrons in the chemical process as demonstrated in the following reaction [6,7]:

$$NH_{3(g)} + 3O^-_{2(ads)} \rightarrow 6H_2O + 2N_2 + 6e^- \quad (19)$$

This reaction results in the addition of electrons to the Cu_xO surface, which in turn leads to a decrease in hole accumulation due to recombination. For p-type resistive gas detectors and sensors, this process should translate to an increase in resistance (or decrease in conductivity) [5,8]. However, the overall decrease in resistance states for this memristor indicates that the deposited Cu_xO layer is actually n-type rather than p-type. This suggestion is supported by previous literature that points to the creation of n-type Cu_xO given a relatively high (>50% PO_2) [9] or low introduction of oxygen (e.g., Cu-rich) during deposition [9,10]. The high initial resistance of this memristor (on the order of 10^9 ohms) versus the resistance of the previous memristor (on the order of 10^5 ohms) shows evidence of relatively high oxygen concentration in spite of both devices being the same thicknesses.

In addition to these observations, exposure of the device to NH_3 correlates with a widening of the hysteresis gap as observed in Fig. 59. Further analysis is necessary to determine the physical reasoning behind this phenomenon but

repeated tests confirm the association between NH_3 exposure and increasing distance between resistance states.

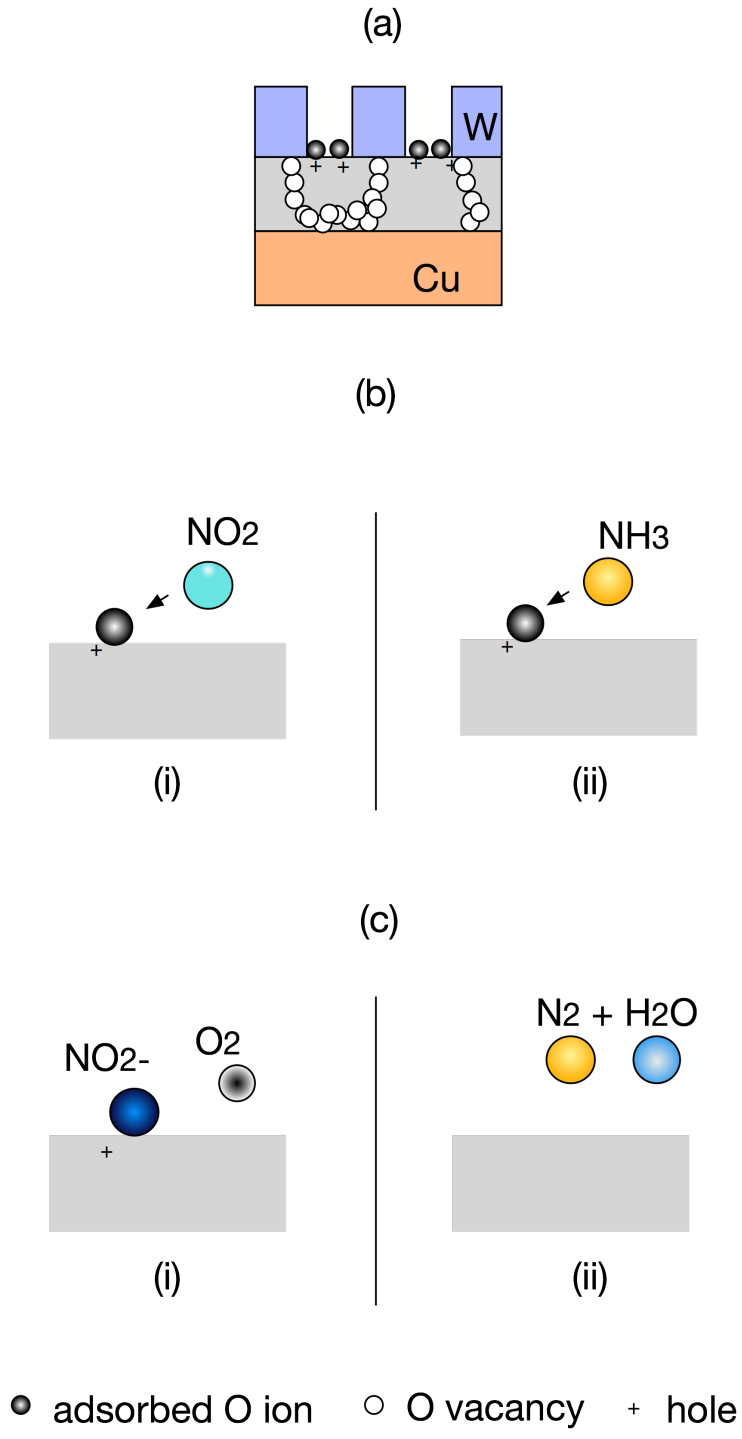

Figure 59. Depiction of gas detection mechanism.

6.6 SUMMARY

In conclusion, we have shown that we can achieve reversible gas detection through the design of perforated memristors. In response to gas exposure, these devices exhibit changes in low and high resistance states, which result in either a collapse or widening of the hysteresis gap as well as a decrease in overall conductivity. These observations suggest an association between the memristor resistance states and exposure to an oxidizing (NO_2) or reducing gas (NH_3), though further analysis is necessary to physically explain the influence on hysteresis gap change. This work introduces the possibility of the memristor as an "enhanced" resistive gas detector (and ultimately sensor) by providing additional information within the shape and size of the hysteresis. This work also presents the potential of tuning memristor characteristics after fabrication via external stimuli, such as gases.

REFERENCES

REFERENCES

1. C. Nyenke and L. Dong, “Effect of NO2 and NH3 on the resistive switching behavior of W/CuxO/Cu memristors,” *Journal of Micromechanics and Microengineering*, vol. 27, no. 10, art. no. 105013, Oct. 2017. 10.1088/1361-6439/aa8672. © IOP Publishing. Reproduced with permission. All rights reserved.

2. N. Barsan, C. Simion, T. Heine, S. Pokhrel, and U. Weimar, “Modeling of sensing and transduction for p-type semiconducting metal oxide based gas sensors”, *Journal of Electroceramics*, vol. 25, pp. 11-19, June 2009.

3. K. Wetchakuna, T. Samerjaia, N. Tamaekonga, C. Liewhirana, C. Siriwonga, et al., “Semiconducting metal oxides as sensors for environmentally hazardous gases,” *Sensors and Actuators B: Chemical*, vol. 160, pp. 580-591, Aug. 2011.

4. G. F. Fine, L. M. Cavanagh, A. Afonja, and R. Binions, “Metal oxide semiconductor gas sensors in environmental monitoring,” *Sensors*, vol. 10, pp. 5469-5502, Jun. 2010.

5. A.A. Mane, M.P. Suryawanshi, J.H. Kim and A.V. Moholkar, “Fast response of sprayed vanadium pentoxide (V_2O_5) nanorods towards nitrogen dioxide (NO_2) gas detection,” *Applied Surface Science*, vol. 403, pp. 540–550, May 2017.

6. A. Sharma, P. Bhojane, A. K. Rana, Y. Kumar, and P. M., Shirage, “Mesoporous nickel cobalt hydroxide/oxide as an excellent room temperature ammonia sensor,” *Scripta Materialia*, vol. 128, pp. 65-68, Feb. 2017.

7. I. Jiménez, M. A. Centeno, R. Scotti, F. Morazzoni, A. Cornet, et al., “NH_3 interaction with catalytically modified nano-WO_3 powders for gas sensing applications,” *Journal of The Electrochemical Society*, vol. 150, pp. 72-80, Feb. 2003.

8. S. Bhuvaneshwari, N. Gopalakrishnan, “Hydrothermally synthesized copper oxide (CuO) superstructures for ammonia sensing,” *Journal of Colloid and Interface Science*, vol. 480, pp. 76-84, Jul. 2016.

9. V. Figueiredo, E. Elangovan, R. Barros, J. V. Pinto, T. Busani, et al., “p-Type Cu_xO films deposited at room temperature for thin-film transistors,” *Journal of Display Technology*, vol. 8, pp. 41-47, Jan. 2012.

10. S. H. Lee, M. Shin, S. J. Yun, and J. W. Lim, “CuO_x/a-Si:H heterojunction thin-film solar cell with an n-type μc-Si:H depletion-assisting layer,” *Progress in Photovoltaics*, vol. 23, pp. 1642-1648, Nov. 2015.

CHAPTER 7 CONCLUSIONS AND FUTURE WORK

7.1 SUMMARY OF CONCLUSIONS

In this dissertation, Cu_xO-based memristors were designed, fabricated, and investigated for passive sensing of oxygen as well as reversible sensing of nitrogen dioxide (an oxidizing gas) and ammonia (a reducing gas) in consecutive studies. The first study set out to determine the feasibility of such memristors for passive sensing under ambient conditions [1]. It was then concluded that resistance states demonstrated increases with time (i.e., days) while EDS profiles were consistent with the adsorption of oxygen to the Cu_xO switching layers. The second study built upon the first study by introducing heat and an improved memristor design – which included 1) sub-micron holes in the tungsten top electrode and 2) more devices per substrate – for further investigation of passive sensing [2]. From this study, it was confirmed that resistance states and atomic composition both increase with exposure to oxygen from the air and depend on the surface area of the exposed switching layer. The mechanism by which this detection occurred was determined to be the diffusion of adsorbed oxygen ions and the filling of local oxygen vacancies over time. The final study set out to demonstrate the reversible detection of an oxidizing gas (nitrogen dioxide) and a reducing gas (ammonia) by the Cu_xO-based memristors [3]. In response to gas exposure, these devices exhibited decreases in low and high resistance states, which resulted in either a collapse (or widening)

of the current-voltage hysteresis gap. The mechanism by which these resistance state changes occurred was determined to be a reversible chemical reaction between the oxidizing (or reducing) gas and the adsorbed oxygen ions on the exposed switching layer surface. Ultimately, this dissertation demonstrated a potential application of the memristor as a multifunctional tool for memory and gas detection.

7.2 FUTURE RESEARCH

7.2.1 Further Understanding of Reversible Sensing Mechanism

For future work, it is suggested that more experiments be done to build upon the reversible sensing of oxidizing and reducing gases with memristors. Further analysis is necessary to physically understand the influence of oxidization and reduction on the change in current-voltage hysteresis gap size. This analysis would require several more test trials than was explored in this dissertation in order to gather more data. These tests could incorporate various ranges (ppm) of gas concentrations and, perhaps, different temperatures as well.

7.2.2 Different Switching Layer Composition and Design

Future work may also investigate other metal oxide materials – for example nonstoichiometric forms of zinc oxide or tungsten oxide – for the switching layers. This is because the choice of material could be made to greatly increase the sensing capability and switching endurance of the device. Alternatively, fabrication of the switching layer via the bilayer approach [4, 5, 6, 7] (as discussed in the literature review) could further improve the device performance. This approach may require a deposition method other than reactive sputtering to better control the composition and structure of the second layer. Additionally, x-ray photoelectron spectroscopy (XPS) or other analytical techniques could be employed to more accurately examine the chemical state of the switching layer as well as determine the empirical formula.

7.2.3 Influence of Memristor Area on Sensing

Lastly, construction of thinner electrodes in a crossbar array structure – and thus, smaller memristors in terms of area – may be investigated for influence on sensitivity to gas or chemical stimuli. Electron beam lithography (EBL) can be used to fabricate nanoelectrodes for the device.

REFERENCES

REFERENCES

1. C. Nyenke and L. Dong, “Sensing ambient oxygen using a W/CuxO/Cu memristor,” *IEEE 10th International Conference on Nano/Micro Engineered and Molecular Systems*, pp. 254-258, Apr. 2015.

2. C. Nyenke and L. Dong, “Fabrication of a W/CuxO/Cu memristor with sub-micron holes for passive sensing of oxygen,” *Microelectronic Engineering*, vol. 164, pp. 48-52, Oct. 2016.

3. C. Nyenke and L. Dong, “Effect of NO2 and NH3 on the resistive switching behavior of W/CuxO/Cu memristors,” *Journal of Micromechanics and Microengineering*, vol. 27, no. 10, art. no. 105013, Oct. 2017. 10.1088/1361-6439/aa8672.

4. C.H. Huang, J. S. Huang, S. M. Lin, W. Y. Chang, J. H. He, and Y. L. Chueh, “ZnO_{1-x} nanorod arrays/ZnO thin film bilayer structure: from homojunction diode and high-performance memristor to complementary 1D1R application,” *ACS Nano*, vol. 6, no. 9, pp. 8407-8414, Aug. 2012.

5. S.-M. Lin, J.-S. Huang, W.-C. Chang, T.-C. Hou,. H.-W. Huang, C.-H. Huang, S.- J. Lin and Y.-L. Chueh, “Single-step formation of ZnO/$ZnWO_x$ bilayer structure via interfacial engineering for high performance and low energy consumption resistive memory with controllable high resistance states,” *ACS Applied Materials & Interfaces*, vol. 5, no. 16, pp. 7831-7837, Aug. 2013.

6. M.J. Lee, C. B. Lee, D. Lee, S. R. Lee, M. Chang, J. H. Hur, Y. B. Kim, C. J. Kim, D. H. Seo, S. Seo, U. I. Chung, I. K. Yoo, and K. Kim, “A fast, high-endurance and scalable non-volatile memory device made from asymmetric TaO_2O_{5-x} /TaO_{2-x} bilayer structures,” *Nature Materials*, vol. 10, no. 8, pp. 625-630, Jul. 2011.

7. A. Prakash, S. Maikap, C. S. Lai, T. C. Tien, W. S. Chen, H. Y. Lee, F. T. Chen, M.-J. Kao, and M.-J. Tsai, “Bipolar resistive switching memory using bilayer TaO_x/WO_x films,” *Solid-State Electronics*, vol. 77, pp. 35-40, Nov. 2012.